UNIVERSITÀ DEGLI STUDI DI PADOVA

Sede Amministrativa: Università degli Studi di Padova.

Dipartimento di Astronomia.

SCUOLA DI DOTTORATO DI RICERCA IN SCIENZE TECNOLOGIE E MISURE SPAZIALI (STMS)

Indirizzo: Astronautica e Scienze da Satellite (ASS)
CICLO XX.

DETERMINATION OF THE ORBIT OF TITAN FROM CASSINI ALTIMETER DATA

Determinazione orbitale di Titano tramite i dati altimetrici di Cassini

Direttore: Ch.mo Prof. Cesare Barbieri
Coordinatore: Ch.mo Prof. Giampiero Naletto
Supervisore: Ch.mo Prof. Stefano Casotto

Dottoranda : Sara Poltronieri

Alla mia piccola Alessandra
A mio marito Luca
Ai miei genitori

DETERMINATION OF THE ORBIT OF TITAN FROM CASSINI ALTIMETER DATA

Sara Poltronieri

31 Dicembre 2008

Contents

List of Figures

List of Tables

Sintesi

La ricerca presentata in questa tesi riguarda il miglioramento della determinazione orbitale di Titano tramite l'uso delle osservazioni altimetriche effettuate dallo strumento RADAR a bordo del satellite Cassini. Lo scopo del lavoro si concretizza nello sviluppo e implementazione, nel sistema software di navigazione e determinazione orbitale SOSYA (SOlar SYstem Astrometry, [2]), di un modulo che permette di migliorare un arco orbitale preliminare di Titano con l'introduzione delle misure altimetriche ottenute dallo strumento durante l'incontro ravvicinato con la luna di Saturno. Lo strumento software implementato prende il nome di SOSYA_ART (SOlar SYstem Astrometry_Altimetric Run Tool). In aggiunta, nel contesto della Simulazione delle Misure di SOSYA, è stato sviluppato un modulo che permette la creazione di dati altimetrici sintetici ricorrendo alle geometrie, ai kernels di effemeridi planetarie e alle funzioni disponibili in SPICE.

L'uso dei dati altimetrici, in concomitanza con le altre tipologie di dati disponibili, permette di poter determinare l'orbita di Titano con accuratezze molto più elevate di quelle attualmente raggiungibili attraverso le sole misure radio, aumentando il ritorno scientifico della missione. Infatti, mentre l'orbita di Cassini può essere determinata con sufficiente accuratezza sulla base dei dati di tracking doppler e range da Terra, quella di Titano non può essere determinata con altrettanta sufficiente accuratezza se non sulla base dell'analisi delle perturbazioni che la sonda subisce durante i flyby dedicati all'esperimento gravitazionale. Per questo motivo il lavoro presentato ha come obiettivo principale di stabilire il beneficio dell'introduzione dei dati di tipo altimetrico nel processo di miglioramento della determinazione dell'orbita di Titano. Il problema della determinazione orbitale viene quindi risolto mantenendo "fissa" la traiettoria di Cassini e stimando la posizione di Titano nel sistema saturnocentrico.

Il lavoro svolto può essere diviso in 4 parti:

- Nella prima parte, dopo una breve introduzione alla missione Cassini-Huygens, viene presentato lo strumento RADAR a bordo del satellite con le sue caratteristiche tecniche e i suoi obiettivi scientifici primari. L'attenzione è stata rivolta all'approfondimento del funzionamento dello strumento e alla teoria dell'elaborazione del segnale radar. Parallelamente lo studio ha incluso l'analisi delle tipologie di flyby dell'orbiter e della sequenza operativa della strumentazione di bordo.
- Nella seconda parte del lavoro introduciamo i concetti fondamentali della determinazione orbitale e sviluppiamo il modello di osservazione altimetrico necessario a raggiungere lo scopo del lavoro. L'implementazione di questo modello ci ha consentito di ottenere dei buoni risultati circa la stima dello stato di Titano alle epoche prefissate.
- Nella terza parte descriviamo i flyby durante i quali sono stati raccolti i dati altimetrici che abbiamo ricevuto da CO.RI.S.T.A. (Consortium for Research on Advanced Remote Sensing Systems) e la distribuzione delle osservazioni nel corso dell'intero flyby.
- Infine, nella quarta parte vengono discussi i risultati ottenuti dal processo di determinazione orbitale con la presentazione dei valori delle stime degli stati di Titano ricavate e delle statistiche di tali risultati. Inoltre vengono presentati i grafici dei residui di osservazione in relazione ad ogni flyby utilizzato.

Altimetria da satellite

La missione Cassini-Huygens è il risultato di una collaborazione internazionale fra tre agenzie spaziali principalmente. La costruzione dell'orbiter Cassini è stata gestita e portata a termine dal Jet Propulsion Laboratory della NASA, mentre la sonda Huygens è stata fornita dall'Agenzia Spaziale Europea (ESA). Il contributo dell'Agenzia Spaziale Italiana (ASI) si è concretizzato nella costruzione dell'antenna ad alto guadagno di Cassini per le comunicazioni. Il complesso Cassini-Huygens è equipaggiato per l'esecuzione di diverse investigazioni scientifiche tramite 18 strumenti e 12 di essi si trovano a bordo di Cassini. Tipicamente, buona parte degli strumenti hanno delle funzioni multiple, in modo tale da investigare attentamente in diverse modalità tutti gli elementi importanti del sistema saturniano.

Lanciata nel 1997, la sonda ha compiuto una traiettoria di tipo VVEJGA (Venus-Venus-Earth-Jupiter Gravity Assist) per poter essere proiettata nel sistema di Saturno ed entrarvi nel luglio del 2004. In quel momento è iniziata una missione della durata nominale di 4 anni che ha incluso più di 70 orbite attorno al gigante gassoso, ai suoi anelli e alle sue lune. Ben 45 flyby sono stati esclusivamente destinati a Titano. Huygens è stata rilasciata da Cassini il 25 Dicembre 2004 ed è entrata nella spessa atmosfera della luna collezionando informazioni di estremo interesse scientifico sulla sua composizione chimica, sui fenomeni atmosferici e spettacolari immagini una volta toccato il misterioso suolo di Titano.

Nel Luglio del 2008 la NASA ha confermato la sua decisione di estendere la missione per altri 2 anni visti i notevoli successi ottenuti e il buono stato delle strumentazioni di bordo.

Cassini comunica con la Terra tramite i sottosistemi delle sue antenne, che consistono in un'antenna ad alto guadagno, e in due antenne a basso guadagno. La funzione principale della sua antenna ad alto guadagno è di supportare le comunicazioni con la Terra, ma viene anche usata per gli esperimenti scientifici dallo strumento RADAR e dal Radio Science Subsystem (RSS) entrambi a bordo di Cassini.

RADAR è uno strumento multifunzione che trasmette un impulso chirp modulato linearmente in frequenza, alla frequenza portante in banda Ku (13.78 GHz). Ogni incontro ravvicinato con Titano prevede una precisa sequenza di osservazioni effettuate da tale potente strumento. A seconda della distanza relativa tra la luna e la sonda, RADAR opera in diverse modalità: per immagini, come altimetro, come radiometro e come scatterometro. Ognuno di questi modi operativi consente la raccolta di tipologie di dati differenti. Durante le operazioni di imaging, altimetria e backscattering, RADAR funziona in modalità attiva, cioè trasmette un impulso e ne riceve l'eco. In particolare, in funzione di altimetro, lo strumento misura il ritardo temporale dell'eco di ritorno alla sonda del segnale elettromagnetico inviato con l'obiettivo di ottenere dati numerici precisi dell'altezza del satellite sulla superficie topografica di Titano. Lavorando ad elevata risoluzione ad un'altezza compresa tra 4000 e 9000 km di altezza, Cassini acquisisce profili altimetrici con una risoluzione orizzontale di 24-27 km e una risoluzione verticale di 90-150 m. Trascurando il ritardo nella ricezione del segnale dovuto alla presenza dell'atmosfera, la misura dell'altezza della sonda rispetto alla superficie osservata è data da

$$h = \frac{ct}{2} \tag{1}$$

con un'accuratezza di:

$$\Delta h = \frac{c\tau}{2} = \frac{c}{2B}, \tag{2}$$

dove t è il ritardo temporale tra il segnale trasmesso e l'eco ricevuto, c è la velocità della luce, τ è la lunghezza del segnale e $B = 1/\tau$ è l'ampiezza di banda dell'impulso. Se due punti target sono separati da una distanza Δr, i due eco ricevuti sono separati di un intervallo di tempo pari a $\Delta t = 2\Delta r/c$. Risulta quindi necessario, affinchè i due segnali di ritorno non si sovrappongono nella ricezione, che la durata dell'impulso τ sia $\tau < 2\Delta r/c$. Allora la minima separazione spaziale di due punti target è data proprio dall'Equazione (2) ed è detta risoluzione in range. Per poter ottenere elevate risoluzioni in range è necessario ricorrere a brevi impulsi o ad ampie larghezze di banda del segnale elettromagnetico inviato. Tuttavia l'energia dell'impulso è proporzionale alla sua durata τ, quindi maggiore energia si ottiene con minore larghezza di banda B. Ma questo porta alla diminuzione della risoluzione secondo quanto detto prima. Per conciliare l'esigenza di elevate risoluzioni in distanza si ricorre alla cosiddetta codifica dell'impulso che si realizza modulando il segnale linearmente in frequenza (segnali di tipo chirp) oppure modulando il segnale in fase in modo binario. La prima delle due tecniche citate è utilizzata da RADAR e consiste nell'introdurre una qualche forma di modulazione in un impulso di lunga durata, allargandone la banda. In questo modo è possibile distinguere due echi parzialmente sovrapposti grazie alla modulazione presente nell'impulso.

Determinazione orbitale

Il problema della determinazione orbitale consiste nel determinare la miglior stima dello stato dinamico (cioè posizione e velocità del corpo celeste, e tutti i parametri dinamici relativi ad esso e non) le cui condizioni sono note con precisione finita, utilizzando osservazioni di un certo tipo e un modello dinamico che descriva il sistema con una accuratezza limitata.

L'accuratezza delle effemeridi o dell'orbita ottenute dal processo dipende strettamente dalla precisione e dall'accuratezza dei modelli e dagli errori di misura utilizzati. In generale le osservazioni non sono funzioni lineari del vettore di stato e dei parametri del corpo da stimare. A questo si aggiunge il fatto che nemmeno le equazioni differenziali che descrivono il moto sono lineari. Il meccanismo solitamente adottato è la linearizzazione del problema espandendo le equazioni del moto e le relazioni stato-osservazione attorno alla traiettoria di riferimento. Si calcolano le deviazioni da tale traiettoria in modo da trovare il miglior accordo con le osservazioni tramite il metodo dei minimi quadrati.

La stima a varianza minima con informazione a priori è data dalla seguente

$$\hat{\mathbf{x}}_k = (\widetilde{\mathbf{H}}_k^T \mathbf{R}_k^{-1} \widetilde{\mathbf{H}}_k + \overline{\mathbf{P}}_k^{-1})^{-1} (\widetilde{\mathbf{H}}_k^T \mathbf{R}_k^{-1} \mathbf{y}_k + \overline{\mathbf{P}}_k^{-1} \overline{\mathbf{x}}_k)\,, \tag{3}$$

e la matrice di covarianza associata è:

$$\mathbf{P}_k = (\widetilde{\mathbf{H}}_k^T \mathbf{R}_k^{-1} \widetilde{\mathbf{H}}_k + \overline{\mathbf{P}}_k^{-1})^{-1}. \tag{4}$$

Due tipi di algoritmi implementano tali equazioni: l'algoritmo detto *batch filter* che accumula l'intero set di dati prima di risolvere per $\hat{\mathbf{x}}_k$, e l'algoritmo detto invece *sequential filter* che combina l'osservazione mappata al tempo t_k con la nuova ossevazione al tempo t_k per calcolare la stima $\hat{\mathbf{x}}_k$.

In questo lavoro, ci siamo focalizzati sul problema di determinare una miglior stima dello stato di Titano attraverso l'uso di osservazioni quali i dati altimetrici acquisiti da RADAR durante gli incontri ravvicinati con Titano. L'epoca alla quale viene stimato lo stato del satellite naturale, con algoritmo di tipo batch, antecede di pochi minuti il set di dati raccolti durante il flyby, e questa procedura si ripete per ogni flyby di cui ci sono stati forniti i dati altimetrici. Le stime ottenute sono molto soddisfacenti confrontandole ad esempio con i risultati ottenuti da Jacobson [8] come verrà discusso oltre.

Una volta ottenute le stime dello stato di Titano per ognuno di questi flyby, abbiamo a disposizione un nuovo set di effemeridi del satellite che possono essere utilizzate per ricostruire un'orbita più accurata della luna saturniana.

Osservazioni altimetriche e modello geometrico di osservazione

La tipologia di dato altimetrico fondamentale per questa ricerca, ovvero il range-to-target (RTT), è contenuto nel set di dati di tipo ABDR (Altimeter Burst Data Record) fornite dal PDS, ma tuttora non risultano disponibili tali tabelle per tutti i flyby destinati all'altimetria. Per questo si è deciso di contattare direttamente CO.RI.S.T.A affinchè ci fornisse le misure necessarie per lo sviluppo del software di determinazione orbitale.

Il dato altimetrico che abbiamo ricevuto e di cui ci serviamo per stimare lo stato di Titano all'epoca, è sostanzialmente la distanza tra il satellite e la superficie di Titano calcolato direttamente sulla base del ritardo temporale dell'eco radar ricevuto. Le altezze altimetriche ricevute sono il frutto dell'elaborazione del segnale radar relativo ai flyby Ta, T3, T8, T13, T16, T19, T21, T23, T25, T28, T29, T30, T36 e T39. La Tabella 1 mostra la distribuzione dei dati altimetrici a nostra disposizione e i flyby in cui sono stati raccolti. Come si può notare, i flyby T13 e T25 hanno il minor numero di osservazioni e questo comporta una stima dello stato all'epoca di batch meno accurata delle altre ottenute invece con un numero maggiore di dati altimetrici.

Altimetric observations summary	
Titan Flyby	**N° altimetric data**
Titan flyby Ta	459
Titan flyby T3	291
Titan flyby T8	742
Titan flyby T13	268
Titan flyby T16	886
Titan flyby T19	911
Titan flyby T21	444
Titan flyby T23	887
Titan flyby T25	57
Titan flyby T28	1248
Titan flyby T29	982
Titan flyby T30*	3439
Titan flyby T36*	1833
Titan flyby T39*	633
Total	**13080**

Table 1: Numero di osservazioni altimetriche per ogni flyby. Le tabelle dati SBDR dei flyby contrassegnati da * non sono attualmente presenti sul sito del Planetary Data System.

Per poter ottenere il residuo di osservazione è necessario calcolare geometricamente l'osservazione altimetrica. Il modello geometrico sviluppato e implementato nel software è illustrato in Figura 1. Nel sistema di riferimento baricentrico, l'equazione di osservazione espressa in funzione dello stato di Titano, $\mathbf{X}_\mathrm{T}$, risulta essere la distanza istantanea geometrica (range), esprimibile come

$$\mathbf{G}(\mathbf{X}_\mathrm{T}, t) = h(t) = [(\mathbf{r}_s(t) - \mathbf{r}_\mathrm{C}(t)) \cdot (\mathbf{r}_s(t) - \mathbf{r}_\mathrm{C}(t))]^{\frac{1}{2}} \,, \tag{5}$$

dove $\mathbf{r}_s(t)$ rappresenta le coordinate del punto di intersezione del fascio radar sulla superficie di Titano e $\mathbf{r}_\mathrm{C}(t)$ è il vettore posizione di Cassini.

L'equazione di osservazione, $\mathbf{G}(\mathbf{X}_\mathrm{T}, t)$, è stata implementata nel codice in modo tale da poter scegliere tra l'utilizzo di un modello di osservazione avente una geometria di tipo *nadir-pointing* oppure di un modello con geometria di tipo *off-nadir pointing* in base alla tipologia dei dati in input a disposizione. L'implementazione dell'osservazione off-nadir utilizza i file di assetto di Cassini forniti dal Data Search Service (DSS) del PDS insieme ai kernel file contenenti gli archi orbitali per ogni flyby. L'assetto di Cassini serve per trovare le intersezioni del fascio RADAR 3 (usato per le misure altimetriche) con la superficie di Titano. Infatti lo strumento RADAR è solidale al satellite e quindi la direzione del campo di vista risulta strettamente legata all'assetto dello stesso satellite. Inoltre, come descritto nei kernel file di SPICE contenenti l'allineamento e la direzione di puntamento degli strumenti di bordo, il campo di vista (*FOV*, Field Of View) del fascio 3 è direzionato negativamente lungo l'asse z del sistema di riferimento solidale al satellite. Dopo aver determinato il punto di intersezione nel sistema di riferimento baricentrico, si calcola l'altezza altimetrica come lunghezza del vettore che si ottiene dalla differenza tra la posizione di Cassini e il vettore posizione del punto di intersezione del fascio a terra (Equazione 5).

Implementazione del codice e risultati

Con il modulo di *Simulazione Orbitale* di SOSYA ([2]), sono state integrate numericamente le equazioni del moto per ottenere un nuovo set di condizioni iniziali di Titano e delle altre lune ad una data di poco

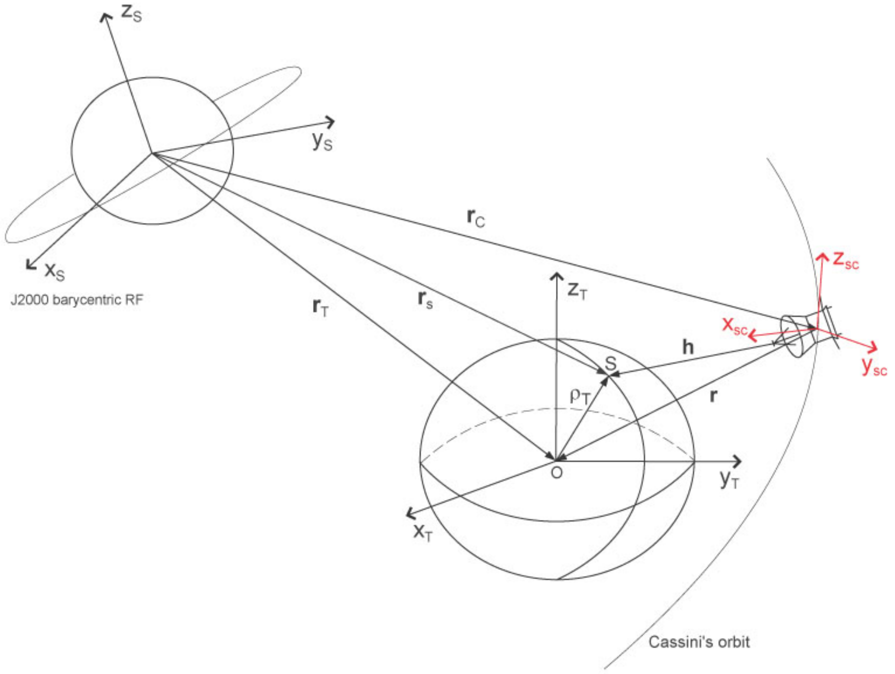

Figure 1: Geometria del modello di osservazione e sistemi di riferimento utilizzati per la soluzione al problema della determinazione orbitale.

antecedente la prima osservazione del flyby. A tale epoca viene poi stimato lo stato di Titano tramite le misure altimetriche collezionate nel medesimo flyby. Per la parte riguardante l'integrazione numerica delle orbite e dell'interpolazione degli stati agli istanti di osservazione, sono state usate le effemeridi planetarie DE405 e il file di effemeridi satellitari ricevute dal Gruppo di Radio Scienza di Cassini dell'Università "La Sapienza" di Roma e specifiche per il tour della sonda. Non avendo a disposizione la loro matrice di varianza associata, la stima dello stato di Titano è stata calcolata inizialmente senza l'introduzione della matrice di varianza a priori. Avendo comunque ottenuto dei buoni risultati con questa impostazione iniziale di simulazione, il processo di determinazione orbitale è stato successivamente effettuato utilizzando la matrice di varianza a priori. Il suo valore è stato impostato a 9 e 25 km per l'indeterminazione sulla posizione e a $9 \cdot 10^{-6}$ e $25 \cdot 10^{-6}$ km/s per la velocità rispettivamente. Come atteso, vincolando il sistema, si ottengono delle stime dello stato più precise con valori di deviazione standard migliori rispetto al caso iniziale.

Dal momento in cui non sono disponibili gli errori di misura associati ad ogni dato altimetrico, si è posto un valore costante di 80 m come accuratezza delle osservazioni. Dopo aver effettuato una serie di simulazioni variando il valore di tale accuratezza di misura, si è notato che la stima varia proporzionalmente all'errore di misura selezionato. Inoltre, come descritto da CO.RI.S.T.A. ([3]), i valori dell'altezza del satellite sulla superficie di Titano sono stati determinati con una precisione migliore di 100 m. Questo giustifica la nostra scelta di porre un valore pari ad 80 m come accuratezza dei dati altimetrici che abbiamo in input.

Le informazioni statistiche sui residui ottenuti dai processi di determinazione senza la varianza a priori sono mostrati in Tabella 2, dove viene dato anche il valore dell'rms, della media e della deviazione standard nel prefit e nel postfit per ogni flyby.

Come si può notare i valori di rms migliorano notevolmente dalla prima all'ultima iterazione: la media totale delle iterazioni di pre-fit di 4.703 km mentre quella delle iterazioni di post-fit di 81.67 m. Il miglioramento dei valori di rms dalla prima all'ultima iterazione è indice di una buona stima dello stato

first iteration	***h*** (km)		
	mean	***σ***	**rms**
Ta	15.977771	1.743615	16.072422
T3	-1.911673	0.129171	1.916017
T8	-2.328764	1.640540	2.847308
T13	-2.806186	0.129327	2.809154
T16	0.576560	1.333688	1.452287
T19	0.517462	2.792778	2.838807
T21	-4.447653	0.554961	4.482065
T23	3.290940	5.007163	5.989466
T25	3.503621	0.192917	3.508835
T28	-3.785247	0.432284	3.809831
T29	-3.590752	1.329476	3.828734
T30	-7.505698	2.914905	8.051689
T36	-0.380654	1.647358	1.690328
T39	-1.871269	3.259723	3.756415

last iteration	***h*** (km)		
	mean	***σ***	**rms**
Ta	-0.000031	0.065519	0.065435
T3	0.000007	0.047574	0.047489
T8	-0.000058	0.043685	0.043622
T13	-0.353466	0.306451	0.467440
T16	-0.000815	0.087654	0.087607
T19	-0.000326	0.101835	0.101777
T21	-0.000005	0.070569	0.070488
T23	-0.000460	0.091950	0.091899
T25	0.000000	0.027994	0.027738
T28	-0.000504	0.080050	0.080019
T29	-0.000598	0.114147	0.114089
T30	0.000138	0.068910	0.068898
T36	-0.001254	0.100706	0.100685
T39	-0.001249	0.108113	0.108031

Table 2: Residui delle osservazioni altimetriche, media e standard deviation alla prima iterazione (a sinistra) e all'ultima iterazione (a destra) per ogni flyby processato senza la matrice di varianza a priori.

di Titano sull'arco orbitale considerato. La media globale dei residui alla prima iterazione è pari a -340 m e decresce al valore della media globale dei residui all'ultima iterazione pari a $-4.296 \cdot 10^{-4}$ km, valore che ci ha permesso di trascurare la stima del bias di osservazione.

La Tabella 3 contiene i vettori di stato di Titano ad ogni epoca insieme ai valori di deviazione standard. Vi sono inoltre riportate le epoche alle quali è stato effettuato il processo di stima dello stato del satellite naturale. I valori di deviazione standard sono maggiori per i flyby T13 e T25. Infatti il numero di osservazioni collezionate durante tali incontri non sono sufficienti per poter ottenere una buona statistica nei residui di osservazione (Tabella 1). Per questo motivo, sebbene vengano comunque inglobati nel processo di determinazione orbitale, vengono esclusi dalla discussione dei risultati ottenuti. Le Figure 2, 3 e 4 mostrano graficamente i valori di deviazione standard degli stati stimati di Titano al variare della matrice di varianza a priori utilizzata. Sebbene in questo lavoro la stima venga fatta solo per Titano, dai valori di deviazione standard presentati nei grafici si evince che i risultati ottenuti sono buoni ripetto, come accennato prima, al precedente lavoro fatto da Jacobson [8]. Come si può notare, i valori di deviazione standard nel caso in cui non viene utilizzata la matrice a priori, variano da un massimo di 5.233 km ad un minimo di 294 m per la posizione, e da un massimo di 7.2 m/s ad un minimo di $6.322 \cdot 10^{-2}$ m/s per la velocità. Jacobson, stimando tutti i satelliti tramite misure astrometriche, di tracking radiometrico e immagini, ottiene valori di deviazione standard compresi tra 10 e 1600 km, in particolare di 40 km in R, 150 in T e 50 in N per Titano.

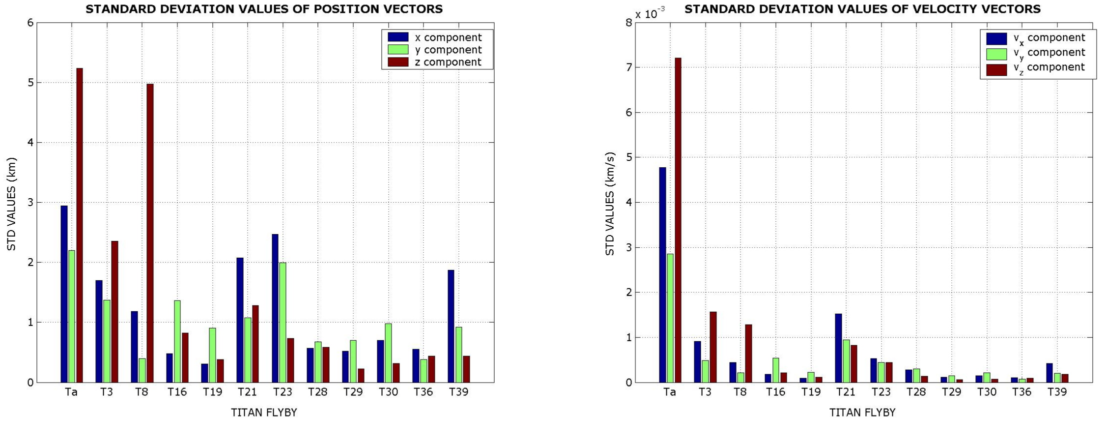

Figure 2: Deviazione standard dei vettori posizione e velocità ottenuti dai processi simulativi di determinazione orbitale senza l'uso della matrice di varianza a priori. I risultati dei flyby T13 e T25 non sono inclusi.

		position (km)		**velocity** (km/s)	
		value	$\boldsymbol{\sigma}$	**value**	$\boldsymbol{\sigma}$
Ta	x	90790.525887122727	2.9440	5.5819055604179333	4.7752E-03
2004 oct 26 15:40:00.0000 TDB	y	-1199096.8702990653	2.2010	0.5287902415603646	2.8570E-03
	z	72683.696103072813	5.2328	-0.5211272691898859	7.2062E-03
T3	x	87274.251869283093	1.7017	5.6038494837426098	9.1069E-04
2005 feb 15 06:20:00.0000 TDB	y	-1199526.7118605727	1.3677	0.5216955983513399	4.8789E-04
	z	73048.913198629612	2.3527	-0.5236462589797357	1.5680E-03
T8	x	-28411.947114015828	1.1801	5.6098905160979378	4.4396E-04
2005 oct 28 03:40:00.0000 TDB	y	-1204874.3297385797	0.3972	-0.0170421344191247	2.1091E-04
	z	83697.084967720904	4.9703	-0.4973570222043116	1.2787E-03
T13	x	-697190.40329855599	2.0621	-4.5393541600028380	7.8958E-03
2006 apr 30 21:00:00.0000 TDB	y	1037998.2779941373	6.9895	-2.9371701979330251	1.4919E-03
	z	-8581.1580313269133	48.7006	0.6410486250934060	2.3702E-02
T16	x	-1244986.6941283541	0.4764	-0.4521965877121465	1.8484E-04
2006 jul 21 23:20:00.0000 TDB	y	122907.95779253976	1.3644	-5.3852336263923322	5.3568E-04
	z	101553.09322396258	0.8267	0.4034803557739413	2.1801E-04
T19	x	-1244831.8356550639	0.3109	-0.4618691366535072	8.8171E-05
2006 oct 09 16:40:00.0000 TDB	y	125123.60402943045	0.9021	-5.3833573101367449	2.2372E-04
	z	101398.18302370311	0.3797	0.4054949744917004	1.1006E-04
T21	x	-1245733.3951738123	2.0727	-0.4211978077103663	1.5185E-03
2006 dec 12 12:00:00.0000 TDB	y	113963.34775349268	1.0784	-5.3844918197851150	9.3881E-04
	z	102235.55166288861	1.2812	0.3972387688240128	8.1909E-04
T23	x	-1242739.6849992662	2.4655	-0.5644528869519235	5.3211E-04
2007 jan 13 07:40:00.0000 TDB	y	147202.40915197050	1.9947	-5.4109008357353741	4.4343E-04
	z	99781.250334802389	0.7342	0.3890415401640619	4.3928E-04
T25	x	1175875.9729624467	112.559	0.7098084782556775	1.3299E-01
2007 feb 22 02:40:00.0000 TDB	y	-136831.39986573055	120.804	5.7435019151753206	1.5676E-01
	z	-94559.060560886181	31.840	-0.4072782136239315	4.0374E-02
T28	x	1173990.1626205295	0.5716	0.7413754756430268	2.7392E-04
2007 apr 10 22:00:00.0000 TDB	y	-151952.98153080599	0.6755	5.6647203933513897	3.0138E-04
	z	-93337.905377521194	0.5860	-0.4489225463615419	1.3532E-04
T29	x	1173926.1655281514	0.5185	0.7430029997321714	1.1979E-04
2007 apr 26 20:40:00.0000 TDB	y	-152491.00758121791	0.7035	5.6658372592139417	1.5045E-04
	z	-93306.390496484630	0.2239	-0.4472932586492427	6.3220E-05
T30	x	1172953.8982665027	0.6993	0.7785458663755382	1.5180E-04
2007 may 12 19:00:00.0000 TDB	y	-159771.73128275471	0.9781	5.6561877983858251	2.0972E-04
	z	-92669.078982320018	0.3171	-0.4627073555797382	6.9744E-05
T36	x	970318.12994343333	0.5514	3.2363470236583027	1.0389E-04
2007 oct 02 03:40:00.0000 TDB	y	-683158.18994310603	0.3833	4.6939375904908234	7.0512E-05
	z	-39493.444615246422	0.4377	-0.6021358192517183	8.7647E-05
T39	x	984147.20423707645	1.8673	3.1401328309200665	4.2020E-04
2007 dec 20 22:20:00.0000 TDB	y	-662675.71488640446	0.9225	4.7591812181829836	2.0345E-04
	z	-42080.310902837278	0.4358	-0.5993228227933789	1.8223E-04

Table 3: Stati di Titano risolti baricentricamente alle epoche in formato TDB scritte nella prima colonna. I dati altimetrici sono stati processati applicando la correzione per il tempo luce e senza ricorrere alla matrice di varianza a priori.

Sviluppi futuri

Il modulo software per la determinazione orbitale tramite l'utilizzo delle osservazioni altimetriche è stato sviluppato in maniera generale in modo tale da poter essere applicato a differenti scenari di missione in cui vi siano un corpo celeste osservato e un satellite artificiale che effettui le osservazioni. Si attendono per il loro processamento le osservazioni altimetriche degli ultimi flyby previsti dalla missione nominale e quelli che verranno effettuati durante la missione estesa. In tal modo avremo a disposizione un numero sufficiente di stati stimati con i quali ricostruire un'orbita più accurata di Titano ed utilizzarla per migliorare i risultati di altri obiettivi scientifici primari della missione. Alcuni flyby hanno residui di post-fit che mostrano andamenti sinusoidali più o meno accentuati e perciò richiedono una più approfondita indagine. Tale caratteristica potrebbe essere legata all'assetto del satellite oppure potrebbe trattarsi di

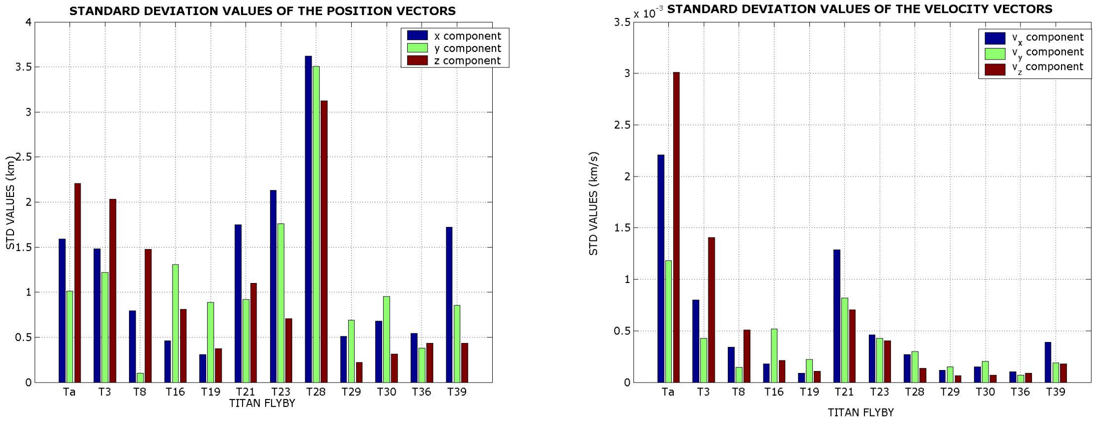

Figure 3: Deviazione standard dei vettori posizione e velocità ottenuti dai processi simulativi di determinazione orbitale con una matrice di varianza a priori di 25 km nella posizione e di $25 \cdot 10^{-6}$ nella velocità. I risultati dei flyby T13 e T25 non sono inclusi.

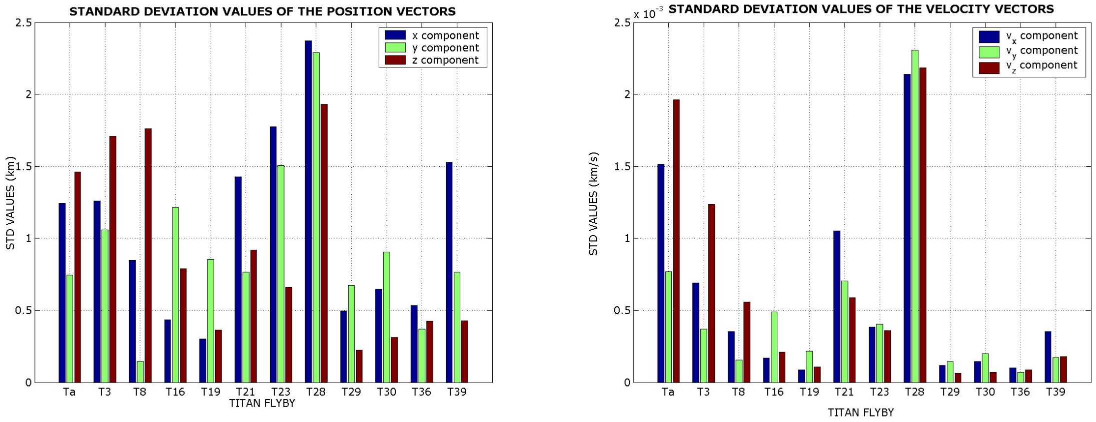

Figure 4: Deviazione standard dei vettori posizione e velocità ottenuti dai processi simulativi di determinazione orbitale con una matrice di varianza a priori di 9 km nella posizione e di $9 \cdot 10^{-6}$ nella velocità. I risultati dei flyby T13 e T25 non sono inclusi.

un ulteriore segnale sovrapposto ai dati altimetrici.

I dati altimetrici collezionati da RADAR sono misure molto accurate. Dal momento che abbiamo stimato solo Titano e su archi orbitali molto brevi, le soluzioni della stima dello stato del satellite sono particolari e locali rispetto alla soluzione trovata da Jacobson. Per poter ottenere una soluzione globale su tutto il tour sarebbe indicato adottare la tecnica di integrazione multiarco. Probabilmente tale approccio porterebbe ad ottenere stime più accurate dal momento che l'arco orbitale sarebbe più lungo e il numero di osservazioni processate contemporaneamente sarebbe maggiore.

SOSYA_ART sarà esteso dando all'utente la possibiltà di effettuare un'analisi di covarianza che quantifichi, senza ricorrere all'utilizzo delle osservazioni reali, l'impatto dell'introduzione dei dati di tipo altimetrico sulla stima dello stato del satellite in osservazione.

Il modulo di Simulazione delle Misure altimetriche sarà migliorato con la possibilità di introdurre disturbi al segnale iniziale.

Summary

The research presented in this thesis concerns the improvement of Titan's orbit determination by the means of the altimetric data captured by the Cassini's RADAR instrument. The work carries out the development and implementation in the SOSYA (SOlar SYstem Astrometry) software tool, of a module, called SOSYA_ART (SOlar SYstem Astrometry_Altimetric Run Tool), that computes bodies'Orbit Determination by an altimetric type process. Moreover, the Measurements Simulation part of SOSYA has been enriched the introduction of the module that creates synthetic altimetric measurements at given observation times set. This research can be divided in four parts.

The first part gives a brief introduction of the Cassini mission and a detailed description of the RADAR instrument on board the satellite with its features and scientific purposes. RADAR is a multimode instrument that uses the five beam antenna feed assembly associated with the spacecraft high gain antenna to transmit and receive electromagnetic radiation according to different operative modes: imaging mode, altimeter mode, radiometer and scatterometer mode. A precise observation sequence of observations is performed during each Titan's encounter: within 25,000 km range active scatterometer measurements start, then the low resolution altimeter mode is planned between 9000 and 22.500 while the high resolution altimeter mode is performed between 4000 and 9000 km. The imaging mode is selected while the spacecraft altitude passes from 4000 km to its minimum value, then outbound observations are repeated in reverse order.

Basic concepts of the radar theory and signal modulation are presented. Radar data acquisition is a type of remote sensing technique. These techniques acquire information detecting and measuring changes that the object causes on the surrounding field (potential, electromagnetic or acoustic field). In fact, radar altimetry involves bouncing microwave pulses off the surface of the target body and measuring the time it takes the echo to return to the spacecraft.

The second part is concerned with the fundamentals of orbit determination. Statistical orbit determination is the set of techniques that allows the estimation of the orbital parameters of a spacecraft or a celestial body during its motion in the Solar System. It is the problem of determining the best estimate of the orbital parameters of a spacecraft or a celestial body, whose initial state is unknown, from observations influenced by random and systematic errors, using a mathematical model that is not exact. Then we give the detailed development of the geometrical observation model used to determine the altimetric measurement for the residuals computation at each observation time.

The problem of orbit determination is solved by SOSYA_ART for Titan's state at epoch, t_0, keeping fixed the trajectory of Cassini spacecraft. Titan's surface is considered as a sphere of 2575 km radius and the problem is solved in the reference frame centered on the barycenter of the Saturnian system. At each observation time, Cassini's ephemeris and attitude values are read from SPICE's SPK and CK kernels files and corrected for light time, while Titan's states are integrated and interpolated by the means of SOSYA's Orbit Simulation capability [2]. Then, as the field of view direction of RADAR beam is strictly connected to the spacecraft's attitude, the intersection point with the surface is computed and residual value is found. The weighted least squares method is applied to fit to the observational data and the set of adjustable parameters are Titan's position and velocity.

The third part is dedicated to the altimetric data used and to the flybys during which they were collected by the Cassini RADAR. The altimetric observation processed in the software tool is the distance, or rather *the range-to-target (RTT)*, measured from the antenna's center of phase to the surface of the target body. The altimetric data have been received from CO.RI.S.T.A. (Consortium for Research on Advanced Remote Sensing Systems) and they have been collected in 12 of 44 Titan's flybys, beginning from the flyby completed on 26th October 2004 (Ta) and up to the one completed on 20th December 2007 (T39). The total number of altimetric measurements processed is 13080 and they are not uniformly distributed in the 14 flybys: T13 and T25 have the lowest numbers of observations so they are precessed but not included in results discussion. For each of these encounters we searched for the `SPK` kernels, containing Cassini's ephemerides, and the relative `CK` kernels, containing the spacecraft attitude matrices. In order to give a description of the flybys used in the Orbit Determination process, we implemented a simple SPICE-based routine that reads the ephemeris files and gives three output files containing respectively: 1) Cassini barycentric states, 2) Titan barycentric states and 3) Cassini states in Titan-centered reference frame. Then by the use of Matlab, the states have been plotted in order to visualize the entire encounters in two different ways: the first one is the Titan-centric representation of the flyby while the second one is the orthogonal projection on the xy plane of the Saturn-barycentric passage. For each available flyby, we give its general description, as duration and the closest approach distance and time. Moreover we give tables that summarize the distribution over time of the altimetric observation sequence.

The last part of the work is entirely dedicated to the Orbit Determination process and to the discussion about the solutions obtained for Titan's states computed at the batch epochs by SOSYA_ART. Since the altimetric observation errors were not available, we have used a constant value for the weight of 80 m for all the observations corresponding to the maximum resolution value that the instrument achieves approximatively. Titan's flybys T13 and T25 are have been processed but they are not discussed with the others results obtained because they have very few observations. The mean of all the rms values at first iteration is 4.703 km and it decreases to the value of 81.67 m at last iteration underlining the goodness of the solutions for Titan's states obtained with respect the initial ones. The global mean of residuals at the first iteration is -340 m and it decreases to the global mean at the last iteration of $-4.296 \cdot 10^{-4}$ km, giving the possibility of neglecting the bias estimation. The minimum value of standard deviation of the estimated position is 294 m, while the maximum value is 5.233 km. The standard deviation of the velocity ranges from a minimum of $6.322 \cdot 10^{-2}$ m/s to a maximum value of 7.2 m/s. Although our estimation has been made only for Titan and yields particular and local solutions, the results are fully satisfying. Jacobson [8] obtained 1-σ uncertainties for Titan of 40 km along R, 150 km along T and 50 km along N. These results come from astrometry, radiometric tracking and spacecraft imaging data and estimating all the major Saturnian satellites. The accuracy of our solution is limited by the altimetric measurement errors and by the a priori covariance matrix values applied to the initial conditions of the natural bodies integrated. In fact we proved that the standard deviation errors effectively decrease by the use of different a priori variance matrices. In addition, the resulting accuracy of the estimation is due to the short orbital arcs considered in the orbit determination process over which the measurements are taken.

Our research can be further extended to other mission scenarios in order to reach a better accuracy in the orbit determination of natural satellites by the means of altimetric data collected on board spacecrafts by radar or laser instruments.

New data sets coming from the last part of the nominal mission and from its extended part will be included in the research and processed by SOSYA_ART. In this way we have a sufficient numbers of points at which Titan's state has been computed and this becomes the basis on which starting the reconstruction of the improved moon's orbit together with the other types of observation. In order to compute a global solution all over the entire tour with more accurate estimation of Titan'state, a multi-arc approach would be probably indicated.

SOSYA_ART will be enriched by the consider covariance analysis module testing the impact of the introduction of the altimetric observations on the state estimation process without having the real data.

The altimetric measurements simulation module will be improved by the introduction of the possibility of adding noise to the signal.

Introduction

Cassini-Huygens is a planetary exploration mission, planned to make an exhaustive study of Saturn, its rings and satellites. The mission provided a great amount of data and information, giving an increase to the knowledge about the Solar System formation, the origins of life and about specific aspects of the Saturnian System.

Titan, the largest of Saturn's satellites, is very important for the mission and the Huygens probe was dedicated to its exploration. Titan is the only satellite in the Solar System to have a dense atmosphere rich in nitrogen. The analysis of Titan's internal structure and constitution is essential to determining the presence and the nature of a possible inner core. This investigation can be carried out by combining the analysis of Titan's gravity field and the analysis of its rotational state. In this sense the measure of the Titan's axial moment of inertia is the crucial quantity that poses limits to its internal constitution. In order to guarantee a good determination of the gravitational field, it is necessary to have an excellent estimate of the true Cassini trajectory and a very precise ephemerides of all the main bodies of the Saturnian system. Cassini's orbit can be accurately determined from the high accuracy, Earth-based, range and doppler tracking in Ka band with minor optimization of Titan's orbit and perhaps other perturbers'. On the other hand, for the successful completion of experiments, Titan's orbit needs to be determined with a good accuracy.

For this purpose it has been necessary to develop an adequate force model that considers all the perturbations that influence the motion of the spacecraft during the flybys descripted in details in [2]. The satellite ephemerides based on analytical theories are not accurate enough, making it necessary to generate the ephemerides by integrating numerically the satellite orbits. In addition, given the high accuracy of the measurements, it is possible to have very precise ephemerides of all the main bodies of the Saturnian system combining all observation types made by both Cassini's instruments and both from Earth in the orbit determination process. This is the purpose of SOSYA software [2] which can provide the Orbit Determination of Cassini spacecraft and the moons of Saturn by means of the optical, photometric, radiometric and altimetric data provided by the instruments on board the probe. Jacobson [8] developed new ephemerides for the major Saturnian satellites by means of astrometric, radiometric and imaging data types and with this research we want to prove that the introduction of the altimetric measurements can really improve the accuracies given by the orbit determination solution for Titan's state.

The altimetric measurements come from one of the experiments included in the scientific payload: it is the multimode radar which collects altimetric data on Titan's surface during the several encounters with the moon. The research presented in this thesis concerns the improvement of Titan's orbit determination by the means of the altimetric data captured by the Cassini's RADAR instrument and it carries out the implementation of the altimetric modules for SOSYA called SOSYA_ART (SOlar SYstem Astrometry_Altimetric Run Tool).

Satellite altimetry was developed in the 1970's to measure the geometric shape of the ocean surface and geoid heights. The first radar sounder flown has been ALSE (Apollo Lunar Sounder Experiment) on board Apollo 17 in 1972. The use of altimeters on board orbiting spacecraft has become a necessity in a number of geophysical disciplines because they allow the acquisition of global and synoptic coverage with relatively short repetitive period. These features are essential for observing dynamic atmospheric, oceanic, and biologic phenomena. As example, only from space oceans can be observed on a global scale and critical changes in currents and heat storage can be monitored. Satellites like TOPEX/Poseidon and Jason help to understand and foresee the effect of the changing oceans on the climate. The global coverage capability is also essential in a number of geologic applications.

Radar altimeters activity expanded dramatically using planetary mission and data were acquired on the surfaces of the Moon, Mercury, Mars and the Jovian and Saturnian satellites. Some sounder instruments flown are MARSIS (Mars Advanced Radar for Subsurface and Ionosphere Sounding) on board the ESA's Mars Express probe, and SHARAD (mars SHallow RADar sounder) on JPL's Mars Reconnaissance Orbiter (MRO). The sensors operates independently of Sun illumination and usually are not sensitive to weather conditions or cloud cover. For example, in the case of Venus and Titan, the continuous and complete cloud coverage limits surface observation to the longer wavelength, particularly radio frequency and microwave bands.

Satellite altimetry was first applied to radar technology and then a similar version using lasers has been used in space missions such as Mars Global Surveyor and the MESSENGER's Mercury Laser Altimeter, or MLA, which allowed scientists to correlate, for the first time, high resolution topography measurements with high resolution images.

The applications of the altimetric information for spacecraft motion have been investigated by Pelletier [16] for the NEAR mission. The spacecraft carried a laser altimeter to measure distances from the asteroid surface. The application of this information for spacecraft orbital motion are investigated using the crossover technique, and this involves shape modeling of the asteroid. This crossover method could not be applied to Titan case because the number of crossover points is not sufficient to set up a differential altimetry procedure.

In Chapter 1 we describe the Cassini-Huygens mission to Saturn with its scientific objectives and instruments. The attention is focused on the RADAR multimode instrument on board the probe and on the precise sequence of observations it performs.

Chapter 2 introduces the remote sensing technique and describes the sensors used by this data acquisition approach. In particular, we give the basic principles and theory of radar sensors and some of the physical properties of the electromagnetic signal. Cassini's RADAR instrument and the observation sequence performed during the closest approach with Titan are described in details.

Chapter 3 gives some generalities on the theory of statistical orbit determination with the mathematical tools needed by this investigation.

In Chapter 4 we present the altimetric observation model needed to obtain the computed altimetric measurement. The observation equation is developed in the Saturn's barycenter reference frame together with the geometric partials derivatives with respect Titan's state at epoch. The procedure used to get the intersection points of the radar beam with Titan's surface at the observation time is given.

Chapter 5 is devoted to the altimetric data files description and to the flybys during which these data have been collected.

Chapter 6 gives the results we obtained by the Titan's Orbit Determination processes with the altimetric data as input observations.

In Chapter 7 we give conclusions and suggestions for future work.

Appendix A gives the procedure to compute the synthetic altimetric data by the use of SPICE subroutines. The procedure completes SOSYA_ART and fulfill the Data Simulation capabilities of SOSYA.

Appendix B presents a description of the software tool SOSYA_ART.

Appendix C describes the SPICE function used to get Cassini's matrix attitude at a given time epoch.

Chapter 1

The Cassini Mission

1.1 Mission to Saturn

Saturn is the second most massive planet in the Solar System and offers a treasure of opportunities for exploration and discovery. The giant planet has a huge magnetosphere and a stormy atmosphere with super-fast winds that, combined with heat rising from within the planet's interior, cause the yellow and gold bands visible in its atmosphere. Its remarkable system of rings is a subject intensively studied, described and cataloged. In fact Saturn has the most extensive and complex ring system, extending hundreds of thousands of miles from the planet. Saturn's many known moons are equally mysterious, especially Titan. Bigger than Mercury and Pluto, Titan is of particular interest to scientists because it is one of the few moons in the solar system with its own atmosphere: the moon is cloaked in a thick, smog-like haze. In addition to Titan, Saturn has many smaller icy satellites each a separate world to explore in itself. Some, like Pan, Atlas, Prometheus, and Pandora, are "shepherd moons" that herd Saturn's orbiting particles into distinct ring. Some moons produce twisting and wave patterns in the rings. Saturn, its moons and its awesome rings sit inside the enormous cavity in the solar wind created by the planet's strong magnetic field. The field rotates with the planet, carrying with it a vast population of charged particles called a plasma. Saturn's magnetosphere is extensive and maintains dynamic interfaces with both the solar wind and with Titan's atmosphere.

The Cassini-Huygens mission is an international collaboration between three space agencies. Seventeen nations contributed to building the spacecraft. The orbiter, supplied by NASA, is named for Jean-Dominique Cassini, who discovered the satellites Iapetus, Rhea, Dione and Tethys, as well as ring features such as the Cassini division, in the period 1671-1684. The Titan probe, supplied by European Space Agency (ESA), is named for Christiaan Huygens, who discovered Saturn's largest satellite in 1655. The Italian space agency (Agenzia Spaziale Italiana, or ASI), through a bilateral agreement with NASA, provided hardware systems for the obiter spacecraft and the Cassini's high-gain communication antenna.

The Cassini spacecraft is the first to explore the Saturn system of rings and moons from orbit. After a 6.7-year Venus-Venus-Earth-Jupiter Gravity Assist (VVEJGA) trajectory Cassini entered Saturn's orbit in July of 2004 and immediately began sending back intriguing images and data. It has begun a four-year mission that includes more than 70 orbits around the ringed planet and its moons 45 of these are Titan targeted. The Huygens Probe dove into Titan's thick atmosphere in January 2005. Instruments on board collected information about the atmosphere's chemical composition and the clouds surrounding Titan. The data were radioed to the Cassini orbiter, which then relayed the data to Earth. The sophisticated instruments on both spacecrafts are providing scientists with vital data and the best views ever of this mysterious, vast region of our solar system.

Cassini's mission originally had been scheduled to end in July 2008 but NASA is extending the international Cassini-Huygens mission by two years. The spacecraft is performing exceptionally well and the extension will include 60 additional orbits of Saturn and more flybys of its exotic moons (26 Titan's flybys). This extended tour is responding to the new discoveries and giving a chance to look for more.

1.2 Instruments onboard the orbiter

The Cassini orbiter and the Huygens probe were equipped with an array of sophisticated instruments and cameras able to collect images in many varying conditions and light spectra; from visible light to the infrared. Twelve science instruments are mounted onboard the Cassini spacecraft and each instrument is designed to carry out sophisticated scientific studies of Saturn, from collecting data in multiple regions of the electromagnetic spectrum, to studying dust particles, to characterizing Saturn's plasma environment and magnetosphere. Cassini is capable of making a wide range of in situ and remote-sensing observations.

Science investigations can be divided into three different types:

- Optical Remote Sensing. The instruments involved are:
    1. **Composite Infrared Spectrometer (CIRS)**: it consists of dual interferometers that measure infrared emission from atmospheres, rings, and surfaces over wavelengths from 7 to 1000 micrometers (1400 to 10 cm-1) to determine their composition and temperatures.
    2. **Imaging Science Subsystem (ISS)**: it consists of a wide angle camera, with angular resolution of 60 microradians per pixel, and a narrow angle camera, with angular resolution of 6.0 microradians per pixel.
    3. **Ultraviolet Imaging Spectrograph (UVIS)**: the instrument measures the views in ultraviolet light. Ultraviolet is particularly interesting because it includes the light characteristics of some key chemical elements and compounds. These light patterns are like fingerprints in UVIS observations.
    4. **Visual and Infrared Mapping Spectrometer (VIMS)**: it has a pair of imaging grating spectrometers designed to measure reflected and emitted radiation.
- Fields, Particles and Waves
    1. **Cassini Plasma Spectrometer (CAPS)**: it measures the flux of ions as a function of mass per charge, and the flux of ions and electrons as a function of energy per charge and angle of arrival relative to CAPS.
    2. **Cosmic Dust Analyzer (CDA)**: it is intended to provide direct observations of particulate matter in the Saturnian system, to investigate the physical, chemical, and dynamical properties of these particles, and to study their interactions with the rings, icy satellites, and magnetosphere of Saturn.
    3. **Ion and Natural Mass Spectrometer (INMS)**: it is intended to measure positive ion and neutral species composition and structure in the upper atmosphere of Titan and magnetosphere of Saturn, and to measure the positive ion and neutral environments of Saturn's icy satellites and rings.
    4. **Dual Technique Magnetometer (MAG)**: the primary objective is to determine the planetary magnetic fields and the dynamic interactions in the planetary environment.
    5. **Magnetospheric Imaging Instrument (MIMI)**: it is designed to measure the composition, charge state and energy distribution of energetic ions and electrons, detect fast neutral species, and conduct remote imaging of the Saturn's magnetosphere.
    6. **Radio and Plasma Wave Science (RPWS)**: the major functions are to measure the electric and magnetic fields and electron density and temperature in the interplanetary medium and planetary magnetospheres.

- Microwave Remote Sensing
    1. **Cassini Radar (RADAR)**: it uses the five-beam Ku-band antenna feed assembly associated with the spacecraft high gain antenna to direct radar transmissions toward targets, and to capture blackbody radiation and reflected radar signals from targets (Section 1.3).
    2. **Cassini's Radio Science Subsystem (RSS)**: it studies the compositions, pressures and temperatures of the atmospheres and ionospheres of Saturn and Titan; the radial structure of Saturn's rings and the particle size distribution within the rings, and planet-satellite masses, gravity fields and ephemerides within the Saturn system. RSS is split in two parts: one resides on the spacecraft, the other at stations equipped to receive very stable radio signals at each of the three Deep Space Network complexes.

Once the spacecraft's onboard recording device reaches capacity, it points its high-gain antenna toward Earth and downloads the data through one of the 70-meter (230-foot) antennas of the Deep Space Network. Cassini is sending home several gigabytes of data daily.

1.3 The Cassini RADAR

Italian contribution provides Cassini with the core of the telecommunication system: the High-Gain Antenna. At the top of the Cassini stack is the large, four-meter-diameter High-Gain Antenna (HGA) and two low-gain antennas (LGA1 and LGA2). HGA is also used for radio and radar experiments and it was used for receiving signals from Huygens. The two microwave remote-sensing experiments, RADAR and RSS, share the spacecraft's HGA.

The Cassini RADAR is a multimode instrument working in Ku band (13.78 GHz). It uses the five beam antenna feed assembly associated with the spacecraft high gain antenna to transmit and receive electromagnetic radiation according to different possible operative modes: scatterometer mode, imaging mode, altimeter mode and radiometer mode. Each mode allows for the collection of different types of data, from straightforward imaging to 3-dimensional modeling to passive collection of information, such as simply recording the energy emanating from a planet's surface. RADAR scientific objectives are:

- to determine whether liquid surfaces exist on Titan, and, if so, to determine their distribution;
- to investigate the geologic features and topography of the solid surface of Titan;
- to acquire data on non-Titan targets (rings, icy satellites) as conditions permit.

In imaging mode the radar works as Synthetic Aperture Radar (SAR), that is an active mode able to provide a microwave image of the observed target with a relatively high spatial resolution (Section 2.4). SAR images is the sharpest that Cassini can achieve on the surface of Titan, with 350 to 1700 meter horizontal resolution. To collect SAR data, Cassini looks off to one side of the ground track as it flies by, instead of straight down as it does for altimetric measurements. The radio antenna chirps a signal at the planet, then listens for the echo and measures the delay time, the time between the chirp and the echo. But the echo is not exactly like the original chirped signal. The echo will be stretched out over time, because the signal returns first from the ground closest to Cassini, and later from the ground farther from Cassini. Also, the echo is Doppler shifted to slightly different wavelengths depending upon whether the echo comes from the ground ahead of the spacecraft along its track, which appears to be moving toward Cassini, shifting the wavelength shorter, or from the ground behind the spacecraft, which appears to be retreating and thus has a longer-wavelength shift. By processing the data into a map of echo strength in "delay-Doppler space" it can be seen how the strength of the signal varies relative to the spacecraft's position. This processing must be performed for each chirping signal produced by the spacecraft. SAR processing depends on incredibly accurate knowledge of the speed and position of the spacecraft relative to the surface that it is mapping. Instead of the inherent albedo, or brightness of the surface that is seen in optical images, SAR images show the strength of a reflected radio signal. Variation in the strength of a reflected radio signal can result from three main factors: slope, roughness, and dielectric constant.

Radar altimetry similarly involves bouncing microwave pulses off the surface of the target body and measuring the time it takes the echo to return to the spacecraft (Section 2.5.2). In this case, however, the goal is not be to create visual images but rather to obtain numerical data on the precise altitude of the surface features of Titan. In this mode, Cassini acquires profiles with 24 to 27 kilometer (15 to 18 mile) horizontal resolution and 90 to 150 meter (300 to 500 foot) vertical resolution.

In radiometer mode the radar operates as a passive instrument just recording the electromagnetic energy spontaneously radiated from the surface of Titan. This information stores the amount of latent heat in Titan's atmosphere, a factor that has an important impact on the precision of the other active radar measurements. Radiometry roughly correlates with temperature, and radiometry results are often described as brightness temperatures of surfaces. In this mode, Cassini can create maps of Titan with 7 to 310 kilometer pixel resolution. When it turns in the active mode, RADAR acts as a scatterometer. That is, it bounces pulses off Titan's surface and then measure the intensity of the energy returning. This returning energy or backscatter, is always less than the original pulse, because surface features inevitably reflect the pulse in more than one direction. From the backscatter measurements, scientists can infer the composition of the surface of Titan.

Here we give a table that summarizes the resolution values and characteristics of RADAR instrument (for details see [6]):

RADAR Sensing Instruments:	
Synthetic Aperture Radar Imager [SAR]	(13.78 GHz Ku-band; 0.35 to 1.7 km resolution)
Altimeter	(13.78 GHz Ku-band; 24 to 27 km horizontal, 90 to 150 m vertical resolution)
Radiometer	(13.78 GHz passive Ku-band; 7 to 310 km resolution)
RADAR Instrument Characteristics	
Mass (current best estimate)	41.43 kg
Peak Operating Power (current best estimate)	108.40 W
Peak Data Rate (current best estimate)	364.800 kilobits/sec

Table 1.1: Cassini's RADAR details.

1.3.1 RADAR observation sequence

Cassini completed 44 Titan encounters during its nominal mission. RADAR observations will not be made at all flybys, since some will be devoted to optical remote sensing, others are devoted to radio science and four are dedicated to gravitational measurements.

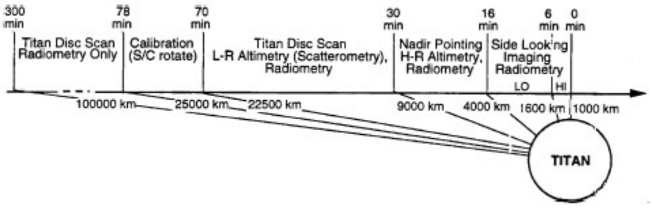

Figure 1.1: Timeline of a radar dedicated encounter, marked times before the closest approach. The sequence is repeated after the closest distance is reached.

As described in details by Lorenz et al. [12], on a RADAR dedicated flyby, observations begin several hours before the closest approach, at a range of around 100,000 km and a precise sequence of observations is performed (Figure 1.3.1). After a warm-up period to stabilize the noise diode reference and cold-sky measurements, the beam is pointed at Titan in the radiometric mode. At a range of 100,000 km the beam footprint is around 500 km across (a resolution of 1/10th of Titan's disk). The beam is moved in a spiral or raster pattern to cover the whole disk.

Within 25,000 km range (about 1 hour before the closest approach) active scatterometer measurements start. Radiometer observations can continue, although the incidence angles may be optimized for scatterometry, rather than the ridealong radiometry.

Within 10,000 km, altimeter observations are more useful, and the spacecraft is held nadir-pointing. Again, simultaneous radiometry is performed. The simultaneous radiometry and altimetry are of particular meteorological interest, since elevated terrain should be cooler by about 1 K/km due to radiative-convective temperature profile of Titan's atmosphere. Also in this case we have a high resolution altimeter mode between 4000 and 9000 km where the transmitted bandwidth is 4.25 MHz and the altimeter footprint is pulsewidth limited and is 24 to 27 km wide. The low resolution altimeter mode is planned between 9000 and 22.500 km and in this case the radar actually works as a scatterometer transmitting a waveform with a bandwidth of about 106 KHz to measure the average surface reflectivity over a beamwidth footprint up to 100 km wide ([13]).

The imaging mode is selected while the spacecraft altitude passes from 4000 km to its minimum value (1000 km from the surface of Titan). In particular in this time interval we have a high resolution imaging mode between 1000 and 1500 km where the radar image pixel is 380 (azimuth) × 600 (range) meters wide and a low resolution imaging mode between 1500 and 4000 km where the radar image pixel is 600 × 2500 m wide.
In any case the number of looks integrated to improve the radiometric quality of the image is ≥ 3, the incidence angle is included in the range $10° \div 30°$ and a quite simple unfocused processing algorithm can be used to obtain the radar images from the raw radar data.

Outbound, the altimeter, scatterometer and radiometry observations are repeated in reverse order. Titan'surface will be essentially covered completely at some incidence and polarization, with some repeated coverage to look for seasonal change and exploit multiple incidence angles.

Chapter 2

Remote Sensing

2.1 Introduction to the remote sensing

Remote sensing involves gathering data and information about the physical world by detecting and measuring radiation, particles, and fields associated with objects located beyond the immediate vicinity of the sensor devices. It is a technology essentially based on the acquisition of information about an object without being in physical contact with it. Information is acquired detecting and measuring changes that the object causes on the surrounding field (potential, electromagnetic or acoustic field). This could include an electromagnetic field emitted or reflected by the object, or perturbations of the surrounding gravity or magnetic potential field due to the presence of the object. Information acquisition is based on techniques that cover the whole electromagnetic spectrum, from the low-frequency radio waves to the gamma-ray regions of the spectrum.

Sensors on satellites orbiting around the Earth provide information about global patterns and dynamics of the atmosphere, surface vegetation cover, surface morphologic structures, ocean surface temperature and near-surface wind. The rapid wide coverage capability allows monitoring of rapidly changing phenomena while the long duration and repetitive capability allows the observation of longer term changes. The wide-scale coverage allows the observation and study of regional and continental scale features such plate boundaries and mountain chains.

Sensors on planetary probes are providing similar information about the planets and objects of the Solar System and this is what it's happening in the Saturnian system by means of information acquired by Cassini orbiter's instruments.

The basics scientific and engineering background of remote sensing and its applications are widely discussed by Elachi in [5]. In this chapter we give some scientific principles of the remote sensing technique and the description of the instruments involved of interest for this research.

2.1.1 Remote sensing data and sensor types

The type of remote sensing data acquired is dependent on the type of information being sought, as well as on the size and dynamics of the object or phenomena being studied [5]. Some different sensor types and their role in acquiring different types of information are illustrated in Figure 2.1 while Figure 2.2 summarizes the types of sensors now used or being developed in remote sensing. Passive sensors detect the reflected or emitted electro-magnetic radiation from natural sources, while active sensors detect reflected responses from objects which are irradiated from artificially generated energy sources, such as radar. Each is divided further in to non-scanning and scanning systems. A sensor classified as a combination of passive, non-scanning and non-imaging method is a type of profile recorder, for example a microwave radiometer. A sensor classified as passive, non-scanning and imaging method, is a camera, such as an

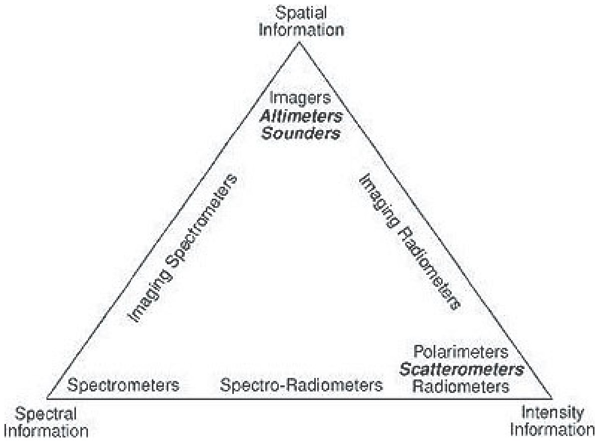

Figure 2.1: Diagram illustrating the different data types of information and the type of sensor used to acquire this information.

aerial survey camera or a space camera. Sensors classified as a combination of passive, scanning and imaging are classified further into image plane scanning sensors, such as TV cameras and solid state scanners, and object plane scanning sensors, such as multispectral scanners (optical-mechanical scanner) and scanning microwave radiometers. An example of an active, non-scanning and non-imaging sensor is a profile recorder such as a laser spectrometer and laser altimeter. An active, scanning and imaging sensor is a radar, for example synthetic aperture radar (SAR), which can produce high resolution, imagery, day or night, even under cloud cover. The most popular sensors used in remote sensing are the camera, solid state scanner, such as the CCD (charge coupled device) images, the multi-spectral scanner and in the future the passive synthetic aperture radar. Laser sensors have recently begun to be used more frequently for monitoring air pollution by laser spectrometers and for measurement of distance by laser altimeters.

As explained in Section 1.3, Cassini's RADAR operates as passive and active sensor depending on the acquisition of the different data type strictly connected to the observation sequence planned in the encounter with Titan.

2.2 Basic principles and theory of radar sensors

Radar is an acronym for RAdio Detection And Ranging. It operates in part of the microwave region of the electromagnetic spectrum, specifically in the frequency interval from 40,000 to 300 MHz. Commonly used frequencies and their corresponding wavelengths are specified by a band nomenclature, as in Table 2.1. Unlike other sensors that passively sense radiation from targets illuminated by the Sun or

Designation	Frequency range
`Ka Band`	40-26.5 GHz (0.8-1.1 cm)
`K Band`	26.5-18.5 GHz (1.1-1.7 cm)
`Ku Band`	18.5-12.5 GHz (1.7 - 2.4 cm)
`X Band`	12.5-8 GHz (2.4-3.8 cm)
`C Band`	8-4 GHz (3.8-7.5 cm)
`L Band`	2-1 GHz (15.0-30.0 cm)
`P Band`	1000- 300 MHz (30.0-100.0 cm)

Table 2.1: Band nomenclature and frequency ranges.

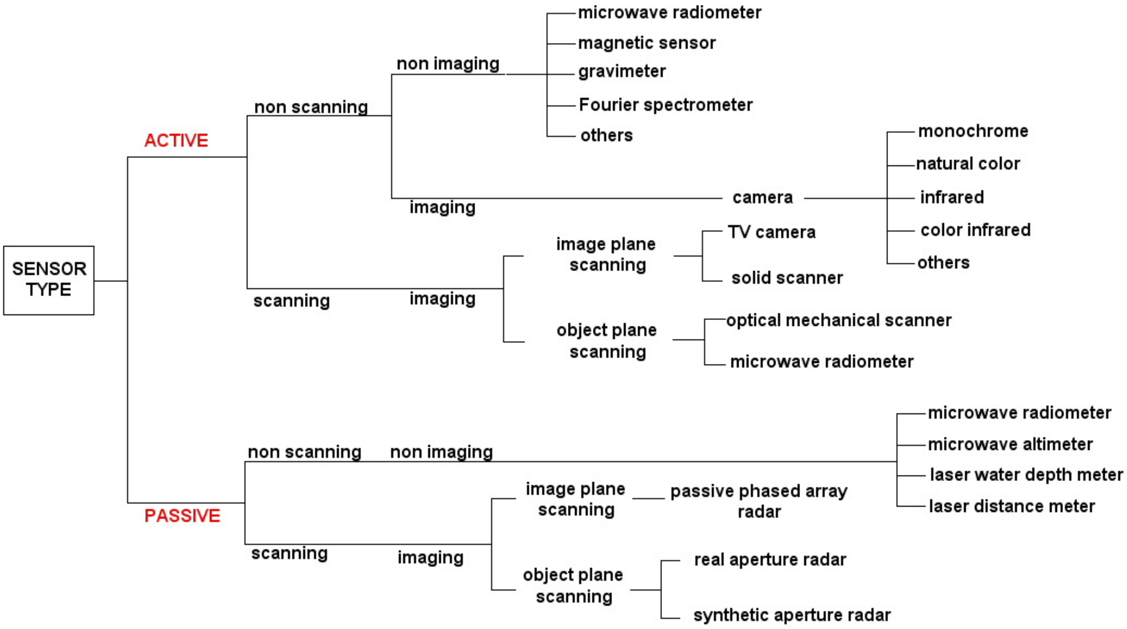

Figure 2.2: Diagram illustrating the different types of sensors now used or being developed in remote sensing.

thermal sources, radar generates its own illumination (hence it is active) by sending bursts or pulses of electromagnetic energy that reflect off of a target. A fraction of the reflected energy then returns to the radar's receiving antenna, which collects it and passes it to the electronic system. Thus, a radar system is a ranging device that measures distances as a function of round trip travel times (at light speed) of a directed beam of pulses (the signal, whose strength is measured in decibels, dB) spread out over specific distances. In this way radar determines the direction and distance from the instrument (fixed or moving) to an energy-scattering object. We can also derive information about target shapes and certain diagnostic physical properties of materials at and just below the surface by analyzing signal modifications. By supplying its own illumination, radar can function day and night and, for some wavelengths, without significant interference from blocking atmospheric conditions (e.g., clouds). Ground (fixed) and airborne (mobile) radar systems are used extensively today for marine navigation and air traffic control. Imaging radar, mounted on air or space platforms, has proven especially useful in mapping cloud-shrouded land surfaces. This use also permits expressing surface shapes in regions heavily covered by vegetation (penetrated by some bands).

Discernment between signals received from different parts of the illuminated scene may be performed by different techniques that involve angular, temporal or frequency separation. Some of the basic principles of radar sensors, designed for different applications, are discussed in the next paragraphs.

2.2.1 Properties of the signal: spectrum and modulation

Two general types of radar sensors exist: continuous wave and pulsed wave. In the second case, the number of pulses per second is called the pulse repetition frequency (PRF).

A signal $A(t)$ consisting of a single pulse of length τ and carrier frequency f_0 can be written as

$$A(t) = A\cos\omega_0 t \qquad -\frac{\tau}{2} < t \leq \frac{\tau}{2}, \tag{2.1}$$

where $\omega_0 = 2\pi f_0$. The bandwidth of a pulse is defined as

$$B = \frac{1}{\tau} \tag{2.2}$$

and it underlines the capability of the pulse to discriminate neighboring targets (i.e., sensor range resolution). If two target points are separated by a distance Δr, the two received echoes are separated by a time $\Delta t = 2\Delta r/c$. Thus it is necessary that $\tau < 2\Delta r/c$ in order for the the two echoes not to overlap. The shortest separation Δr that can be measured is given by

$$\Delta r = \frac{c\tau}{2} = \frac{c}{2B} \tag{2.3}$$

which is called range resolution. Thus, in order to obtain a high range resolution, a short pulse or a wide bandwidth pulse is needed.

The energy in a pulse is

$$E = P\tau, \tag{2.4}$$

where P is the instantaneous peak power, and the maximum power can be obtained by increasing the peak P or the pulse length τ. Thus, in order to achieve a high detection capability (large E) and a high resolution (large B), a pulse with the apparent incompatible characteristics of large τ and large B is needed. This problem is overcome by modulating the pulse.

Two types of modulation can be realized: linear frequency modulation, called FM chirp, and binary phased modulation. In the first case, the frequency f_0 is not kept constant throughout the pulse, but it is linearly changed from f_0 to $f_0 + \Delta F$ where ΔF can be positive (up chirp) or negative (down chirp). The bandwidth is independent of τ because

$$B = |(f_0 + \Delta f) - f_0| = |\Delta f|. \tag{2.5}$$

The mathematical expression for a chirp signal is

$$A(t) = \begin{cases} A\cos\left(\omega_0 t + \frac{\Delta\omega}{2\tau'}t^2\right) & \text{for } 0 \le t \le \tau' \\ 0 & \text{otherwise.} \end{cases} \tag{2.6}$$

The reason that a chirp signal of long duration can have a high range resolution is that at reception the echo can be inputted in a dispersive delay line which delays differently the parts of the pulse with different frequencies such that at the output the total energy is compressed into a much shorter pulse. The length of the output pulse and the compression ratio are respectively

$$\begin{aligned} \tau &= \frac{1}{B} = \frac{2\pi}{\Delta\omega} = \frac{1}{\Delta f}, && (2.7) \\ \frac{\tau'}{\tau} &= \tau'\frac{\Delta\omega}{2\pi} = \tau'\Delta f. && (2.8) \end{aligned}$$

Before compression, the separation of the echoes is allowed by the fact that the instantaneous frequency from each echo at a specific time in the overlap region is different.

In the case of binary phase modulation, the transmitted signal phase is changed by 180° at a specific time according to a predetermined binary code. At reception, a tapped delay is used. Some of the taps have 180° phase shifts injected in them with a pattern identical to the one in the transmitted pulse. So when the received echo is fully in the delay line, the output is maximum. One cycle earlier or later, there is mismatch between the received signal and the tapped delay line, leading to a much weaker output.

2.2.2 Range measurements and discrimination

Suppose that a shot pulse is transmitted toward a point target positioned at a distance R, then a short pulse echo will be received at a time $t = 2R/c$ where c is the speed of light. If the pulse has a length τ, the echo will have the same length. If two targets are separated by a distance ΔR, the shortest separation ΔR that can be measured is given by:

$$\Delta R = \frac{c\tau}{2} = \frac{c}{2B} \tag{2.9}$$

which is called range resolution. In order to achieve a good resolution, a short pulse or a wide bandwidth pulse, compressed into a short pulse, are needed.

Range discrimination can also be obtained by using frequency modulation, which consists on a long continuous signal transmitted with a linearly swept frequency. The echo is mixed with a signal identical to the signal being transmitted with an appropriate time delay. The resulting low passed signal has a frequency proportional to the range. Mathematically,

$$V_t(t) \sim \cos(\omega_0 t + \pi a t^2) \tag{2.10}$$

$$V_r(t) \sim V_t\left(t - \frac{2R}{c}\right) \sim \cos\left[\omega_0\left(t - \frac{2R}{c}\right) + \pi a\left(t - \frac{2R}{c}\right)^2\right] \tag{2.11}$$

are the transmitted and received signals respectively. After mixing, the output signal is the product of these two signals and it gives

$$V_0(t) \sim \cos\omega_t t \cos\omega_r t = \frac{1}{2}\cos(\omega_t + \omega_r)t - \frac{1}{2}\cos(\omega_t - \omega_r)t \tag{2.12}$$

where ω_t and ω_r are the instantaneous angular frequencies. After the sum frequency is filtered out, the resulting signal is given by

$$V_0(t) \sim \cos(\omega_t - \omega_r)t = \cos\left(\frac{2\omega_0 R}{R} + \frac{4\pi a R t}{c} - \frac{4\pi a R^2}{c^2}\right) \tag{2.13}$$

which has a frequency $f = 2aR/c$. If there are two targets separated by ΔR, the output signals will be separated in frequency by

$$\Delta f = \frac{2a\Delta R}{c} \tag{2.14}$$

and it should be

$$\frac{2a\Delta R}{c} > \frac{1}{\tau} \Longrightarrow \Delta R > \frac{c}{2a\tau} = \frac{c}{2B} \tag{2.15}$$

which is identical to Equation (2.9).

2.2.3 Doppler measurements and discrimination

Doppler shift results from the motion of the sensor and/or motion of the targets, thus the received echo has frequencies shifted away from the transmitted frequency by the corresponding Doppler frequencies f_{dn}. The received signal is

$$V_r(t) = \sum_n a_n \cos(\omega_0 t + \omega_{\mathrm{dn}} t). \tag{2.16}$$

In the case of a pulse signal, the echo will have the same spectrum as the transmitted signal but shifted by $f_{\mathrm{d}} = 2(v/c)f_0$ where v is the apparent relative velocity of the target. If there are two targets with apparent velocities v and $v + \Delta v$, the echo contains Doppler shifts at f_{d} and $f_{\mathrm{d}} + \Delta f_{\mathrm{d}}$. In order to separate the two targets, we need

$$\Delta f_{\mathrm{d}} > \frac{1}{nT} \Longrightarrow \frac{2\Delta v}{c} f_0 > \frac{1}{nT} \tag{2.17}$$

or

$$\Delta v \geq \frac{\lambda \mathrm{PRF}}{2n} \tag{2.18}$$

which is called Doppler resolution. The maximum Doppler shift cannot exceed $1/T = \mathrm{PRF}$, otherwise ambiguity occurs.

2.3 Imaging sensors: Real Aperture Radars (*RAR*)

The real aperture imaging technique leads to an azimuth resolution which is linearly proportional to the distance between the sensor and the surface. Therefore, *RARs* are used for scatterometry and altimetry and they are not used in the cases when the objective is to have high resolution imaging.

2.3.1 Range and azimuth resolutions

The range resolution is the minimum distance between two points on the surface which can still be separable. If the distance between two points is X_r, their respective echoes are separated by the time difference (Fig. 2.3)

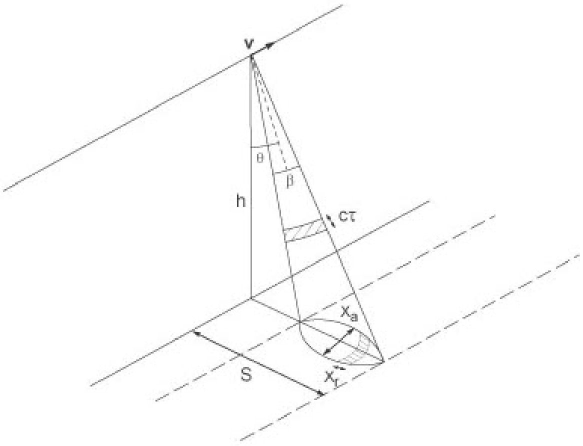

Figure 2.3: Geometry of a real aperture radar.

$$\Delta t = \frac{2X_r}{c}\sin\theta. \tag{2.19}$$

If the smallest discriminable time difference is $\tau = 1/B$, the range resolution is given by

$$2\frac{X_r}{c}\sin\theta = \tau \Rightarrow X_r = \frac{c\tau}{2\sin\theta} = \frac{c}{2B\sin\theta}. \tag{2.20}$$

The azimuth resolution correspond to the two nearest separable points along an azimuth line, that is, on a constant delay time. It is equal to the width of the antenna footprint because the echoes from all the points along a line spanning that width are returned at the same time:

$$X_a = \frac{h\beta'}{\cos\theta} = \frac{h\lambda}{L\cos\theta} \tag{2.21}$$

where β' is the antenna beam width in azimuth.

2.3.2 Radar equation

One of the factors that determines the quality of the images acquired with an imaging radar sensor is the signal-to-noise ratio for a pixel element in the image. In order to find out this factor, let consider the transmitted peak power P_t and the gain of the antenna $G = 4\pi A/\lambda^2$. The power density per unit area incident on the illuminated surface is

$$P_i = \frac{P_t G}{4\pi r^2}\cos\theta, \tag{2.22}$$

and the backscattered power is then equal to

$$P_s = P_i S \sigma \tag{2.23}$$

where S is the area illuminated at a certain instant of time ($S = X_a X_r$) and σ is the surface backscatter cross section. In the neighborhood of the sensor, the reflected power density is

$$P_c = \frac{P_s}{4\pi r^2} \tag{2.24}$$

and the total power collected by the antenna is

$$P_r = AP_c = \frac{P_t}{8\pi} \frac{W^2 L}{\lambda h^3} \frac{c\sigma}{B} \frac{\cos^4 \theta}{\sin \theta}. \tag{2.25}$$

The thermal noise in the receiver is given by

$$P_N = kTB \tag{2.26}$$

where k is the Boltzmann constant and T is the total noise temperature. The signal-to-noise ratio is then

$$SNR = \frac{P_r}{P_N} = \frac{P_r}{kBT}. \tag{2.27}$$

There are a number of factors which could improve the SNR and one such factor is the use of a dispersed pulse with a compression ratio $l = \tau/\tau' = \tau' B$, where τ' is the disperse pulse length. This improves the SNR by l, which commonly exceed 20 dB.

2.4 Imaging sensors: Synthetic aperture radars (*SAR*)

The azimuth resolution of a real aperture radar is given by Equation 2.21. In order to improve this resolution, the synthetic aperture radar technique is used. The target stays in the beam for a significant amount of time, and it is observed by the radar from different positions along the satellite path. Two approaches can be used to explain the synthetic aperture technique and they are presented in the following paragraphs [5].

Synthetic array approach

Let us assume a sensor has an antenna of length L and it is moving at a velocity v. The footprint of the main beam on the surface is equal to

$$\mathcal{L} = \frac{2\lambda h}{L} \tag{2.28}$$

When the sensor moves, echoes are recorded at points $X_1, X_2 \ldots X_i$, along the flight line as represented in Figure 2.4. The echoes are recorded coherently, that is, amplitude and phase as a function of time, with a stable oscillator used as reference and combined to synthesize a linear array. The maximum array length achieved is equal to $\mathcal{L}$, the beam width and the footprint of the synthesized array are

$$\theta_s = \frac{\lambda}{\mathcal{L}} = \frac{L}{2h} \tag{2.29}$$

$$X_a = h\theta_s = \frac{L}{2}. \tag{2.30}$$

This is the better resolution that could be achieved using the synthetic array. The result in 2.30 is independent of the distance between the sensor and the area being observed. In addition, finest resolution can be achieved with the smaller antenna. This is explained in the following way. The farther sensor is, the larger the footprint is on the ground, thus the longer the synthetic array. This leads to a finer synthetic beam, which exactly counter-balances the increase in distance. The smaller antenna is, the larger the footprint and the synthetic array. This leads to a finer synthetic beam, therefore a finer resolution.

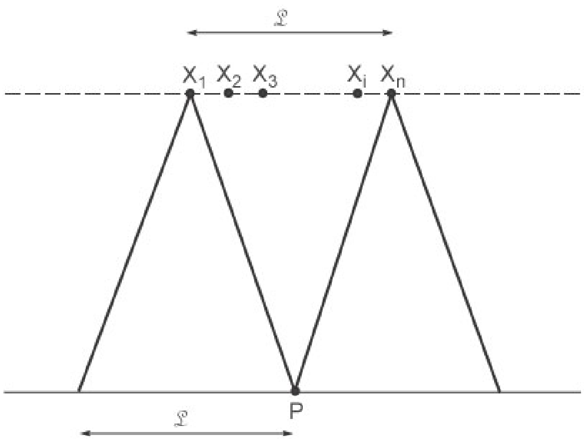

Figure 2.4: Geometry showing the formation of a synthetic array by moving a single antenna along a track.

Doppler Synthesis approach

When the target point P enters the beam, the echo will have a positive Doppler shift which decreases down to zero, then the shift becomes negative when P exits the beam (Figure 2.5). The spectrum covers the frequency region $f_0 \pm f_D$, where f_0 is the transmitted signal frequency and

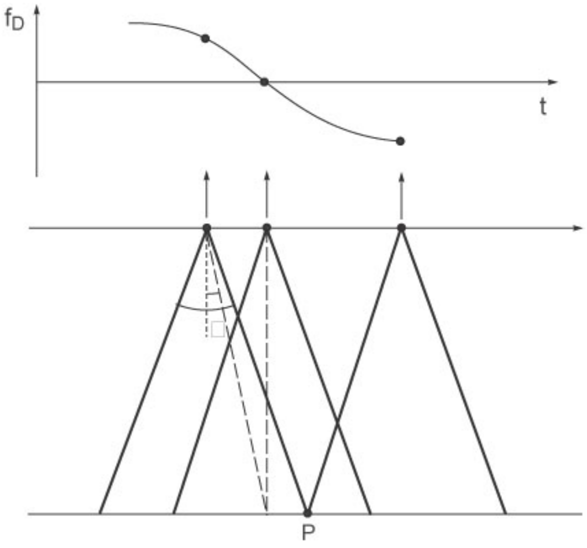

Figure 2.5: Doppler history of point P as the sensor passes by.

$$f_D = \frac{2v}{\lambda}\sin\frac{\theta}{2} \simeq \frac{v\theta}{\lambda} = \frac{v}{L}. \tag{2.31}$$

If a neighboring target P' is displaced from P by a distance X_a along the azimuth dimensions, the Doppler history of P' will be a replica of the Doppler history of P with a time displacement $t = X_a/v$. The shortest time displacement that can be measured is

$$t_m = \frac{1}{B_D} = \frac{1}{2f_D} = \frac{L}{2v}, \tag{2.32}$$

where $B_D = 2f_D$ is the spectrum bandwidth. Then, the finest possible resolution is

$$X_a = vt_m = \frac{L}{2}, \tag{2.33}$$

which is the same derived using the synthetic array approach (eq. 2.30).

The range resolution is the same as in the case of real aperture radar (see Equation 2.20), and it is not dependent on the altitude of the sensor. In fact, the imaging mechanism uses the Doppler shifts in the echo and the differential time delays between points on the surface, neither of which is a function of the distance between the sensor and the surface. The altitude still plays an important role in determining the power required to acquire a detectable echo and in determining the size on the antenna.

SAR imaging coordinate system

The coordinate system for synthetic aperture radar imaging are represented in Figure 2.6. Points located on a sphere centered at the radar location have their echoes received simultaneously. Thus a family of concentric spheres intersecting with the plane being imaged gives a series of concentric circles, centered at the nadir point, which define lines of equidistance to the sensor. Points located on coaxial cones, with the flight line as the axis and the radar location as the apex, have returned echoes with identical Doppler shifts. The intersection of the cones with the surface gives a family of hyperbolas. Objects located on some of these hyperbolas, provide equi-Doppler returns. As consequence, a coordinate system consisting of concentric circles and coaxial hyperbolas lays on the surface: each point on the surface is uniquely identified by its time delay and its Doppler shift. The potential ambiguity, due to symmetry between the right and the left region of the flight track, is avoided by illuminating only one side of the track (side illumination).

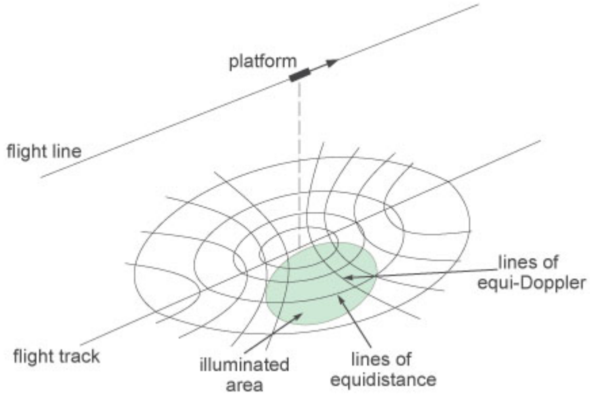

Figure 2.6: Coordinate system for SAR.

The brightness assigned to a specific pixel in the radar image is proportional to the echo energy contained in the time delay bin and Doppler bin, which correspond to the equivalent point on the surface illuminated.

SAR system modes

Three basic operating modes of a SAR system exist: *stripmap* (mode used by Cassini RADAR), *scan* and *spotlight* [7]. A common characteristic of these sensors is the side-looking view with respect to the flight track, necessary to avoid the ambiguity discussed before. The most used is the strip mode: the radar antenna points along a fixed direction with respect to the flight platform path, and the antenna footprint covers a strip on the illuminated surface as the platform moves. The strip SAR image is limited in the range direction but not in the azimuth direction. The strip mode involves two imaging geometries: the most conventional one is referred to as *boresight*, with the antenna beam pointing in the plane perpendicular to the flight direction. The other geometry is the *squinted* one, with the antenna making a pointing angle with respect to the boresight direction. The squint angle can reach some tens of degrees and it is useful in several applications, for example in the analysis of the backscattering properties of the illuminated surface with respect to the azimuth direction.

The scan mode increase the range swath dimension by stepping the antenna beam periodically to the neighboring subswaths (in the range direction). This causes a degradation of the achievable azimuth resolution with respect to the strip case. This mode allows an interferometric extension, but a careful synchronization between the acquisitions is required for two pass operations.

In the spot mode the radar antenna is steered during the overall acquisition time to illuminate the same area. The available synthetic antenna length can be increased with respect to the strip mode, thus improving azimuth resolution; this gain is traded off by loss of coverage due to the limited area illuminated.

2.5 Non imaging sensors

2.5.1 Scatterometer

Scatterometers are radar sensors which provide the backscattering cross section of the surface area illuminated by the sensor antenna. They usually have a large footprint and are for the most part used in studying average scattering properties over large spatial scales. They have been particularly useful in measuring the ocean backscatter cross section as a means of deriving the near-surface wind vector. The physical basis for this technique is that the strength of the radar backscatter is proportional to the amplitude of the surface capillary and small gravity waves, which in turn is related to the wind speed near the surface. Moreover, the radar backscatter can be measured at different azimuth angles, allowing the determination of the wind direction. Different configurations are used (Figure 2.7). The side-looking fan beam scatterometer allows sensing of a wide swath. The forward-looking fan beam scatterometer allows measurement only along the flight track. The tilted fan beam allows wide swath sensing and, with multiple beams, multiple look directions measurement. The scanning pencil beam scatterometer provides backscatter measurement at a constant angle and a dual look direction over a wide swath.

2.5.2 Altimeter

Altimeters use the ranging capability of radar sensors to measure the surface topographic profile. An altimeter measures the two-way travel time required for a radar pulse to be emitted by the altimeter antenna, travel to and reflect off the surface and then return to the antenna [15]. The geometry of the satellite altimeter measurement is shown in Figure 2.8. Ignoring delays due to the atmosphere, the altitude measurement is given by

$$h = \frac{ct}{2} \tag{2.34}$$

with an accuracy of:

$$\Delta h = \frac{c\tau}{2} = \frac{c}{2B} \tag{2.35}$$

where t is the time delay between the transmitted signal and the received echo. This altitude is the distance between the sensor and the portion of the surface illuminated by the antenna beam or by the pulse footprint. In the first case the footprint is given by

$$X = \frac{\lambda h}{L} \tag{2.36}$$

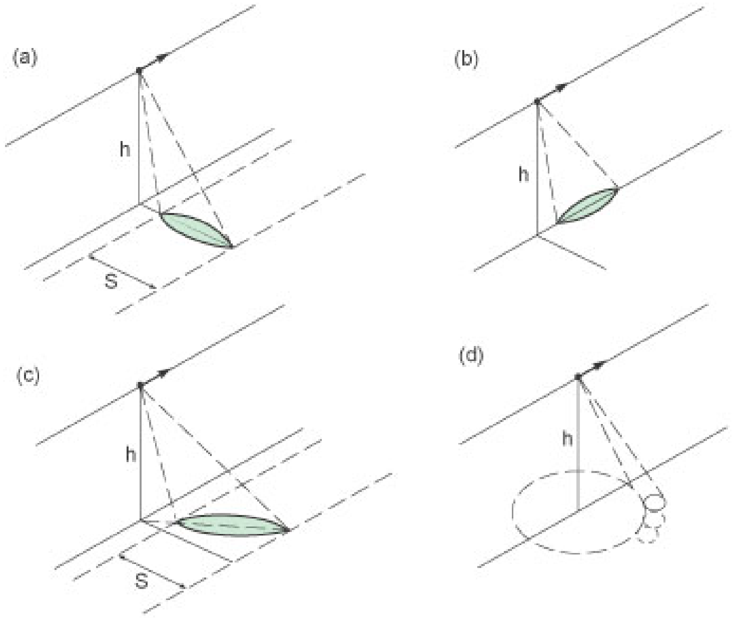

Figure 2.7: Different scatterometer configurations: (a) side looking fan beam; (b) forward looking fan beam; (c) tilted fan beam, and (d) scanning pencil beam.

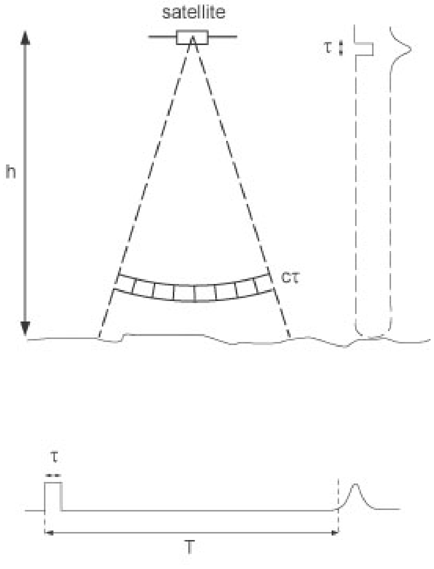

Figure 2.8: Altimeter measurement geometry.

and it corresponds to the beam limited altimeter, commonly used for land topography mapping. In the second case the footprint is given by

$$X = 2\sqrt{c\tau h} \tag{2.37}$$

which corresponds to a pulse limited altimeter, commonly used over relatively smooth areas such as the ocean surface.

2.6 Radar observations on Titan

Titan is of great interest to scientists because it is the only moon known to have clouds and a mysterious, planet-like atmosphere. Its unique environment and thick atmosphere may resemble that of Earth some several billion years ago, before life as we know it began pumping oxygen into our atmosphere.

The science objectives of Titan include [14]:

1. Determine the most abundant elements, and most likely scenarios for the formation and evolution of Titan and its atmosphere.

2. Determine the relative amounts of different components of the atmosphere.

3. Observe vertical and horizontal distributions of trace gases; search for complex molecules; investigate energy sources for atmospheric chemistry; determine the effects of sunlight on chemicals in the stratosphere; study formation and composition of aerosols (particles suspended in the atmosphere).

4. Measure winds and global temperatures; investigate cloud physics, general circulation and seasonal effects in Titan's atmosphere; search for lightning.

5. Determine the physical state, topography and composition of Titan's surface; characterize its internal structure.

6. Investigate Titan's upper atmosphere, its ionization and its role as a source of neutral and ionized material for the magnetosphere of Saturn.

7. Determine whether Titan's surface is liquid or solid, analyze the evidence of a bright continent as indicated in Hubble images taken in 1994.

The following table shows which instruments on the spacecraft support the corresponding science objectives above.

	CAPS	CDA	CIRS	INMS	ISS	MAG	MIMI	RADAR	RPWS	RSS	UVIS	VIMS	HUYGENS
1.	✓		✓	✓			✓			✓	✓	✓	✓
2.	✓		✓	✓	✓	✓				✓	✓	✓	✓
3.			✓			✓			✓	✓	✓	✓	✓
4.			✓			✓			✓	✓	✓	✓	✓
5.								✓		✓			✓
6.	✓			✓		✓	✓		✓	✓	✓		
7.								✓		✓			✓

Table 2.2: Science objectives of the instrument onboard.

As we can see, Cassini RADAR instrument is used to determine fundamental Titan's surface features.

Since the first two swath collected by Cassini's Titan Radar Mapper (images taken during Ta and T3 flybys and discussed in depth by Stofan et al. [20]), the significant differences between the terrains of the two swaths suggested that Titan is geologically complex. The limited amount of radar coverage at the end of the prime mission is up to 20% and this unfortunately limit the ability to interpret Titan in terms of the global balance on endo- and exogenic processes, and hence extended mission radar coverage is essential to understand the nature of and extend to which internal and external processes have shaped Titan's surface.

2.6.1 Titan's surface features interpretation

RADAR data illustrate the great diversity of Titan's surface and the large number of processes that are at play on that surface, from winds, to the action of liquids, to the possibility of volcanism involving warm ice or liquid ammonia-water. Titan's surface has been modified by both endogenic (volcanism, tectonism) and exogenic (impact cratering, erosion) processes, with no process dominating in an obvious way.

Cryovolcanic units have been identified in SAR images mostly at mid-latitudes (40-60 N), several calderas with associated flows, and large cryovolcanic flows. Flybys over high northern latitudes have shown lacustrine features, the distribution of these features is consistent with colder temperatures and more precipitation at high latitudes. Ridges and mountains that are interpreted to be of tectonic origin have been seen mostly at low latitudes, while drainage channels appear common at all latitudes. Fields of dunes (Titan's "sand seas") are mostly equatorial. Erosion by fluvial processes is likely to have occurred on a global scale. The small number of definitive impact craters suggests that these geologic processes are erasing or burying the majority of impacts.

As we can see Titan is a world with a complex history that the Cassini orbiter and the Huygens probe together elucidate.

2.6.2 Craters

RADAR-SAR images show some features that look like impact craters (Figures 2.9) because they have similarities to multi-ringed structures on the Moon and other solar system bodies. Brightness in SAR images can result from one of three effects: the slope of the surface (it's brighter if it tilts toward the spacecraft), the roughness of the surface (if it's bumpy on the same scale as the radio wavelength), and the intrinsic radio scattering properties of the surface material.

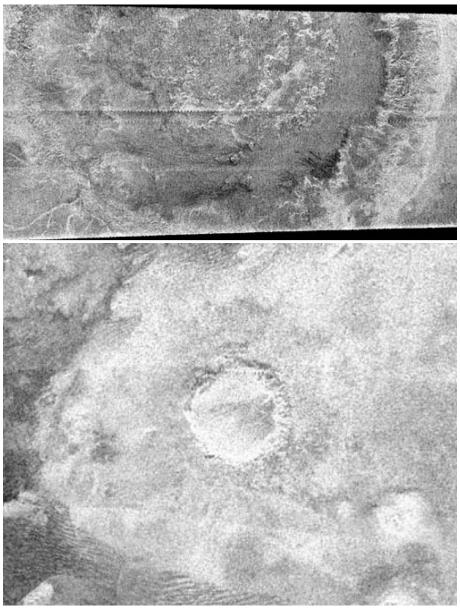

Figure 2.9: This is apparently the lower half of an enormous multi-ringed impact basin to the northeast of the bright region on Titan known as Xanadu. The basin is being referred to as "Circus Maximus" by the science team. The entire basin is about 440 kilometers (273 miles) across, or nearly ten percent the diameter of Titan. Image: NASA/JPL.

Craters are important because they are tools used by planetary geologists to figure out the age of planetary surfaces and the history of geologic events. Therefore, identifying them helps to begin to put Titan's history into a timeline. The overall scarcity of impact craters provides evidence that the surface imaged to date is relatively young, with resurfacing by cryovolcanism, fluvial erosion, aeolian erosion, and likely atmospheric deposition of materials.

2.6.3 Channels

Cassini radar images contains interesting channel features (Figures 2.10), often several hundreds of kilometers in length. Some are radar-bright and braided, resembling desert washes where fines have been removed by energetic surface liquid flow, presumably from methane rainstorms. Others are radar-dark and meandering and drain into or connect polar lakes, suggesting slower-moving flow depositing fine-grained sediments. A third type have radar brightness patterns indicating topographic incision, with valley widths of up to 3 km across and depth of several hundred meters. These observations show that fluvial activity occurs at least occasionally at all latitudes, not only at the Huygens landing site, and can produce channels much larger in scale than those observed there.

Figure 2.10: This area contains very primitive-looking channels. Image: NASA/JPL

2.6.4 Lakes

The existence of oceans or lakes of liquid methane on Saturn's moon Titan was predicted more than 20 years ago. But with a dense haze preventing a closer look it has not been possible to confirm their presence. Until the Cassini flyby of July 22, 2006, when scientists report definitive evidence of the presence of lakes filled with liquid methane on Saturn's moon (Figures 2.11). More than 75 radar-dark patches or lakes were seen, ranging from 3 kilometers (1.8 miles) to more than 70 kilometers (43 miles) across.

Radar-dark patches in Figure 2.11 are interpreted as lakes because they show very low radar reflectivity and morphological similarities to lakes, including associated channels and location in topographic depressions. Some lakes appear partly dry, while others seem liquid-filled. Some of the partly filled lakes may never have filled fully, or may have partly evaporated at some point in the past. The dry lakes have margins or rims and a radar brightness similar to the rest of the surrounding terrain, making them appear devoid of liquid. Approximately 15 of the dark patches seem filled and show no clear evidence of erosion. These dark patches resemble terrestrial lakes confined within impact basins or within volcanic calderas. The nest-like nature of these lakes and their limited range of sizes make that they have a volcanic origin. Some lakes have steep margins and very distinct edges, suggesting a topographic rim while other lakes have diffuse, more scalloped edges, with a gradual decrease in radar brightness towards the center of the lake. These lakes are more likely to be associated with channels, and may be either drainage lakes or groundwater drainage lakes. Bright patches near the lake edges could be small islands peeking through the surface. Floating "icebergs" are unlikely because most materials would not float in liquid hydrocarbons.

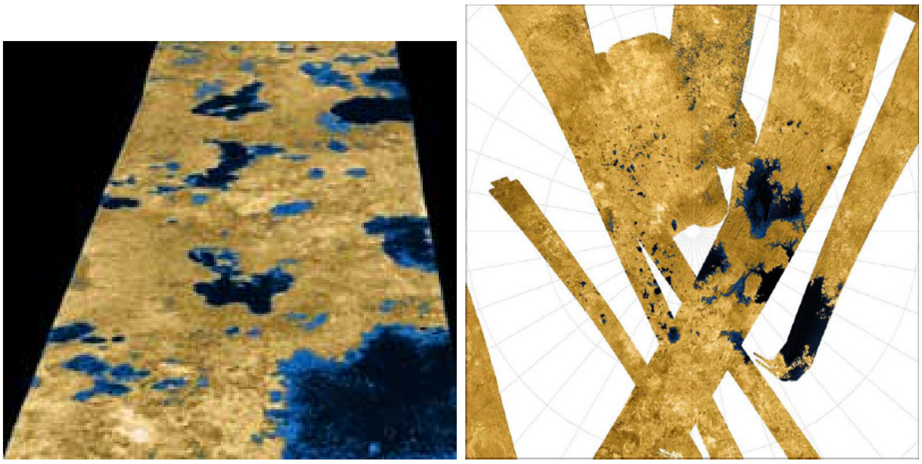

Figure 2.11: This is an example in false color image from the radar instrument illustrating the distribution of lakes on Titan.Image: NASA/JPL

2.6.5 Dunes

Recently longitudinal dunes (Figure 2.12) have been discovered by the Radar Mapper on the surface. Their longitudinal duneform, interactions with topography, and correlation with other aeolian forms indicate a single, dominant wind direction aligned with the dune axis plus lesser, off-axis or seasonally alternating winds. Global compilations of dune orientations reveal the mean wind direction is dominantly eastwards, with regional and local variations where winds are diverted around topographically high features, such as mountain blocks or broad landforms.

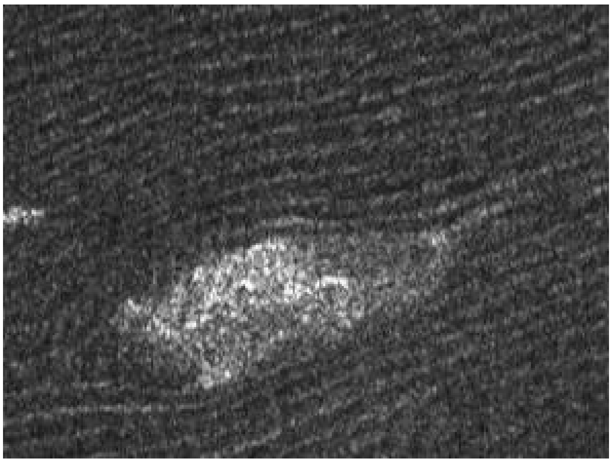

Figure 2.12: Details of dunes from a Cassini RADAR image.Image: NASA/JPL

Chapter 3

Fundamentals of Orbit Determination

3.1 Introduction

The problem of determining the best estimate of the orbital parameters of a spacecraft or a celestial body, whose initial state is unknown, from observations influenced by random and systematic errors, using a mathematical model that is not exact, is referred to as the process of *orbit determination.* The word "best" is used to imply that the estimate is optimal in a statistical sense.

The classical orbit determination problem is characterized by the assumption that the bodies move under the influence of a central force. For the satellite orbit determination problem the minimal set of parameters is the position and velocity vectors at some given epoch. This minimal set will be expanded to include dynamic and measurement model parameters, which may be needed to improve the prediction accuracy. If we denote the general state vector at a time t as $\mathbf{X}(t)$, the general orbit determination problem can be posed as follow.

If at some initial time, t_0, the state $\mathbf{X}_0$ of a vehicle following a ballistic trajectory is given and if the differential equations that govern the motion are known, then the equations of motion can be integrated to determine the state of the vehicle at any time. In such a way the vehicle will follow a design trajectory. However, during an actual flight, the initial state is never known exactly, hence the true initial state, $\mathbf{X}_0$, will differ from the nominal initial state, $\mathbf{X}_0^*$. Moreover, certain physical constants as well as the mathematical specification of the forces required to define the differential equations of motion are known only approximately. Such errors will cause the actual motion to deviate from the predicted motion, the true trajectory followed by the vehicle will differ from the nominal trajectory. Consequently, in order to determine the position of the spacecraft at some time $t > t_0$, it must be tracked or observed from tracking stations whose positions are known precisely. With the observations of the spacecraft motion, a better estimate of the trajectory can be determined. The estimate of the trajectory will not be exact because the observations will be subject to both random and systematic errors.

When an estimate of the trajectory has been made, the subsequent motion (spacecraft's position and velocity as functions of time) and values for the observations can be predicted. These predicted values will differ from the true values due to the following effects:

1. inaccuracies in the estimated state vector caused by errors in the orbit determination process, such as:
    - approximations involved in the method of orbit improvement and in the mathematical model;
    - errors in the observations;

   - errors in the computational procedure used in the solution process;

2. errors in the numerical integration procedure caused by errors in the dynamical model and computer truncation and roundoff errors.

Consequently, the process of observation and estimation must be repeated continually as the motion evolves.

In this work, we focus on the problem of determining the best estimate of Titan's states by the use of observations such as the altimetric data taken by Cassini's RADAR during their encounters. The epochs at which we compute the estimates are set to be few minutes before the first observation is collected for every available flyby where the radar sequence is adopted. As the optimal estimates of the orbital parameters are obtained for each flyby, we will have a new set of Titan's ephemerides that can be used to determine a new more precise moon's orbit.

The accuracy of the obtained ephemerides or orbit, is strictly connected with the precision and accuracy of the models and the measurements errors. In general, rather than being directly observable, the measurements are non-linear functions of the state vector parameters. Also, the differential equations that describe the motion are strongly non linear, and the solution must be obtained by numerical iteration procedure. This leads to the conclusion that multiple solutions can be found, but only one corresponds to the minimizing or correct solution. In the usual operational situation, many observations are made, and the trajectory is selected to give the best agreement with the observations obtained. In general the mechanism for obtaining the best estimate is to linearize the problem by expanding the equations of motions and the observation-state relationship about a reference trajectory. Deviation from the reference trajectory are then determined to yield the "best" agreement with observations. The "best" agreement is commonly based on the least squares criterion.

The goal of the least squares approach is to minimize the *observation residuals* (difference between the true measurements and their computed values). There are essentially two ways to update the state vector: if a new estimate is obtained after each observation we talk about *sequential* or *recursive* estimation. If all the measurements are collected and then processed to obtain an estimate of the state vector at a specified initial epoch (*batch epoch*) we are talking about *batch* estimation.

In general, a sequential estimator (filter) will be more sensitive to the goodness of the individual points than a batch filter. Also, a sequential algorithm will converge faster to the right solution (if it is properly tuned) than a batch algorithm. The last one may require several iterations before converging. The method as it is presented here was first developed and applied for satellite precise orbit determination by Tapley, [21].

3.2 Linearization of the orbit determination process

The general formulation of the orbit determination problem involves significant nonlinear relationships both in dynamics and in measurements. The relations that involves these nonlinear expressions are

$$\begin{aligned} \dot{\mathbf{X}} &= \mathbf{F}(\mathbf{X}, t)\,, & \mathbf{X}(t_k) \equiv \mathbf{X}_k\,, \qquad (3.1)\\ \mathbf{Y}_i &= \mathbf{G}(\mathbf{X}_i, t_i) + \boldsymbol{\epsilon}_i\,, & i = 1, ..., l\,, \qquad (3.2) \end{aligned}$$

where $\mathbf{X}_k$ is the unknown n-dimensional state vector at the time t_k, and $\mathbf{Y}_i$ for $i = 1, ..., l$, is a p-dimensional set of observations that are to be used to obtain a best estimate of the unknown value of $\mathbf{X}_k$, i.e. $\hat{\mathbf{X}}_k$. In general, $p < n$ and $m = p \times l \gg n$.

The formulation represented by equations (3.1) and (3.2) is characterized by:

1. the inability to observe the state directly;
2. nonlinear relations between the observations and the state;

3. fewer observations at any time epoch than there are state vector components ($p < n$);
4. errors in the observations represented by $\boldsymbol{\epsilon}_i$.

The problem of determining the trajectory of a space vehicle in the presence of these effects is referred to as the nonlinear estimation or orbit determination problem. If the state vector and the observation vector can be related in a linear manner, then several powerful techniques from the field of linear estimation theory can be applied to the orbit determination problem.

If a reasonable reference trajectory is available and if $\mathbf{X}$, the true trajectory, and $\mathbf{X}^*$, the reference trajectory, remain sufficiently close throughout the time interval of interest, then the trajectory for the actual motion can be expanded in a Taylor's series about the reference trajectory at each point in time. If this expansion is truncated to eliminate higher order terms, then the deviation in the state from the reference trajectory can be described by a set of linear differential equations with time-dependent coefficients. A linear relation between the observation deviation and the state deviation can be obtained by a similar expansion procedure. Then, the nonlinear orbit determination problem in which the complete state vector is to be estimated can be replaced by a linear orbit determination problem in which the deviation from some reference solution is to be determined.

To conduct this linearization procedure, let the $n \times 1$ state deviation vector, $\mathbf{x}$, and the $p \times 1$ observation deviation vector, $\mathbf{y}$, be defined as follows:

$$\begin{aligned} \mathbf{x}(t) &= \mathbf{X}(t) - \mathbf{X}^*(t)\,, \\ \mathbf{y}(t) &= \mathbf{Y}(t) - \mathbf{Y}^*(t)\,. \end{aligned} \tag{3.3}$$

It follow that

$$\dot{\mathbf{x}}(t) = \dot{\mathbf{X}}(t) - \dot{\mathbf{X}}^*(t)\,. \tag{3.4}$$

Expanding equations (3.1) and (3.2) in a Taylor's series about the reference trajectory leads to

$$\begin{aligned} \dot{\mathbf{X}}(t) &= \mathbf{F}(\mathbf{X},t) = \mathbf{F}(\mathbf{X}^*,t) + \left[\frac{\partial \mathbf{F}(t)}{\partial \mathbf{X}(t)}\right]^* \mathbf{x}(t) + \dots\,, \\ \mathbf{Y}_i(t) &= \mathbf{G}(\mathbf{X}_i,t_i) + \boldsymbol{\epsilon}_i = \mathbf{G}(\mathbf{X}_i^*,t_i) + \left[\frac{\partial \mathbf{G}}{\partial \mathbf{X}}\right]_i^* \mathbf{x}_i + \dots + \boldsymbol{\epsilon}_i\,, \end{aligned} \tag{3.5}$$

where $[\,]^*$ indicates that the partial derivative matrix is evaluated on the reference solution, $\mathbf{X}^*(t)$, which is obtained by integrating Equation (3.1) with the specified initial conditions, $\mathbf{X}^*(t_0)$. If the terms of order higher than the first in equations (3.5) are neglected, under the assumption that the higher order products are small compared to the first order terms, and if the condition $\dot{\mathbf{X}}^* = \mathbf{F}(\mathbf{X}^*,t)$ and $\mathbf{Y}_i^* = \mathbf{G}(\mathbf{X}_i^*,t_i)$ are used, equations (3.5) can be written as

$$\begin{aligned} \dot{\mathbf{x}}(t) &= \mathbf{A}(t)\mathbf{x}(t)\,, \\ \mathbf{y}_i &= \widetilde{\mathbf{H}}_i \mathbf{x}_i + \boldsymbol{\epsilon}_i\,, \qquad i = 1,...,l\,, \end{aligned} \tag{3.6}$$

where

$$\mathbf{A}(t) = \left[\frac{\partial \mathbf{F}(t)}{\partial \mathbf{X}(t)}\right]^*, \qquad \widetilde{\mathbf{H}}_i = \left[\frac{\partial \mathbf{G}}{\partial \mathbf{X}}\right]_i^*. \tag{3.7}$$

Hence, the original nonlinear estimation problem is replaced by the linear estimation problem described by equations (3.6), where

$$\begin{aligned} \mathbf{x}(t) &= \mathbf{X}(t) - \mathbf{X}^*(t)\,, \\ \mathbf{x}_i &= \mathbf{X}(t_i) - \mathbf{X}^*(t_i)\,, \\ \mathbf{y}_i &= \mathbf{Y}_i - \mathbf{G}(\mathbf{X}_i^*,t_i)\,. \end{aligned} \tag{3.8}$$

Notice that if the original system of differential equations $\dot{\mathbf{X}} = F(\mathbf{X},t)$ is linear, the second and higher order partial derivatives of $\mathbf{F}(\mathbf{X},t)$ are zero. The same statements apply to $\mathbf{G}(\mathbf{X}_i,t_i)$. Hence, for a linear system there is no need to deal with a state or observational deviation vector or a reference solution. However, for the orbit determination problem, $\mathbf{F}(\mathbf{X}, t)$ and $\mathbf{G}(\mathbf{X}_i, t_i)$ will always be nonlinear in $\mathbf{X}(t)$, thus requiring that we deal with deviation vectors and a reference trajectory in order to linearize the system.

3.3 The state transition matrix

The first of equations (3.6) represents a system of linear differential equations with time-dependents coefficients. The symbol $[\,]^*$ indicates that the values of $\mathbf{X}$ are derived from a particular solution to the equations $\dot{\mathbf{X}} = \mathbf{F}(\mathbf{X}, t)$ which is generated with the initial conditions $\mathbf{X}(t_0) = \mathbf{X}_0^*$. The general solution for this system, $\dot{\mathbf{x}}(t) = \mathbf{A}(t)\mathbf{x}(t)$, can be expressed as

$$\mathbf{x}(t) = \mathbf{\Phi}(t, t_k)\mathbf{x}_k \,, \tag{3.9}$$

where $\mathbf{x}_k$ is the value of $\mathbf{x}$ at t_k, that is, $\mathbf{x}_k = \mathbf{x}(t_k)$. The matrix $\mathbf{\Phi}(t_i, t_k)$ is called the *state transition matrix*. The state transition matrix has the following useful properties:

$$\begin{aligned} \mathbf{\Phi}(t_i, t_i) &= \mathbf{I} \,, \\ \mathbf{\Phi}(t_i, t_k) &= \mathbf{\Phi}(t_i, t_j)\mathbf{\Phi}(t_j, t_k) \,, \\ \mathbf{\Phi}(t_i, t_k) &= \mathbf{\Phi}^{-1}(t_k, t_i) \,. \end{aligned} \tag{3.10}$$

The differential equation for $\mathbf{\Phi}(t_i, t_k)$ can be obtained by differentiating Equation (3.9) (noting that $\mathbf{x}_k$ is a constant). This yields

$$\dot{\mathbf{x}}(t) = \dot{\mathbf{\Phi}}(t, t_k)\mathbf{x}_k \,. \tag{3.11}$$

Substituting Equation (3.11) into the first of equations (3.6) and using Equation (3.9) yields

$$\dot{\mathbf{\Phi}}(t, t_k)\mathbf{x}_k = \mathbf{A}(t)\mathbf{\Phi}(t, t_k)\mathbf{x}_k \,. \tag{3.12}$$

Since this condition must be satisfied for all $\mathbf{x}_k$, it follows that

$$\dot{\mathbf{\Phi}}(t, t_k) = \mathbf{A}(t)\mathbf{\Phi}(t, t_k) \,, \tag{3.13}$$

with initial conditions

$$\mathbf{\Phi}(t_k, t_k) = \mathbf{I} \,. \tag{3.14}$$

Under certain conditions on $\mathbf{A}(t)$, the state transition matrix may be inverted analytically.

3.3.1 Solution for the state transition matrix

A linear differential equation of the type $\dot{\mathbf{x}}(t) = \mathbf{A}(t)\mathbf{x}(t)$ or $\dot{\mathbf{\Phi}}(t, t_0) = \mathbf{A}(t)\mathbf{\Phi}(t, t_0)$ has an infinite number of solutions in terms of arbitrary constants. However, when initial conditions, $\mathbf{x}(t_0)$ and $\mathbf{\Phi}(t_0, t_0)$, are specified and the elements of $\mathbf{A}(t)$ are continuous functions of time, the solution becomes unique.

The solution for $\mathbf{\Phi}(t, t_0)$ is facilitated by noting that the individual columns of the differential equation for $\dot{\mathbf{\Phi}}(t, t_0)$ are uncoupled and independent. To illustrate this, consider a one-dimensional case where the state vector consists of a single position and velocity coordinate. Equation (3.13) can be written in terms of the individual elements of the state transition matrix as follows:

$$\dot{\mathbf{\Phi}}(t, t_0) = \begin{bmatrix} \dot{\Phi}_{11} & \dot{\Phi}_{12} \\ \dot{\Phi}_{21} & \dot{\Phi}_{22} \end{bmatrix} = \begin{bmatrix} A_{11} & A_{12} \\ A_{21} & A_{22} \end{bmatrix} \begin{bmatrix} \Phi_{11} & \Phi_{12} \\ \Phi_{21} & \Phi_{22} \end{bmatrix} \,, \tag{3.15}$$

subject to the following initial conditions at t_0

$$\begin{bmatrix} \Phi_{11} & \Phi_{12} \\ \Phi_{21} & \Phi_{22} \end{bmatrix} = \begin{bmatrix} \mathbf{I} & \mathbf{0} \\ \mathbf{0} & \mathbf{I} \end{bmatrix} = \mathbf{I} \,. \tag{3.16}$$

Equation (3.15) expands to

$$\begin{bmatrix} \dot{\Phi}_{11} & \dot{\Phi}_{12} \\ \dot{\Phi}_{21} & \dot{\Phi}_{22} \end{bmatrix} = \begin{bmatrix} A_{11}\Phi_{11} + A_{12}\Phi_{21} & A_{11}\Phi_{12} + A_{12}\Phi_{22} \\ A_{21}\Phi_{11} + A_{22}\Phi_{21} & A_{21}\Phi_{12} + A_{22}\Phi_{22} \end{bmatrix} . \tag{3.17}$$

Recall that the A_{ij} are known quantities obtained by evaluating

$$A_{ij}(t) = \left[\frac{\partial \mathbf{F}_i(t)}{\partial \mathbf{X}_j(t)} \right]^* , \tag{3.18}$$

on the reference trajectory. From Equation (3.17) we see that the columns of $\dot{\mathbf{\Phi}}(t, t_0)$ are independent. Hence, we can solve for $\mathbf{\Phi}(t, t_0)$ by integrating independently two 2×1 vector differential equations. For any practical orbit determination application, the solution for $\mathbf{\Phi}(t, t_0)$ will be obtained via numerical integration. Hence, we can supply a vector of derivative values for the differential equation of the nominal state vector and $\dot{\mathbf{\Phi}}(t, t_0)$ to the numerical integration routine. For this one-dimensional case we would supply the integrator with the following vector at each time point:

$$\begin{bmatrix} \dot{\mathbf{r}} \\ \dot{\mathbf{v}} \\ \dot{\Phi}_{11} \\ \dot{\Phi}_{21} \\ \dot{\Phi}_{12} \\ \dot{\Phi}_{22} \end{bmatrix} . \tag{3.19}$$

The first two elements would provide the reference orbit, $\mathbf{X}^*(t)$, and the next nine would yield the elements of $\mathbf{\Phi}(t, t_0)$. The reference orbit is used to evaluate $\mathbf{A}(t)$, which is needed to evaluate $\dot{\mathbf{\Phi}}(t, t_0)$ in Equation (3.17).

3.3.2 Relating the observations to an epoch state

The Equation (3.2) shows that there is an unknown state vector $\mathbf{x}_i$ corresponding to each observation $\mathbf{y}_i$, so it is desirable to use the state transition matrix to express all observations in terms of the state at a single epoch. In this way the number of unknown state vector is reduced from $l \times n$ to n. Using Equation (3.9), the second of Equations (3.6) may be written in terms of the state at t_k as

$$\begin{aligned} \mathbf{y}_1 &= \widetilde{\mathbf{H}}_1 \mathbf{\Phi}(t_1, t_k)\mathbf{x}_k + \boldsymbol{\epsilon}_1 , \\ \mathbf{y}_2 &= \widetilde{\mathbf{H}}_2 \mathbf{\Phi}(t_2, t_k)\mathbf{x}_k + \boldsymbol{\epsilon}_2 , \\ &\vdots \\ \mathbf{y}_1 &= \widetilde{\mathbf{H}}_1 \mathbf{\Phi}(t_1, t_k)\mathbf{x}_k + \boldsymbol{\epsilon}_1 . \end{aligned} \tag{3.20}$$

Equations (3.20) now contain $m = p \times l$ observations and only n unknown components of the state. If $\boldsymbol{\epsilon}_i$ (with $i = 1, ..., l$) is zero, any linearly independent n of equations (3.20) can be used to determine $\mathbf{x}_k$.

If the following definitions are used

$$\mathbf{y} = \begin{bmatrix} \mathbf{y}_1 \\ \vdots \\ \mathbf{y}_1 \end{bmatrix} , \qquad \mathbf{H} = \begin{bmatrix} \widetilde{\mathbf{H}}_1 \mathbf{\Phi}(t_1, t_k) \\ \vdots \\ \widetilde{\mathbf{H}}_1 \mathbf{\Phi}(t_1, t_k) \end{bmatrix} , \qquad \boldsymbol{\epsilon} = \begin{bmatrix} \boldsymbol{\epsilon}_1 \\ \vdots \\ \boldsymbol{\epsilon}_1 \end{bmatrix} , \tag{3.21}$$

and if the subscript on $\mathbf{x}_k$ is dropped for convenience, then equations (3.20) can be expressed as follows:

$$\mathbf{y} = \mathbf{H}\mathbf{x} + \boldsymbol{\varepsilon} , \tag{3.22}$$

where $\mathbf{y}$ is an $m \times 1$ vector, $\mathbf{x}$ is an $n \times 1$ vector, $\boldsymbol{\epsilon}$ is an $m \times 1$ vector, $\mathbf{H}$ is an $m \times n$ mapping matrix, where $m = p \times l$ is the total number of observations. If p or l is sufficiently large, the essential condition $m > n$ is satisfied.

3.4 Least squares solution

The least squares solution selects the estimate of $\mathbf{x}$ as that value that minimizes the sum of the squares of the calculated observation residuals. That is, $\mathbf{x}$ is selected to minimize the following *performance index*:

$$J(\mathbf{x}) = \frac{1}{2}\boldsymbol{\epsilon}^T\boldsymbol{\epsilon}\,. \tag{3.23}$$

The sum of the squares of the calculated observation errors is a logical choice for the performance index. A criterion defined, for example, by the sum of calculated observation errors could be identically zero with very large observation errors having plus and minus signs that cancel each other. Whether the observation error is positive or negative, its square will be positive and the performance index defined by equation (3.23) can vanish only if each of the observation errors is identically zero. If $\boldsymbol{\epsilon}$, as defined by equation (3.22), is substituted into equation (3.23), the following expression is obtained:

$$J(\mathbf{x}) = \frac{1}{2}\boldsymbol{\epsilon}^T\boldsymbol{\epsilon} = \sum_{i=1}^{l}\frac{1}{2}\boldsymbol{\epsilon}_i^T\boldsymbol{\epsilon}_i = \frac{1}{2}(\mathbf{y}-\mathbf{H}\mathbf{x})^T(\mathbf{y}-\mathbf{H}\mathbf{x})\,. \tag{3.24}$$

Note that equation (3.24) is a quadratic function of $\mathbf{x}$, and as a consequence the expression will have a unique minima when

$$\frac{\partial J}{\partial \mathbf{x}} = \mathbf{0}\,, \qquad \text{and} \qquad \delta\mathbf{x}^T\frac{\partial^2 J}{\partial \mathbf{x}^2}\delta\mathbf{x} > \mathbf{0}\,, \tag{3.25}$$

for all $\delta\mathbf{x} \neq 0$. The second condition implies that the symmetric matrix $\frac{\partial^2 J}{\partial \mathbf{x}^2}$ is positive definite.

Carrying out the first operation on equation (3.24) yields

$$\frac{\partial J}{\partial \mathbf{x}} = \mathbf{0} = -(\mathbf{y}-\mathbf{H}\mathbf{x})^T\mathbf{H} = -\mathbf{H}^T(\mathbf{y}-\mathbf{H}\mathbf{x})\,. \tag{3.26}$$

The value of $\mathbf{x}$ that satisfies equation (3.26) will be the best estimate of $\mathbf{x}$, which we will call $\hat{\mathbf{x}}$. Hence,

$$(\mathbf{H}^T\mathbf{H})\hat{\mathbf{x}} = \mathbf{H}^T\mathbf{y}\,. \tag{3.27}$$

Also

$$\frac{\partial^2 J}{\partial \mathbf{x}^2} = \mathbf{H}^T\mathbf{H}\,, \tag{3.28}$$

which will be positive definite if $\mathbf{H}$ is full rank. Equation (3.27) is referred to as the *normal equation*, and $(\mathbf{H}^T\mathbf{H})$ is referred to as the *normal matrix*, that is an $n \times n$ symmetric matrix.

If there are more unknowns than linearly independent equations, in other words $\mathbf{H}$ is of rank $< n$, an unique solution is obtained using the minimum norm criterion to determine $\hat{\mathbf{x}}$. The minimum norm criterion chooses $\mathbf{x}$ to minimize the sum of the squares of the difference between $\mathbf{X}$ and $\mathbf{X}^*$, subject to the constraint that $\boldsymbol{\epsilon} = 0$; that is, $\mathbf{y} = \mathbf{H}\mathbf{x}$. In this case the solution is

$$\hat{\mathbf{x}} = \mathbf{H}^T(\mathbf{H}\mathbf{H}^T)^{-1}\mathbf{y} \tag{3.29}$$

In summary,

$$\begin{aligned} \hat{\mathbf{x}} &= (\mathbf{H}^T\mathbf{H})^{-1}\mathbf{H}^T\mathbf{y}\,, && \text{if } m > n \\ \hat{\mathbf{x}} &= \mathbf{H}^{-1}\mathbf{y}\,, && \text{if } m = n \\ \hat{\mathbf{x}} &= \mathbf{H}^T(\mathbf{H}\mathbf{H}^T)^{-1}\mathbf{y}\,, && \text{if } m < n\,. \end{aligned} \tag{3.30}$$

Shortcomings of the least squares solution

Three major shortcomings of the simple least square solution are:

1. each observation error is weighted equally even though the accuracy of observations may differ;

2. the observation errors may be correlated (not independent), and the simple least squares solution makes no allowance for this;
3. the method does not consider that the errors are samples from a random process and makes no attempt to utilize any statistical information.

3.4.1 Weighted least squares solution

Given a vector sequence of observations $\mathbf{y}_1$, $\mathbf{y}_2$, ..., $\mathbf{y}_l$ related through the state transition matrix to the state at some epoch time, $\mathbf{x}_k$, and an associated weighting matrix, $\mathbf{w}_i$, for each of the observations vectors, one can write

$$\begin{array}{rcll} \mathbf{y}_1 & = & \mathbf{H}_1\mathbf{x}_k + \boldsymbol{\epsilon}_1\,, & \qquad \mathbf{w}_1; \\ \mathbf{y}_2 & = & \mathbf{H}_2\mathbf{x}_k + \boldsymbol{\epsilon}_2\,, & \qquad \mathbf{w}_2; \\ & \vdots & & \\ \mathbf{y}_1 & = & \mathbf{H}_l\mathbf{x}_k + \boldsymbol{\epsilon}_1\,, & \qquad \mathbf{w}_1; \end{array} \tag{3.31}$$

where $\mathbf{H}_i$ is the matrix $\widetilde{\mathbf{H}}_i$ propagated at the time t_i:

$$\mathbf{H}_i = \widetilde{\mathbf{H}}_i \boldsymbol{\Phi}(t_i, t_k)\,. \tag{3.32}$$

In Equations (3.31) the weighting matrices, $\mathbf{w}_i$, are assumed to be diagonal with their elements normalized to a range between zero and one. Observations weighted with a one would be given the highest possible weight and those weighted with zero would be neglected. The following definitions can be used

$$\mathbf{y} = \begin{bmatrix} \mathbf{y}_1 \\ \mathbf{y}_2 \\ \vdots \\ \mathbf{y}_1 \end{bmatrix}, \quad \mathbf{H} = \begin{bmatrix} \mathbf{H}_1 \\ \mathbf{H}_2 \\ \vdots \\ \mathbf{H}_1 \end{bmatrix}, \quad \boldsymbol{\epsilon} = \begin{bmatrix} \boldsymbol{\epsilon}_1 \\ \boldsymbol{\epsilon}_2 \\ \vdots \\ \boldsymbol{\epsilon}_1 \end{bmatrix}, \quad \mathbf{W} = \begin{bmatrix} \mathbf{w}_1 & 0 & ... & 0 \\ 0 & \mathbf{w}_2 & ... & 0 \\ \vdots & \vdots & ... & \vdots \\ 0 & 0 & ... & \mathbf{w}_l \end{bmatrix}. \tag{3.33}$$

Each observation $\mathbf{y}_i$ is assumed to be a p-vector and $\mathbf{x}_k$ is a n-vector. Equations (3.31) now can be expressed as

$$\mathbf{y} = \mathbf{H}\mathbf{x}_k + \boldsymbol{\epsilon}\,, \qquad \mathbf{W}\,. \tag{3.34}$$

The weighted least square problem can then be posed as follows: given the linear observation state relationship expressed by (3.34), find the estimate of $\mathbf{x}_k$ to minimize the weighted sum of the squares of the calculated observation errors.

The performance index is

$$J(\mathbf{x}_k) = \frac{1}{2}\boldsymbol{\epsilon}^T\mathbf{W}\boldsymbol{\epsilon} = \sum_{i=1}^{l} \frac{1}{2}\boldsymbol{\epsilon}_i^T \mathbf{w}_\mathbf{i} \boldsymbol{\epsilon}_i\,. \tag{3.35}$$

Using equation (3.34), $J(\mathbf{x}_k)$ can be expressed as

$$J(\mathbf{x}_k) = \frac{1}{2}(\mathbf{y} - \mathbf{H}\mathbf{x}_k)^T\mathbf{W}(\mathbf{y} - \mathbf{H}\mathbf{x}_k)\,. \tag{3.36}$$

A necessary condition for a minimum of $J(\mathbf{x}_k)$ is that its first derivative with respect to $\mathbf{x}_k$ vanishes

$$\frac{\partial J}{\partial \mathbf{x}_k} = \mathbf{0} = -(\mathbf{y} - \mathbf{H}\mathbf{x}_k)^T\mathbf{W}\mathbf{H} = -\mathbf{H}^T\mathbf{W}(\mathbf{y} - \mathbf{H}\mathbf{x}_k)\,. \tag{3.37}$$

This expression can be rearranged to obtain the normal equations in the least squares formulation as

$$(\mathbf{H}^T\mathbf{W}\mathbf{H})\mathbf{x}_k = \mathbf{H}^T\mathbf{W}\mathbf{y}\,. \tag{3.38}$$

If the normal matrix $\mathbf{H}^T\mathbf{W}\mathbf{H}$ is positive definite, it will have an inverse and the solution to (3.38) is

$$\hat{\mathbf{x}}_k = (\mathbf{H}^T\mathbf{W}\mathbf{H})^{-1}\mathbf{H}^T\mathbf{W}\mathbf{y}\,. \tag{3.39}$$

The value of $\hat{\mathbf{x}}_k$ given by equation (3.39) is the weighted least squares estimate and is the estimate that minimizes the sum of squares of the weighted observation errors. Note that equation (3.39) can be expressed as

$$\hat{\mathbf{x}}_k = \mathbf{P}_k\mathbf{H}^T\mathbf{W}\mathbf{y}\,, \tag{3.40}$$

where

$$\mathbf{P}_k = (\mathbf{H}^T\mathbf{W}\mathbf{H})^{-1}\,. \tag{3.41}$$

The $n \times n$ matrix $\mathbf{P}_k$ is symmetric. Furthermore, if it exists, it must be positive definite, since it is computed as the inverse of the positive definite matrix, $\mathbf{H}^T\mathbf{W}\mathbf{H}$. The parameter observability is related to the rank of this matrix. If all parameters in $\mathbf{x}_k$ are observable (i.e., can be uniquely determined with the observation set $\mathbf{y}$), then $\mathbf{P}_k$ will be full rank and $\mathbf{P}_k$ will have an inverse. The number of independent observations must be greater than or equal to the number of parameters being estimated if $\mathbf{P}_k$ is to be invertible. Furthermore, $\mathbf{P}_k$ is related to the accuracy of the estimate, $\hat{\mathbf{x}}_k$. In general, the larger the magnitude of the elements of the matrix, $\mathbf{P}_k$, the less accurate the estimate.

If an a priori value, $\bar{\mathbf{x}}_k$, is available for $\mathbf{x}_k$ and an associated weighting matrix, $\bar{\mathbf{W}}_k$, is given, the weighted least square estimate for $\mathbf{x}_k$ can be obtained by choosing for $\hat{\mathbf{x}}_k$ the value of $\mathbf{x}_k$, which minimizes the performance index

$$J(\mathbf{x}_k) = \frac{1}{2}(\mathbf{y} - \mathbf{H}\mathbf{x}_k)^T\mathbf{W}(\mathbf{y} - \mathbf{H}\mathbf{x}_k) + \frac{1}{2}(\bar{\mathbf{x}}_k - \mathbf{x}_k)^T\bar{\mathbf{W}}_k(\bar{\mathbf{x}}_k - \mathbf{x}_k)\,. \tag{3.42}$$

This results in

$$\hat{\mathbf{x}}_k = (\mathbf{H}^T\mathbf{W}\mathbf{H} + \bar{\mathbf{W}}_k)^{-1}\left(\mathbf{H}^T\mathbf{W}\mathbf{y} + \bar{\mathbf{W}}_k\bar{\mathbf{x}}_k\right)\,, \tag{3.43}$$

where $\bar{\mathbf{x}}_k$ represents an a priori estimate of $\mathbf{x}_k$ and $\bar{\mathbf{W}}_k$ represents a weighting matrix for the a priori estimate of $\mathbf{x}_k$.

3.4.2 The minimum variance estimate

The least squares and weighted least squares methods do not include any information on the statistical characteristics of the measurement errors or the a priori errors in the values of the parameters to be estimated. The minimum variance approach is one method for removing this limitation. The minimum variance criterion is used widely in developing solutions to estimation problems because of the simplicity in its use. It has the advantage that the complete statistical description of the random errors in the problem is not required. Rather, only the first and second moments of the probability density function of the observation errors are required. This information is expressed in the mean and covariance matrix associated with the random error.

If it is assumed that the observation error $\boldsymbol{\epsilon}_i$ is random with zero mean and specified covariance, the state estimation problem can be formulated as follows.

Given the system of state-propagation equations and observation state equations

$$\begin{aligned} \mathbf{x}_i &= \boldsymbol{\Phi}(t_i, t_k)\mathbf{x}_k\,, & (3.44)\\ \mathbf{y}_i &= \widetilde{\mathbf{H}}_i\mathbf{x}_i + \boldsymbol{\epsilon}_i\,, \qquad i = 1, ..., l\,, & (3.45) \end{aligned}$$

find the linear, unbiased, minimum variance estimate, $\hat{\mathbf{x}}_k$, of the state $\mathbf{x}_k$.

Using the state transition matrix and the definitions of equations (3.31), it is possible to reduce equation (3.44) to the following form

$$\mathbf{y} = \mathbf{H}\mathbf{x}_k + \boldsymbol{\epsilon}\,, \tag{3.46}$$

where

$$E[\varepsilon] = \begin{bmatrix} E[\boldsymbol{\epsilon}_1] \\ E[\boldsymbol{\epsilon}_2] \\ \vdots \\ E[\boldsymbol{\epsilon}_1] \end{bmatrix} = \begin{bmatrix} \mathbf{0} \\ \mathbf{0} \\ \vdots \\ \mathbf{0} \end{bmatrix}, \qquad E[\boldsymbol{\epsilon}\boldsymbol{\epsilon}^T] = \begin{bmatrix} \mathbf{R}_{11} & \mathbf{R}_{12} & ... & \mathbf{R}_{1l} \\ \mathbf{R}_{12}^T & \mathbf{R}_{22} & ... & \mathbf{R}_{2l} \\ \vdots & ... & ... & \vdots \\ \mathbf{R}_{1l}^T & ... & ... & \mathbf{R}_{ll} \end{bmatrix} = \mathbf{R}\,.$$

Generally, $\mathbf{R}_{11} = \mathbf{R}_{22} = ... = \mathbf{R}_{ll}$ and $\mathbf{R}_{ij} = \mathbf{0}$ $(i \neq j)$, but this is not a necessary restriction. $\mathbf{R}_{ij} \neq \mathbf{0}$ $(i \neq j)$ corresponds to the more general case of time-correlated observation errors.

From the problem statement, the estimate is to be the best linear, unbiased, minimum variance estimate. The consequences of each of these requirements are addressed in the following steps.

1. *Linear*: the requirement of a linear estimate implies that the estimate is to be made up of a linear combination of the observations:
$$\mathbf{x}_k = \mathbf{M}\mathbf{y}\,. \tag{3.47}$$
The $n \times m$ matrix $\mathbf{M}$ is unspecified and is to be selected to obtain the best estimate.

2. *Unbiased*: if the estimate is unbiased, then by definition
$$E[\hat{\mathbf{x}}] = \mathbf{x}\,. \tag{3.48}$$
Substituting equations (3.47) and (3.44) into equation (3.48) leads to the following requirement
$$E[\hat{\mathbf{x}}_k] = E[\mathbf{M}\mathbf{y}] = E[\mathbf{M}\mathbf{H}\mathbf{x}_k + \mathbf{M}\boldsymbol{\epsilon}] = \mathbf{x}_k\,. \tag{3.49}$$
But, since $E[\boldsymbol{\epsilon}] = \mathbf{0}$, this reduces to
$$\mathbf{M}\mathbf{H}\mathbf{x}_k = \mathbf{x}_k\,, \tag{3.50}$$
from which the following constraint on $\mathbf{M}$ is obtained
$$\mathbf{M}\mathbf{H} = \mathbf{I}\,. \tag{3.51}$$
That is, if the estimate is to be unbiased, the linear mapping matrix $\mathbf{M}$ must satisfy equation (3.51). This condition requires the rows of $\mathbf{M}$ to be orthogonal to the columns of $\mathbf{H}$.

3. *Minimum Variance*: if the estimate is unbiased, then the estimation error covariance matrix can be expressed as
$$\mathbf{P}_k = E\{[(\hat{\mathbf{x}}_k - \mathbf{x}_k) - E(\hat{\mathbf{x}}_k - \mathbf{x}_k)][(\hat{\mathbf{x}}_k - \mathbf{x}_k) - E(\hat{\mathbf{x}}_k - \mathbf{x}_k)]^T\} = E[(\hat{\mathbf{x}}_k - \mathbf{x}_k)(\hat{\mathbf{x}}_k - \mathbf{x}_k)^T]\,. \tag{3.52}$$

Minimizing the last expression satisfying the two constraints 1) and 2) at the same time we obtain the following formulas ([21]):

$$\mathbf{P}_k = \left(\mathbf{H}^T\mathbf{R}^{-1}\mathbf{H}\right)^{-1}\,, \tag{3.53}$$

$$\hat{\mathbf{x}}_k = \left(\mathbf{H}^T\mathbf{R}^{-1}\mathbf{H}\right)^{-1}\mathbf{H}^T\mathbf{R}^{-1}\mathbf{y}\,. \tag{3.54}$$

Note that computation of the estimate, $\hat{\mathbf{x}}_k$, requires inverting the $n \times n$ normal matrix $\mathbf{H}^T\mathbf{R}^{-1}\mathbf{H}$. For a large dimension system the computation of this inverse may be difficult. For this reason, alternative techniques have been employed (Cholesky decomposition, Householder transformations and Given's rotations, see [21]). The solution given by equations (3.54) will agree with the weighted least square solution if the weighting matrix, $\mathbf{W}$, used in the least square approach is equal to the inverse of the observation noise covariance matrix; that is if $\mathbf{W} = \mathbf{R}^{-1}$.

3.4.3 Propagation of the estimate and covariance matrix

If an estimate at a time t_j is obtained by using equation (3.54), the estimate may be mapped to any later time by using the state transition matrix $\mathbf{\Phi}$

$$\bar{\mathbf{x}}_k = \mathbf{\Phi}\left(t_k, t_j\right) \hat{\mathbf{x}}_j \,, \tag{3.55}$$

where $\bar{\mathbf{x}}_k$ is the best estimate of $\mathbf{x}_k$ at time $t_k > t_j$ based on the observations collected up to t_j. The expression for propagating the covariance matrix $\bar{\mathbf{P}}_k$ is the following:

$$\bar{\mathbf{P}}_k = \mathbf{\Phi}\left(t_k, t_j\right) \mathbf{P}_j \mathbf{\Phi}^T \left(t_k, t_j\right) \,, \tag{3.56}$$

where $\mathbf{P}_j = E[(\hat{\mathbf{x}}_j - \mathbf{x}_j)(\hat{\mathbf{x}}_j - \mathbf{x}_j)^T | \mathbf{y}_1, ..., \mathbf{y}_j]$ is the covariance matrix at time t_j provided the observations up to t_j.

3.4.4 Minimum variance estimate with a priori information

If an estimate and the associated covariance matrix are obtained at a time t_j, and an additional observation or observation sequence is obtained at time t_k, the estimate and the observation can be combined in a straightforward manner to obtain the new estimate $\hat{\mathbf{x}}_k$. The estimate, $\hat{\mathbf{x}}_j$, and the associated covariance, $\mathbf{P}_j$, are propagated forward to t_k. The problem can be stated as follows: given the propagated estimates of the state vector $\bar{\mathbf{x}}_k$, the covariance matrix $\bar{\mathbf{P}}_k$ and a new observation $\mathbf{y}_k$ at time t_k

$$\mathbf{y}_k = \widetilde{\mathbf{H}}_k \mathbf{x}_k + \boldsymbol{\epsilon}_k, \tag{3.57}$$

where $E\left[\boldsymbol{\epsilon}_k\right] = \mathbf{0}$, $E[\boldsymbol{\epsilon}_k \boldsymbol{\epsilon}_j^T] = \mathbf{R}_k \delta_{kj}$, and $E[(\mathbf{x}_j - \hat{\mathbf{x}}_j)\boldsymbol{\epsilon}_k^T] = \mathbf{0}$, find the linear, minimum variance, unbiased estimate of $\mathbf{x}_k$.

The solution to this problem can be obtained by reducing it to the previous solved problem interpreting $\bar{\mathbf{x}}_k$ as an observation. Hence it can be found ([21]) that the new optimal estimate is:

$$\hat{\mathbf{x}}_k = (\widetilde{\mathbf{H}}_k^T \mathbf{R}_k^{-1} \widetilde{\mathbf{H}}_k + \overline{\mathbf{P}}_k^{-1})^{-1} (\widetilde{\mathbf{H}}_k^T \mathbf{R}_k^{-1} \mathbf{y}_k + \overline{\mathbf{P}}_k^{-1} \bar{\mathbf{x}}_k) \,, \tag{3.58}$$

and the associated covariance is:

$$\mathbf{P}_k = E[(\hat{\mathbf{x}}_k - E[\hat{\mathbf{x}}_k])(\hat{\mathbf{x}}_k - E[\hat{\mathbf{x}}_k])^T] = (\widetilde{\mathbf{H}}_k^T \mathbf{R}_k^{-1} \widetilde{\mathbf{H}}_k + \overline{\mathbf{P}}_k^{-1})^{-1}. \tag{3.59}$$

These remarks follow Equation (3.58):

1. the array $\mathbf{y}_k$ can be a single observation or it may include a batch of observations mapped to t_k;
2. the a-priori estimate, $\bar{\mathbf{x}}_k$, may represent the estimate based on a priori initial conditions or the estimate based upon a set of previously reduced observations;
3. the $n \times n$ normal matrix of (3.58) must be inverted and if the dimension n is large, this inversion can lead to computational problems. Alternate solution techniques are widely discussed by [21].

Two type of algorithms implement Equations (3.58) and (3.59): the **batch processor** or **batch filter** and the the **sequential processor** or **sequential filter**. The first one accumulates the entire set of data prior to solving for $\hat{\mathbf{x}}_k$; the data are in this way precessed in a single batch. The sequential filter maps the state estimate and the covariance matrix to the time of the next observation, where they would become a-priori information for the next observation. Then they are combined with the observation at that time to compute the estimate for $\hat{\mathbf{x}}_k$. A detailed discussion about these algorithms can be found in Tapley, [21].

3.5 Computational algorithm for the batch processor

Assume that we wish to estimate the state deviation vector $\mathbf{x}_0$ at a reference time, t_0. Given a set of initial conditions $\mathbf{X}^*(t_0)$, an a priori estimate $\bar{\mathbf{x}}_0$ and the associated error covariance matrix, $\bar{\mathbf{P}}_0$, the computational algorithm for the batch processor generally uses the normal equation form for $\hat{\mathbf{x}}_0$. Writing equation (3.43) in normal equations form for a batch of observations and recognizing that $\mathbf{W} = \mathbf{R}^{-1}$ and $\bar{\mathbf{W}} = \bar{\mathbf{P}}_0^{-1}$ yields

$$(\mathbf{H}^T\mathbf{R}^{-1}\mathbf{H} + \bar{\mathbf{P}}_0^{-1})\hat{\mathbf{x}}_0 = \mathbf{H}^T\mathbf{R}^{-1}\mathbf{y} + \bar{\mathbf{P}}_0^{-1}\bar{\mathbf{x}}_0 \,. \tag{3.60}$$

Here t_0 is an arbitrary epoch and all quantities in equation (3.60) are assumed to have been mapped to this epoch using the appropriate state transition matrices as illustrated in equations (3.31) and (3.33).

If $\mathbf{R}$ is a block diagonal matrix, that is the observations are uncorrelated in time although correlations between the observations at any given time may exist, these matrices simply may be accumulated as follows:

$$\mathbf{H}^T\mathbf{R}^{-1}\mathbf{H} = \sum_{i=1}^{l}[\widetilde{\mathbf{H}}_i\mathbf{\Phi}(t_i,t_0)]^T\mathbf{R}_i^{-1}\widetilde{\mathbf{H}}_i\mathbf{\Phi}(t_i,t_0)\,, \tag{3.61}$$

$$\mathbf{H}^T\mathbf{R}^{-1}\mathbf{y} = \sum_{i=1}^{l}[\widetilde{\mathbf{H}}_i\mathbf{\Phi}(t_i,t_0)]^T\mathbf{R}_i^{-1}\mathbf{y}_i \,. \tag{3.62}$$

In general $\mathbf{X}^*(t_0)$ would be chosen so that $\bar{\mathbf{x}}_0 = \mathbf{0}$, and $\bar{\mathbf{P}}_0$ would reflect the relative accuracy of the elements of the initial conditions vector $\mathbf{X}^*(t_0)$. In theory $\bar{\mathbf{x}}_0$ and $\bar{\mathbf{P}}_0$ represent information and should be treated as data that are merged with the observation data, as indicated by equation (3.60). Consequently, the value of $\mathbf{X}_0^*+\bar{\mathbf{x}}_0$ should be held constant for the beginning of each iteration. Since the initial condition vector $\mathbf{X}_0^*$ is augmented by the value of $\hat{\mathbf{x}}_0$ after each iteration, that is, $(\mathbf{X}_0^*)_n = (\mathbf{X}_0^*)_{n-1} + (\hat{\mathbf{x}}_0)_{n-1}$, holding $\mathbf{X}_0^* + \bar{\mathbf{x}}_0$ constant results in the following expression for $(\bar{\mathbf{x}}_0)_n$

$$(\bar{\mathbf{x}}_0)_n = (\bar{\mathbf{x}}_0)_{n-1} - (\hat{\mathbf{x}}_0)_{n-1} \,. \tag{3.63}$$

Recall that the state transition matrix is obtained by integrating

$$\dot{\mathbf{\Phi}}(t,t_k) = \mathbf{A}(t)\mathbf{\Phi}(t,t_k)\,, \tag{3.64}$$

subject to the initial conditions $\mathbf{\Phi}(t_k,t_k) = \mathbf{I}$ along with the nonlinear equations, $\dot{\mathbf{X}}^* = \mathbf{F}(\mathbf{X}^*,t)$, which define the nominal trajectory, $\dot{\mathbf{X}}^*(t)$. The matrix $\mathbf{A}(t)$ is evaluated on the reference trajectory,

$$\mathbf{A}(t) = \frac{\partial \mathbf{F}(\mathbf{X}^*,t)}{\partial \mathbf{X}}\,, \tag{3.65}$$

where $\mathbf{F}(\mathbf{X}^*,t)$ is the time derivative of the state vector in the differential equations governing the time evolution of the system. The observation-state mapping matrix is given by

$$\widetilde{\mathbf{H}}_i = \frac{\partial \mathbf{G}(\mathbf{X}_i^*,t_i)}{\partial \mathbf{X}}\,, \tag{3.66}$$

where $\mathbf{G}(\mathbf{X}_i^*,t_i)$ are the observation-state relationships evaluated on the nominal or reference trajectory.

Notice that the solution for $\hat{\mathbf{x}}_0$ involved inversion of the information matrix, $\mathbf{\Lambda}_0$, where

$$\mathbf{\Lambda}_0 = \mathbf{H}^T\mathbf{R}^{-1}\mathbf{H} + \bar{\mathbf{P}}_0^{-1}\,. \tag{3.67}$$

Generally the normal equations would not be solved by a direct inversion of $\mathbf{\Lambda}_0$ but rather would be solved by an indirect but more accurate technique, such as the Cholesky decomposition. The sequence of operations required to implement the batch estimation process is outlined in Figure 3.1, where we assume that there are no observations at t_0. If observations exist at t_0, set $\mathbf{\Lambda} = \bar{\mathbf{P}}_0^{-1} + \mathbf{H}_0^T\mathbf{R}_0^{-1}\mathbf{H}_0$ and $\mathbf{N} = \mathbf{H}_0^T\mathbf{R}_0^{-1}\mathbf{y}_0$ in the initialization. As previously stated, the entire sequence of computations are repeated until the estimation process has converged. If there are observations at t_0, the state transition matrix for processing these observations is the identity matrix.

This procedure yields a minimum value of the performance index

$$J(\mathbf{x}) = (\hat{\mathbf{x}}_0 - \bar{\mathbf{x}}_0)^T \bar{\mathbf{P}}_0^{-1} + \sum_{i=1}^{l} \hat{\boldsymbol{\epsilon}}_i^T \mathbf{R}_i^{-1} \hat{\boldsymbol{\epsilon}}_i \,, \tag{3.68}$$

where

$$\hat{\varepsilon}_i = \mathbf{y}_i - \mathbf{H}_i \hat{\mathbf{x}}_0 \,, \tag{3.69}$$

and $\hat{\boldsymbol{\epsilon}}_i$ is the best estimate of the observation error.

In practice, $\bar{\mathbf{P}}_0$ is generally not a realistic representation of the accuracy of $\bar{\mathbf{x}}_0$ and it is used only to better condition to estimation error covariance matrix, $\mathbf{P}$. In this case, $\bar{\mathbf{x}}_0$ usually is set to zero for each iteration and $\bar{\mathbf{P}}_0$ is chosen to be a diagonal matrix with large diagonal values. Hence, the first term in equation (3.68) will be very small and the tracking data residuals will determine the value of $J(\mathbf{x})$. The rms (root mean square) of the observation residuals generally is computed and may be used as a measure of convergence; when the rms no larger changes the solution is assumed to be converged. The rms is computed from

$$rms = \left\{ \frac{\sum_{i=1}^{l} \hat{\boldsymbol{\epsilon}}_i^T \mathbf{R}_i^{-1} \hat{\boldsymbol{\epsilon}}_i}{m} \right\}^{\frac{1}{2}} \,, \tag{3.70}$$

where $\hat{\boldsymbol{\epsilon}}_i$ is a p-vector and $m = l \times p$. Hence, m is the total number of observations. The equation (3.70) is referred to as the weighted rms. If the rms is computed without including the weighting matrix, $\mathbf{R}_i^{-1}$, it may be referred to as the unweighted rms or just the rms.

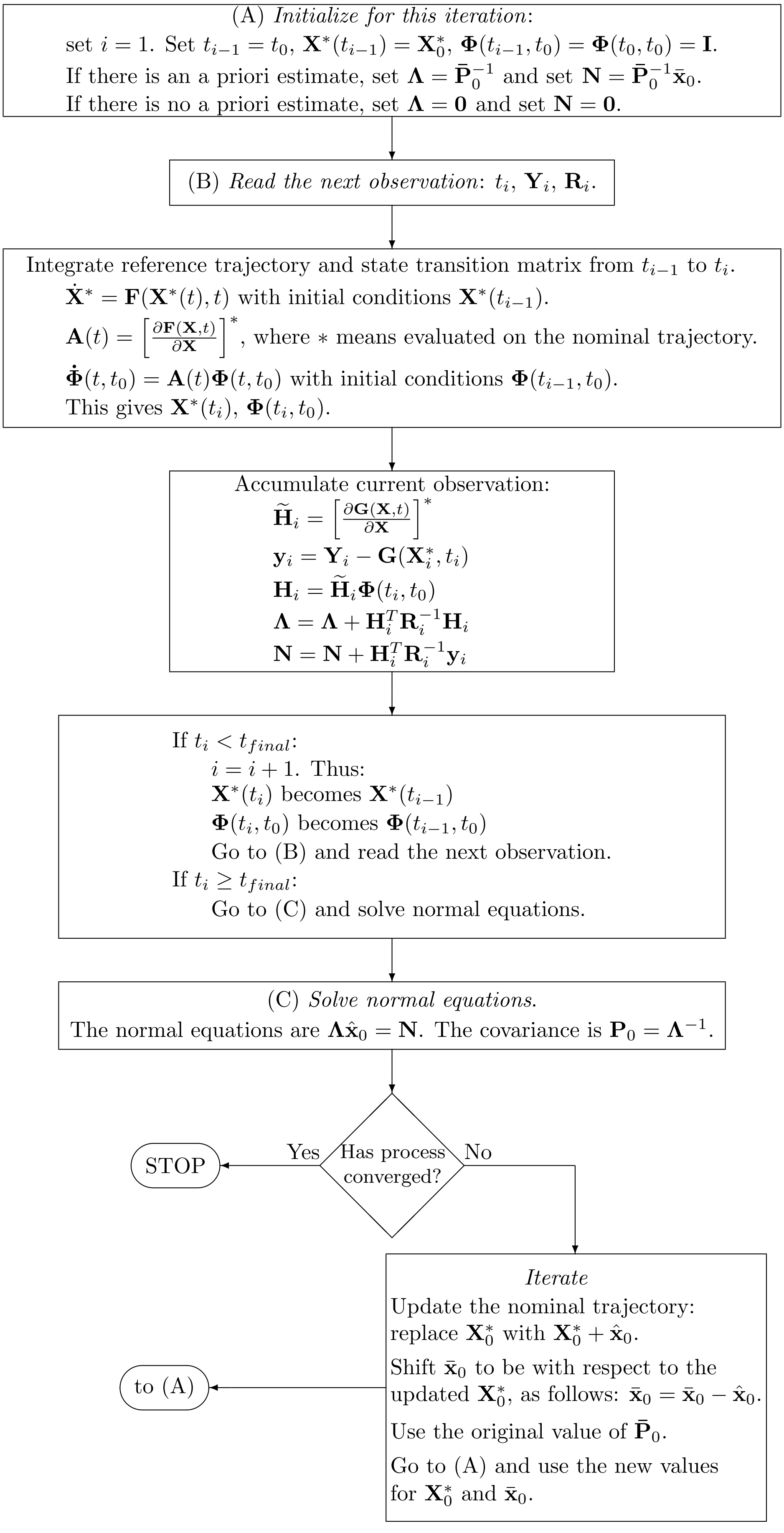

Figure 3.1: Batch processing algorithm flow chart.

Chapter 4

Altimetric Observation Model

4.1 Introduction

Titan's orbit determination is made by means of the altimetric data acquired by the Cassini RADAR instrument. Each set of data consists of range-to-target distances computed for each single burst time and they are collected in the flybys where the altimeter radar mode is operational.

The state estimation procedure implemented adopts a least square batch filter: all the measurements are collected and then processed in order to obtain the estimate of Titan's state vector at epoch (*batch epoch*). As explained in Chapter 3, the least squares method involves the computation of the residuals of the measurements. Residuals are the differences between the actual measurements and their computed values from a geometric model of the observation.

In this chapter we describe the altimetric observation model adopted for this investigation and the geometric relations between Cassini and Titan's state vectors. Moreover, we give the detailed procedure that yields the range-to-target computed values. The procedure, which needs Cassini's attitude and RADAR's beam 3 field of view direction vector, finds the beam intersection point with the surface and then computes the range value at each observation time.

The altimetric formulation of the observation equation is given along with the geometric partial derivatives of the model with respect to Titan's state vector at epoch.

4.2 Background on the altimetric orbit determination process

As discussed in Chapter 3, the orbit determination process gives the possibility of improving a preliminary spacecraft orbit obtained from radiometric data by the use of altimetric data type computed as ranges to the surface. The altimeter measurements made during the Cassini flybys of Titan can used according to two different schemes. In the first, and apparently the more obvious one, the orbit of Cassini can be estimated with respect to a Titan-centered reference frame. In the second scheme, the same measurements can be used to determine the orbit of Titan with respect to the reference frame implicitly defined by the orbit of the Cassini spacecraft. Since the orbit of Cassini is known with an accuracy much higher than the accuracy with which the orbit of Titan is known, we adopt the second processing scheme in an attempt to improve, at least partially, the orbit of Titan. This is possible because of the relatively high accuracy of the altimeter observations, which far surpasses the orbit accuracy of Titan. In the end, the estimated orbit of Titan will be, so to speak, "attached" to the orbit of Cassini, and in turn to the Saturnian system, with respect to which Cassini's orbit is known.

The process of orbit determination implemented in the case of an altimetric data type run, is based on several input files. These files are needed in order to compute the measurement residuals and they are the following:

- the altimetric data files received from CO.RI.S.T.A. (Consortium for Research on Advanced Remote Sensing Systems). These data consists of *.csv* extension files containing the fields of interest used in the orbit determination process. The data fields are described in detail in Section 5.2.
- Cassini's orbit arcs and attitude files at the flybys dates. The spacecraft states and attitude values are read in during the orbit determination process to compute the relative state vectors of Titan with respect Cassini spacecraft at the burst time at which the measurements and their computed values are referred to. The files in SPICE-Kernels form are provided by the Data Search Service (DSS) of PDS.
- SPICE kernels used to calculate the Cassini instruments and RADAR's beams alignment and boresight direction (provided by DSS).

The reference frames involved in the process are:

1. The J2000 reference frame centered on the barycenter of the Saturnian system, $\{\mathbf{X_S}, \mathbf{Y_S}, \mathbf{Z_S}\}$, where Cassini's state is given and Titan's state is estimated;
2. The Cassini fixed reference frame, $\{\mathbf{X_{sc}}, \mathbf{Y_{sc}}, \mathbf{Z_{sc}}\}$, needed to know the direction of the beam 3 in order to compute the slant range as altimetric observation.

The software developed in this work implements the problem of orbit determination solved for Titan's state at epoch t_0 keeping fixed the trajectory of Cassini spacecraft. The measurements used by the process are the altimetric data collected during the flyby and the epoch at which the state of Titan is estimated is set to be a few minutes before the first observation happens. The estimation process is repeated for each of the flybys the sets of data received are referred to.

4.3 The altimetric data used in the orbit determination process

When Titan is close enough for useful altimetry, the radar switches to altimeter mode, as noted in Section 1.3. The raw altimeter data product is an echo profile consisting of intensity versus propagation time delay referenced to the spacecraft clock. The delay corresponds, via a factor of two and the speed of light, to the distance to the target. During the observation interval, the spacecraft attitude is maintained near nadir-pointing by Cassini's attitude control system and the altimetric measurement $\mathbf{h}$ becomes a measure of the slant range. Referring to Figure 4.1a, we define $\boldsymbol{\rho}_\mathrm{T}$ as the position on Titan's surface of the foot of the altimeter beam, $\mathbf{r}$ as the position vector of Titan with respect to the Cassini spacecraft, S being the intersection point of the boresight ray of the Cassini RADAR instrument with the surface. The incidence angle, i, is the angle between the look direction of the incident radar beam and the normal to the intercepting surface halfway between transmission and receipt of the active mode signal. If we consider Titan as a sphere, the normal to the surface coincides with the line that joins Cassini to Titan's center of mass. The off nadir angle, α, is the angle formed by the slant range direction and $\mathbf{r}$. The values of the ranges worked out by CO.RI.S.T.A. are the best estimates of the distances between the target and Cassini spacecraft. As explained in [3], determining the surface height relative to the Titan sphere of radius 2575.0 km, also depends upon an independent measurement of the position of the surface relative to the altimeter. The Cassini-Titan distance is found using the ephemerides determined by the project navigation team and it is reconstructed after a flyby to an accuracy better then 100 m.

4.4 Cassini fixed reference frame and field of view direction

As documented in Frame Definitions (FK-kernels) and Instrument (IK-kernels) SPICE kernels, the spacecraft coordinate system $\{\mathbf{X_{sc}}, \mathbf{Y_{sc}}, \mathbf{Z_{sc}}\}$ is a body fixed coordinate system to which the primary

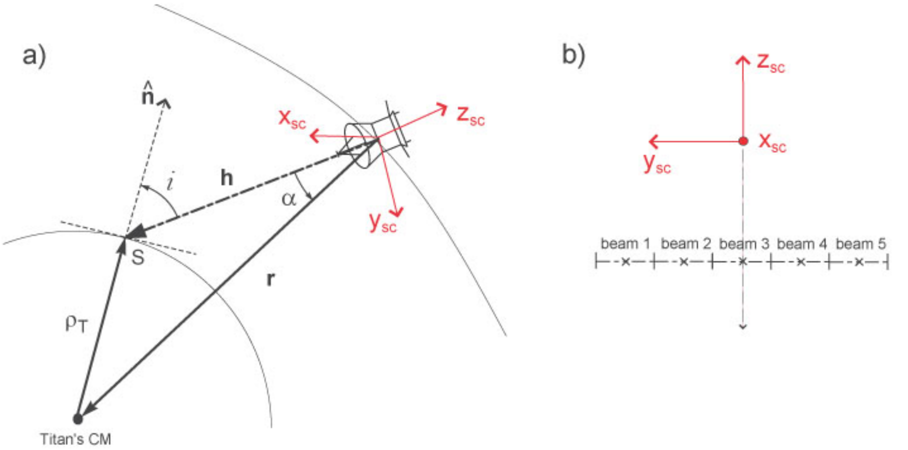

Figure 4.1: a) Angles of interest during the altimetric observations time interval. b) Configuration of the radar beams: beam 3 is directed nominally along the $\mathbf{Z_{sc}}$ axis of the spacecraft frame.

geometrical and mass properties are strictly related. The high-gain antenna points nominally along the spacecraft $\mathbf{Z_{sc}}$ axis (Figure 4.1b), and each single beam has a fixed orientation respect to $\{\mathbf{X_{sc}}, \mathbf{Y_{sc}}, \mathbf{Z_{sc}}\}$ reference frame. Consequently, given Cassini's attitude matrix at the observation time, the boresight direction at the same time is perfectly known without requiring the use of the incidence angle (or off-nadir angle) defined in the previous section. Moreover, the altimetric data are the results of signal processing algorithms which consider the influence of several additional parameters on radar pulse and the effect of the incident angle is included.

From the kernels files, attitude matrices can be extracted by the use of specific SPICE subroutines. The attitude matrices give the components values of direction vector representing Cassini coordinate system's axes in the J2000 reference frame. In order to know the coordinates of the surface intersection point S at the observation time t_i (4.1a)), the matrix representing spacecraft's orientation is needed at the same time t_i. This procedure is performed by SPICE subroutine `CKGP` described in Appendix C. One of the outputs of the subroutine is the rotation matrix, $\mathcal{R}_{sc}$, that transforms the components of a vector expressed in the Saturnian system's barycenter reference frame to the components expressed in the frame tied to the spacecraft at a given Cassini clock time t_i^{cl}. As we solved the orbit determination problem in the barycentric reference frame, we need the inverse coordinates transformation given by the transpose of the matrix $\mathcal{R}_{sc}$. The coordinates transformation is

$$\begin{pmatrix} \mathbf{X_S} \\ \mathbf{Y_S} \\ \mathbf{Z_S} \end{pmatrix} = \mathcal{R}_{sc}^{\mathrm{T}} \begin{pmatrix} \mathbf{X_{sc}} \\ \mathbf{Y_{sc}} \\ \mathbf{Z_{sc}} \end{pmatrix}. \tag{4.1}$$

Then, as specified by the IK/FK kernels and referring to Figure 4.1b, the coordinates transformation needed to know the orientation of the beam 3 field of view in the barycentric reference frame, $\mathbf{FOV}|_{J2000} = (a, b, c)$, is

$$\mathbf{FOV}|_{J2000} = \begin{pmatrix} a \\ b \\ c \end{pmatrix} = \mathcal{R}_{sc}^{\mathrm{T}} \begin{pmatrix} 0 \\ 0 \\ -1 \end{pmatrix}. \tag{4.2}$$

The geometrical procedure used to find the surface intersection point is described below.

Given the Cassini position coordinates (x_C, y_C, z_C) and the direction vector of the beam 3 field of view, the parametric equation of the line defined by these two points is

$$\begin{cases} x = x_C + at \\ y = y_C + bt \\ z = z_C + ct \end{cases} \tag{4.3}$$

and the equation of the sphere representing Titan is given by

$$(x - x_T)^2 + (y - y_T)^2 + (z - z_T)^2 = \rho_T^2. \tag{4.4}$$

Substituting (4.3) in (4.4) we have

$$(x_C + at - x_T)^2 + (y_C + bt - y_T)^2 + (z_C + ct - z_T)^2 = \rho_T^2, \tag{4.5}$$

which can be rewritten as

$$kt^2 + lt + m = 0, \tag{4.6}$$

where the new coefficients are defined as

$$\begin{aligned} k &= a^2 + b^2 + c^2 \\ l &= 2[a(x_C - x_T) + b(y_C - y_T) + c(z_C - z_T)] \\ m &= x_T^2 + y_T^2 + z_T^2 + x_C^2 + y_C^2 + z_C^2 - 2(x_C x_T + y_C y_T + z_C z_T). \end{aligned} \tag{4.7}$$

The solutions of the Equation 4.6 are

$$t_{1,2} = \frac{-l \pm \sqrt{l^2 - 4km}}{2k}, \tag{4.8}$$

and, if $\sqrt{l^2 - 4km} > 0$, the line intersects the sphere at two points. Then, substituting the solution $t_{1,2}$ in (4.3) we obtain

$$\begin{cases} x = x_\mathrm{C} + at_{1,2} \\ y = y_\mathrm{C} + bt_{1,2} \\ z = z_\mathrm{C} + ct_{1,2} \end{cases} \tag{4.9}$$

which are the coordinates of the two intersection points on the surface. In the case of the altimetric observation model developed, the intersection point coordinates of interest, $\mathbf{r}_s = (x_s, y_s, z_s)$, are obviously those of the point nearer to the Cassini spacecraft.

4.5 The observation model developed for the OD process

The geometry of the altimetric observation model during the flyby is illustrated in Figure 4.2. In the reference frame centered on the barycenter of the Saturnian system, $\mathbf{r}_\mathrm{T}$ and $\mathbf{r}_\mathrm{C}$ are the position vectors of Titan and Cassini spacecraft respectively.

We assumed a spherical model for the surface of Titan. From recent studies [22], a biaxial ellipsoid shape fit yields a polar radius of 2574.20 km and an equatorial radius of 2575.08 with a difference of about 880 m between the two values, corresponding to a flattening of about 3.4×10^{-3}. This means to shift the surface by a maximum of about 900 m for the observations at the pole to a minimum of 0 m for the observations along the equator. Since the ground tracks read from the data file lie on mid to low latitude regions (the T30 ground track reaches 60 latitude), the shift would be 600 m at most. The values obtained for the standard deviation of the estimated states discussed in Section 6.2 are an indication that the measurement system accuracy is too low to be sensitive to shapes that differ from a sphere by such small flattening as currently estimated for Titan. Furthermore, assuming a spherical shape model for Titan is consistent with the model adopted by CO.RI.S.T.A for the altimetric signal processing.

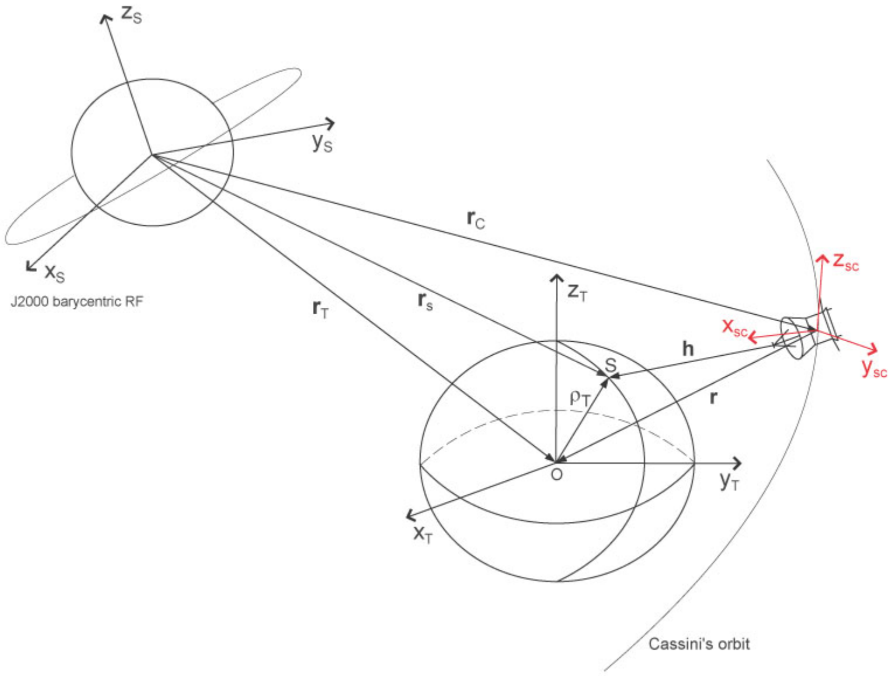

Figure 4.2: Geometry of the observation model and reference frames.

Defining $\mathbf{X}_{\mathrm{T}}^{\mathrm{sc}}$ as Titan's state vector with respect to Cassini spacecraft, $\mathbf{X}_{\mathrm{T}}$ and $\mathbf{X}_{\mathrm{C}}$ the state vectors of Titan and Cassini with respect to the $\{\mathbf{X_S}, \mathbf{Y_S}, \mathbf{Z_S}\}$ reference system, the relation between the state vectors is

$$\mathbf{X}_{\mathrm{T}}^{\mathrm{sc}} = \mathbf{X}_{\mathrm{T}} - \mathbf{X}_{\mathrm{C}}, \tag{4.10}$$

explicitly

$$\left(\begin{array}{c} \mathbf{r} \\ \mathbf{v} \end{array}\right) = \left(\begin{array}{c} \mathbf{r}_{\mathrm{T}} \\ \mathbf{v}_{\mathrm{T}} \end{array}\right) - \left(\begin{array}{c} \mathbf{r}_{\mathrm{C}} \\ \mathbf{v}_{\mathrm{C}} \end{array}\right). \tag{4.11}$$

As we have found the point S on Titan's surface (Section 4.4), we can compute its position with respect to Titan's center of mass (Figure 4.2) as:

$$\boldsymbol{\rho}_{\mathrm{T}} = \mathbf{r}_s - \mathbf{r}_{\mathrm{T}}. \tag{4.12}$$

and $\rho_T \simeq 2575$ km. Then, the altimeter measurement vector, $\mathbf{h}$, is given by (Figure 4.2)

$$\mathbf{h}(t) = \mathbf{r}(t) + \boldsymbol{\rho}_{\mathrm{T}} \tag{4.13}$$

where $\mathbf{r}(t)$ is the Titan's position vector expressed in barycentric coordinates system. If we use the relations (4.12) and (4.11), then

$$\begin{aligned} \mathbf{h}(t) &= \mathbf{r}_{\mathrm{T}}(t) - \mathbf{r}_{\mathrm{C}}(t) + \mathbf{r}_s(t) - \mathbf{r}_{\mathrm{T}}(t) \\ &= \mathbf{r}_s(t) - \mathbf{r}_{\mathrm{C}}(t). \end{aligned} \tag{4.14}$$

Finally, in the barycentric reference frame, the observation model expressed in terms of Titan's state $\mathbf{X}_{\mathrm{T}}$ is the instantaneous geometric distance (range)

$$\mathbf{G}(\mathbf{X}_{\mathrm{T}}, t) = h(t) = \left[(\mathbf{r}_s(t) - \mathbf{r}_{\mathrm{C}}(t)) \cdot (\mathbf{r}_s(t) - \mathbf{r}_{\mathrm{C}}(t))\right]^{\frac{1}{2}}. \tag{4.15}$$

Titan's rotation period is $15^{\mathrm{d}}\,22^{\mathrm{h}}\,41^{\mathrm{m}}\,24^{\mathrm{s}}$ (3321684 s), which means 0.94071° per hour or $2.6131 \cdot 10^{-4}$ degrees per second. Since pulses are separated by $1-3$ sec, then in 3 seconds Titan rotates by $7.84 \cdot 10^{-4}$ degrees, which corresponds to 35 m on the equator, so that we can neglect the effect of the rotation on the altimetric measurement computation.

We remark here that the altimetric measurement is a scalar quantity, but the observation model developed has a vectorial form as expressed by Equation (4.15). As consequence, there are different Titan's state configurations that yield the same altimetric measurement value at a given observation time. The dynamics of the system is not compatible with the existence of all of them. However, due to the short length of the orbital arcs available for the data reduction process, it is not possible to reduce the number of configurations sufficiently to give an estimation as accurate as the altimetric data.

4.5.1 Observation model partials

If the radar altimeter measurements are to be processed as observations for orbit determination, the partials derivatives of the altimeter measurement with respect to the Titan's state vector at epoch in the barycentric reference frame are required (see Equation 3.6). The partial derivatives with respect to the parameters which are concerned with the dynamics of the body (in this case the epoch position and velocity), must be determined according to the chain rule:

$$\frac{\partial \mathbf{G}(\mathbf{X}_{\mathrm{T}}, t)}{\partial \mathbf{X}_{\mathrm{T}}^{0}} = \frac{\partial \mathbf{G}(\mathbf{X}_{\mathrm{T}}, t)}{\partial \mathbf{X}_{\mathrm{T}}(t)} \frac{\partial \mathbf{X}_{\mathrm{T}}(t)}{\partial \mathbf{X}_{\mathrm{T}}^{0}}. \tag{4.16}$$

The partial derivatives $\frac{\partial \mathbf{G}(\mathbf{X}_{\mathrm{T}}, t)}{\partial \mathbf{X}_{\mathrm{T}}(t)}$ are computed directly at the given observation time and the partials $\frac{\partial \mathbf{X}_{\mathrm{T}}(t)}{\partial \mathbf{X}_{\mathrm{T}}^{0}}$ are extracted from the transition matrix $\mathbf{\Phi}$ obtained by the numerical integration of the celestial bodies' motion involved in the process. Explicitly, the first term on the right side of Equation (4.16) is

$$\frac{\partial \mathbf{G}(\mathbf{X}_{\mathrm{T}}, t)}{\partial \mathbf{X}_{\mathrm{T}}(t)} = \begin{bmatrix} \frac{\partial \mathbf{G}(\mathbf{X}, t)}{\partial \mathbf{r}_{\mathrm{T}}(t)} \\ \frac{\partial \mathbf{G}(\mathbf{X}, t)}{\partial \mathbf{v}_{\mathrm{T}}(t)} \end{bmatrix} = \begin{bmatrix} \frac{\partial h(t)}{\partial \mathbf{r}_{\mathrm{T}}(t)} \\ \frac{\partial h(t)}{\partial \mathbf{v}_{\mathrm{T}}(t)} \end{bmatrix}. \tag{4.17}$$

The partial derivatives of the observation model with respect to Titan's velocity vector are identically zero, $\frac{\partial \mathbf{G}(\mathbf{X}, t)}{\partial \mathbf{v}_{\mathrm{T}}(t)} = 0$, while the partials with respect to the position vector are given by (see Eq.(4.15))

$$\begin{aligned} \frac{\partial h(t)}{\partial \mathbf{r}_{\mathrm{T}}(t)} &= \frac{\partial}{\partial \mathbf{r}_{\mathrm{T}}(t)} \Big[(\mathbf{r}_s(t) - \mathbf{r}_{\mathrm{C}}(t)) \cdot (\mathbf{r}_s(t) - \mathbf{r}_{\mathrm{C}}(t)) \Big]^{\frac{1}{2}} \\ &= \frac{1}{2h} \frac{\partial}{\partial \mathbf{r}_{\mathrm{T}}(t)} (\mathbf{r}_s(t) - \mathbf{r}_{\mathrm{C}}(t))^2 \\ &= \frac{(\mathbf{r}_s(t) - \mathbf{r}_{\mathrm{C}}(t))}{h} \left[\frac{\partial \mathbf{r}_s(t)}{\partial \mathbf{r}_{\mathrm{T}}(t)} - \frac{\partial \mathbf{r}_{\mathrm{C}}(t)}{\partial \mathbf{r}_{\mathrm{T}}(t)} \right] \\ &= \hat{\mathbf{h}}^T \frac{\partial \mathbf{r}_s(t)}{\partial \mathbf{r}_{\mathrm{T}}(t)}, \end{aligned} \tag{4.18}$$

where $\frac{\partial \mathbf{r}_{\mathrm{C}}(t)}{\partial \mathbf{r}_{\mathrm{T}}(t)}$ is null. If we denote the altimetric measurement vector components as $\mathbf{h} = (h_x, h_y, h_z)$, the range is expressed as $h = \sqrt{h_x^2 + h_y^2 + h_z^2}$ and the unit vector in (4.18) is

$$\hat{\mathbf{h}} = \begin{pmatrix} \frac{h_x}{h} & \frac{h_y}{h} & \frac{h_z}{h} \end{pmatrix}. \tag{4.19}$$

Using the parametric relations (4.9), the partials $\frac{\partial \mathbf{r}_s(t)}{\partial \mathbf{r}_{\mathrm{T}}(t)}$ are computed as follows:

$$\frac{\partial \mathbf{r}_s}{\partial \mathbf{r}_{\mathrm{T}}} = \begin{pmatrix} \frac{\partial x}{\partial x_{\mathrm{T}}} & \frac{\partial x}{\partial y_{\mathrm{T}}} & \frac{\partial x}{\partial z_{\mathrm{T}}} \\ \frac{\partial y}{\partial x_{\mathrm{T}}} & \frac{\partial y}{\partial y_{\mathrm{T}}} & \frac{\partial y}{\partial z_{\mathrm{T}}} \\ \frac{\partial z}{\partial x_{\mathrm{T}}} & \frac{\partial z}{\partial y_{\mathrm{T}}} & \frac{\partial z}{\partial z_{\mathrm{T}}} \end{pmatrix} = \frac{\partial}{\partial \mathbf{r}_{\mathrm{T}}} \begin{pmatrix} x_s \\ y_s \\ z_s \end{pmatrix} = \begin{pmatrix} a \\ b \\ c \end{pmatrix} \frac{\partial t}{\partial \mathbf{r}_{\mathrm{T}}} = \begin{pmatrix} a \\ b \\ c \end{pmatrix} \begin{pmatrix} \frac{\partial t}{\partial x_{\mathrm{T}}} & \frac{\partial t}{\partial y_{\mathrm{T}}} & \frac{\partial t}{\partial z_{\mathrm{T}}} \end{pmatrix}. \tag{4.20}$$

As in Eqns. (4.7), only l and m are dependent on $\mathbf{r}_{\mathrm{T}}$, so the derivative $\frac{\partial t}{\partial \mathbf{r}_{\mathrm{T}}}$ is

$$\begin{aligned} \frac{\partial t}{\partial \mathbf{r}_{\mathrm{T}}} &= \frac{1}{2k}\left[-\frac{\partial l}{\partial \mathbf{r}_{\mathrm{T}}} \pm \frac{1}{2\sqrt{l^2-4km}}\left(2l\frac{\partial l}{\partial \mathbf{r}_{\mathrm{T}}} - 4k\frac{\partial m}{\partial \mathbf{r}_{\mathrm{T}}}\right)\right] \\ &= \frac{1}{2k}\left[-\frac{\partial l}{\partial \mathbf{r}_{\mathrm{T}}} \pm \frac{1}{\sqrt{l^2-4km}}\left(l\frac{\partial l}{\partial \mathbf{r}_{\mathrm{T}}} - 2k\frac{\partial m}{\partial \mathbf{r}_{\mathrm{T}}}\right)\right] \end{aligned} \tag{4.21}$$

The last terms to compute are the partials $\frac{\partial l}{\partial \mathbf{r}_{\mathrm{T}}}$ and $\frac{\partial m}{\partial \mathbf{r}_{\mathrm{T}}}$. From their definitions given in (4.7) we obtain

$$\frac{\partial l}{\partial \mathbf{r}_{\mathrm{T}}} = \begin{pmatrix} \frac{\partial l}{\partial x_{\mathrm{T}}} & \frac{\partial l}{\partial y_{\mathrm{T}}} & \frac{\partial l}{\partial z_{\mathrm{T}}} \end{pmatrix} = \begin{pmatrix} -2a & -2b & -2c \end{pmatrix} = -2\begin{pmatrix} a & b & c \end{pmatrix} \tag{4.22}$$

$$\frac{\partial m}{\partial \mathbf{r}_{\mathrm{T}}} = \begin{pmatrix} \frac{\partial m}{\partial x_{\mathrm{T}}} & \frac{\partial m}{\partial y_{\mathrm{T}}} & \frac{\partial m}{\partial z_{\mathrm{T}}} \end{pmatrix} = \begin{pmatrix} 2x_{\mathrm{T}} - 2x_{\mathrm{C}} \\ 2y_{\mathrm{T}} - 2y_{\mathrm{C}} \\ 2z_{\mathrm{T}} - 2z_{\mathrm{C}} \end{pmatrix}^T = 2\left[\begin{pmatrix} x_{\mathrm{T}} \\ y_{\mathrm{T}} \\ z_{\mathrm{T}} \end{pmatrix}^T - \begin{pmatrix} x_{\mathrm{C}} \\ y_{\mathrm{C}} \\ z_{\mathrm{C}} \end{pmatrix}^T\right] = 2\left(\mathbf{r}_{\mathrm{T}}^T - \mathbf{r}_{\mathrm{C}}^T\right). \tag{4.23}$$

This completes the computation of the partial derivatives (4.18).

Chapter 5

Titan Flybys and Altimetric Data Description

5.1 Introduction

Cassini's RADAR flybys activities have been planned for 22 Titan encounters and the altimetric radar mode operated in 19 of these flybys. The complete list of the flybys with the RADAR activities planned is presented at the and of this chapter in Figure 5.14. Up to now we have received the altimetric data information about 14 of the 19 encounters, beginning from the flyby completed on 26th October 2004 (Ta) and up to the one completed on 20th December 2007 (T39), except for Titan flyby T7 and T31. We are waiting for these missing flybys and for the last three Titan's encounters executed in the last part of the nominal mission (T41, T43 and T44).

The Orbit Determination run is performed separately for each of these flybys and the results obtained are presented in Chapter 6. In this chapter we give the detailed description of the altimetric observations we've received and the way they are used as input for the Orbit Determination process. Moreover, we describe the useful data fields available on Planetary Data System's Data Service.

A general descriptions of the flybys during which the altimetric data have been collected is presented here together with 3D Matlab figures and tables summarizing their distribution over the flyby length.

5.2 The observed altimetric data

The altimetric observation is the distance, or rather *the range-to-target* (*RTT*), measured from the antenna's center of phase to the interception point on the surface of the target body. Here we indicate the basic characteristics of the instrument when it works in the altimetric mode:

Radar Instrument characteristics	
Radar mode	9 (= altimetry)
Radar beam used	3 (central beam)
Bandwidth	13.78 GHz
Resolution	24-27 km horizontal res 100-150 m vertical res

The RADAR altimeter data have been gently received from CO.RI.S.T.A. and they consist of *.csv* extension files where each row represents one burst of data and contains 17 parameters; one of the parameter is the altimetric range value computed for that burst. The measurement errors are not available. The fields we take from these data tables, which are necessary for the construction of the altimetric data files used as input by the software developed (Appendix B), are the following:

1. `burst id`, an integer which uniquely identifies each burst throughout the mission;
2. `t utc ymd`, time at start burst expressed as UTC time tag in yyyy-mm-ddT:hh:mm:ss.sss. Times in this format are then converted in ephemeris times expressed in seconds since 12:00 AM Jan.1, 2000;
3. `height`, an integer which gives the distance in meters from Titan's reference surface (2575 km radius) computed at a time offset in seconds from burst reference time. The height value is the observed measure in the residuals computation of the orbit determination process (section 3).

The offset values are available in the Short Burst Data Record (SBDR) table ([19]) and they are needed to evaluate the correct observations times, computed altimetric measures (height values) and geometric fields used in the Orbit Determination process. Their values are expressed in seconds and should be added to the ephemeris time read from the data file which is, in reality, the electromagnetic field emission time. We proved that the offset values correspond to the correction for light-time, so we decided to applie the correction instead of using the offset field in the software code implementation. Moreover, the reason of this choice is the fact that up to now the flybys' SBDR tables are not all available and then in this way we make our software independent from any data fields contained in the tables. The geometry of the real altimetric observation is illustrated in Figure 5.1. The measurement involves three times: the emission time t_{emiss} when the electromagnetic field leaves the antenna, the observation time t_{obs} when the signal reaches the target surface and finally the reception time t_{rec} when the radar beam comes back to the antenna. As specified by CO.RI.S.T.A, the altimetric values in the files have been computed at $t_{\text{obs}} = t_{\text{emiss}} + \text{offset}(t_{\text{emiss}})$, that is as applying the light time correction to the emission time. Since the read in values of height are already corrected for light time, we applie the correction to Cassini and Titan's position vectors in the altimetric observation model. In this way, we get the Cassini and Titan's state values at t_{obs} to compute the correct geometric ranges at a given observation time. Despite that, we noticed that neglecting the offset addition or the light time correction could change Titan's states estimation in an appreciable way. In fact, if we consider the time intervals $\Delta t_1 = t_{\text{obs}} - t_{\text{emiss}}$ and $\Delta t_2 = t_{\text{rec}} - t_{\text{obs}}$, the quantity $\Delta T \cdot c = (\Delta t_2 - \Delta t_1) \cdot c$ is of the same order magnitude of RADAR vertical resolution value as in Figure 5.2. In order to maintain the correctness in our solution procedure we applied the correction for the light time in the view of the extension to different mission scenarios.

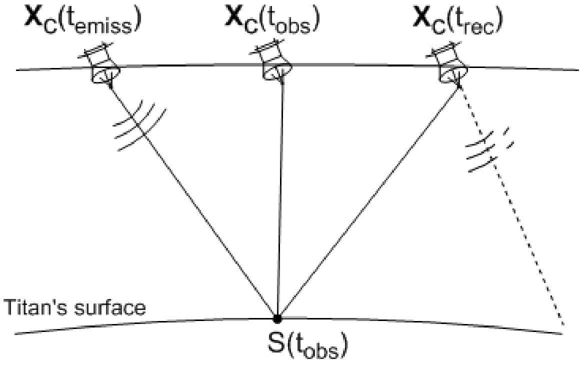

Figure 5.1: Times involved in the altimetric measurement and correction for light time.

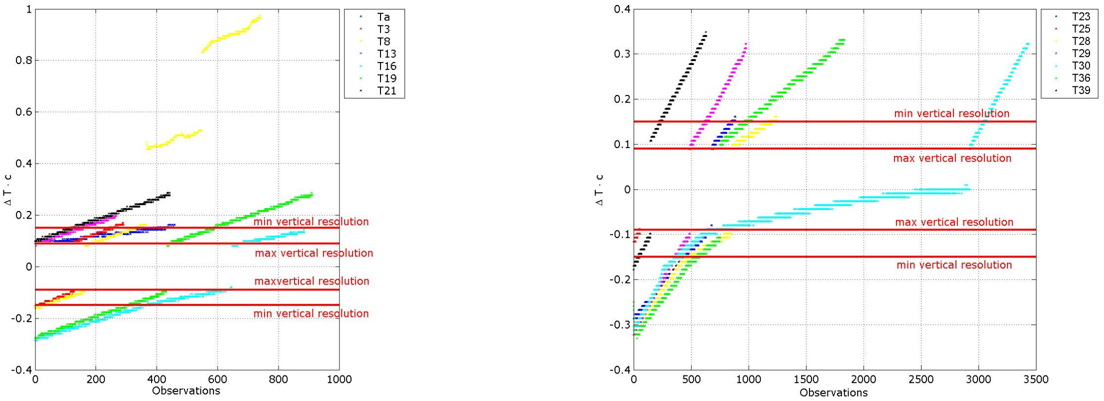

Figure 5.2: Plot of the $\Delta T \cdot c$ quantities for each flyby: the flybys have been divided in 2 groups for more clarity in the graphics. The values are of the same order magnitude of RADAR resolution.

5.2.1 The Short Burst Data Record(SBDR)

The Short Burst Data Record (SBDR) are comprised in the Cassini Burst Ordered Data Products (BODP) data sets together with the Long Burst Data Record (LBDR) and the Altimeter Burst Data Record (ABDR) ([19]). The BODP can be found on the Imaging Node Server of the Planetary Data System (PDS) and they are comprehensive data files that include engineering telemetry, radar operational parameters, row echo data, instrument viewing geometry, and calibrated science data. The BODP files contain time-ordered fixed length records; each record corresponds to the full set of relevant data for an individual radar burst. The LBDRs include the echo data but not the altimeter profile, the ABDRs include the altimeter profile but not the echo data and the SBDRs include neither. This because the two fields in question are much larger than all the other data fields combined. The ABDRs are not available for all the flybys, so we preferred to apply to CO.RI.S.T.A. in order to receive the altimetric range values we needed.

A SBDR record is produced for every burst throughout the passage and each record is divided into three consecutive segments from three different levels of processing: 1) the engineering data segment, 2) the intermediate level data segment and, 3) the science data segment. Different fields have been read from each segment in order to set up procedures that test the consistence of the data received. The fields containing the spacecraft's state and attitude values have been extracted to create SPICE kernels. The kernels are loaded by the Measurement Simulation run (one of the software capability implemented, Appendix B) in the case of the altimetric measurements simulation. The complete description of the SBDR data fields can be found in [19].

5.3 Titan flybys description and time distribution of the measurements

The altimetric measurements received have been collected in 14 Titan flybys and their number for each passage is listed in the Table 5.1. The Data Search Service (DSS) of PDS provides SPICE SP-kernel files for Cassini spacecraft trajectory and kernel files with planetary and satellite ephemerides used by the CASSINI project. For each flyby arc, of which we have received the data files, we downloaded `SPK` kernels named as `"SCPSE"` consisting in merged spacecraft, planetary and satellites ephemerides files. In particular we chose the reconstructed trajectory files and their last version available online. At the same time we downloaded the respective C-kernel files providing the reconstructed Cassini 's attitude

Altimetric observations summary	
Titan Flyby	**N° altimetric data**
Titan flyby Ta	459
Titan flyby T3	291
Titan flyby T8	742
Titan flyby T13	268
Titan flyby T16	886
Titan flyby T19	911
Titan flyby T21	444
Titan flyby T23	887
Titan flyby T25	57
Titan flyby T28	1248
Titan flyby T29	982
Titan flyby T30*	3439
Titan flyby T36*	1833
Titan flyby T39*	633
Total	**13080**

Table 5.1: Number of altimetric observations for each flyby. The SBDRs data tables of the flybys denoted by * are not actually present in PDS.

together with the kernels concerning the spacecraft's clock they are referred to. All files are in binary format and we implemented a simple SPICE-based routine that reads the ephemerides files and gives three output files containing respectively: 1) Cassini barycentric states, 2) Titan barycentric states and 3) Cassini states in Titan-centered reference frame. Then, by the use of Matlab, the states have been plotted in order to visualize the entire encounters in two different ways: the first one is the Titan-centric representation of the flyby, while the second one is the orthogonal projection on the xy plane of the Saturn-barycentric passage (Figures 5.3-5.13). For each available flyby, we give its general description as duration and the closest approach distance and time. Moreover we give tables that summarize the distribution over time of the altimetric observation sequence. A typical Titan encounter should provide a determined sequence of observations as explained in Section 1.3.1, but this seems to be not followed in all flybys. For example, as we can see from Figure 5.5, representing Titan flyby T8, there are three orbital arc during which altimetric radar mode is working, while in Figure 5.7, representing Titan flyby T16, the arc is only one.

In the following tables, the flyby length is computed as the time difference between the first and the last ephemeris time values given in the SBDR data tables. Times are expressed in the ephemeris seconds past J2000 (ET) and in Ephemeris Calendar Time Strings (TDB) and distances are in kilometers.

Titan flyby Ta

Titan Flyby Ta	**26 October 2004**

Flyby Description	
Fields	*Values*
Flyby t_{start}	$2004-10-26T10:21:20.000$ (152058075.0101)
Flyby t_{end}	$2004-10-26T20:29:52.000$ (152094599.0185)
Flyby length (hh mm ss)	$10^{\text{h}}8^{\text{m}}44.008^{\text{s}}$
Time of closest approach t_{cl}	$2004-10-26T15:31:12.000$ (152076668.7513)
Closest approach distance (km)	1174.116

Data Used Time Distribution	
Fields	*Values*
Altimetric data acquisition initial time t_{i}	$2004-10-26T15:50:08.000$ (152077812.8693)
Altimetric data acquisition final time t_{f}	$2004-10-26T16:01:04.000$ (152078466.8459)
Number of observations	459

Total number of altimetric observations used	**459**

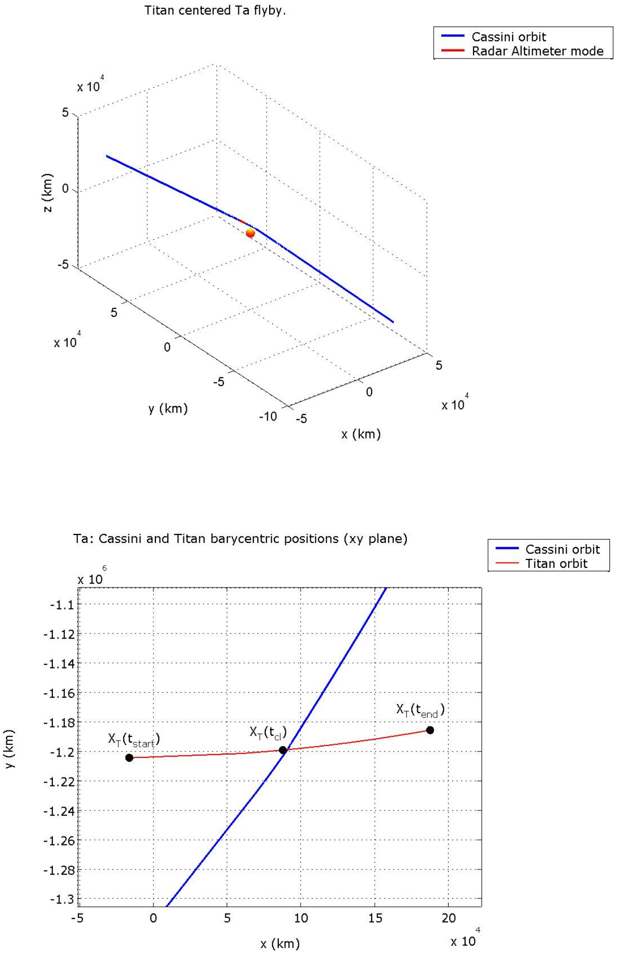

Figure 5.3: Titan flyby Ta: plot of Cassini orbit with the red arcs when the altimeter mode is on, and plot of Cassini orbit and Titan's positions during the flyby on xy barycentric plane.

Titan flyby T3

Titan Flyby T3	**15 February 2005**

Flyby Description	
Fields	*Values*
Flyby t_{start}	$2005-02-15T02:18:56.000$ (161705938.9870)
Flyby t_{end}	$2005-02-15T08:05:20.000$ (161726720.8517)
Flyby length (hh mm ss)	$5^{\text{h}}46^{\text{m}}21.865^{\text{s}}$
Time of closest approach t_{cl}	$2005-02-15T06:58:56.000$ (161722737.2381)
Closest approach distance (km)	1578.967

Data Used Time Distribution	
Fields	*Values*
Altimetric data acquisition initial time t_{i}	$2005-02-15T06:28:16.000$ (161720903.0983)
Altimetric data acquisition final time t_{f}	$2005-02-15T06:37:20.000$ (161721442.5601)
Number of observations	129
Time gap (hh mm ss)	$0^{\text{h}}42^{\text{m}}42.508^{\text{s}}$
Altimetric data acquisition initial time t_{i}	$2005-02-15T07:20:60.000$ (161724005.0685)
Altimetric data acquisition final time t_{f}	$2005-02-15T07:31:28.000$ (161724683.3601)
Number of observations	162

Total number of altimetric observations used	**291**

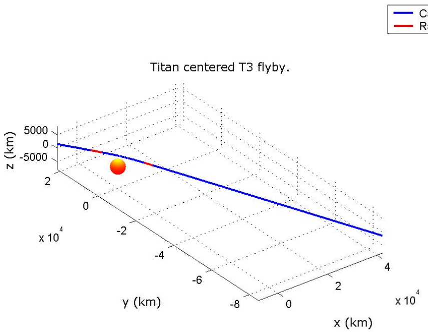

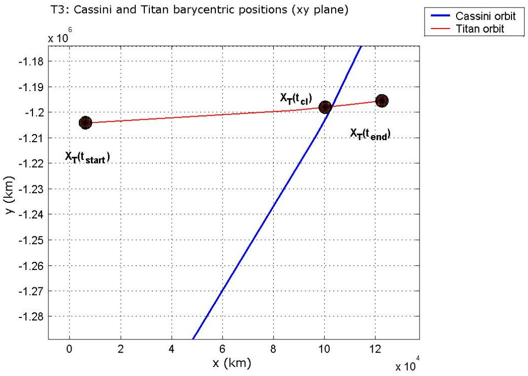

Figure 5.4: Titan flyby T3: plot of Cassini orbit with the red arcs when the altimeter mode is on, and plot of Cassini orbit and Titan's positions during the flyby on xy barycentric plane.

Titan flyby T8

Titan Flyby T8	**28 October 2005**

Flyby Description	
Fields	*Values*
Flyby t_{start}	$2005 - 10 - 27T18 : 38 : 24.000$ (183710305.3677)
Flyby t_{end}	$2005 - 10 - 28T09 : 20 : 48.000$ (183763253.1078)
Flyby length (hh mm ss)	$14^{\text{h}}42^{\text{m}}27.740^{\text{s}}$
Time of closest approach t_{cl}	$2005 - 10 - 28T04 : 16 : 32.000$ (183744988.5794)
Closest approach distance (km)	1353.042

Data Used Time Distribution	
Fields	*Values*
Altimetric data acquisition initial time t_{i}	$2005 - 10 - 28T03 : 44 : 00.000$ (183743039.1901)
Altimetric data acquisition final time t_{f}	$2005 - 10 - 28T03 : 54 : 56.000$ (183743695.0788)
Number of observations	165
Time gap (hh mm ss)	$0^{\text{h}}40^{\text{m}}40.079^{\text{s}}$
Altimetric data acquisition initial time t_{i}	$2005 - 10 - 28T04 : 35 : 28.000$ (183746135.1574)
Altimetric data acquisition final time t_{f}	$2005 - 10 - 28T04 : 48 : 48.000$ (183746935.1662)
Number of observations	201
Time gap (hh mm ss)	$0^{\text{h}}47^{\text{m}}34.033^{\text{s}}$
Altimetric data acquisition initial time t_{i}	$2005 - 10 - 28T05 : 36 : 32.000$ (183749789.1988)
Altimetric data acquisition final time t_{f}	$2005 - 10 - 28T06 : 01 : 36.000$ (183751288.8938)
Number of observations	376

Total number of altimetric observations used	**742**

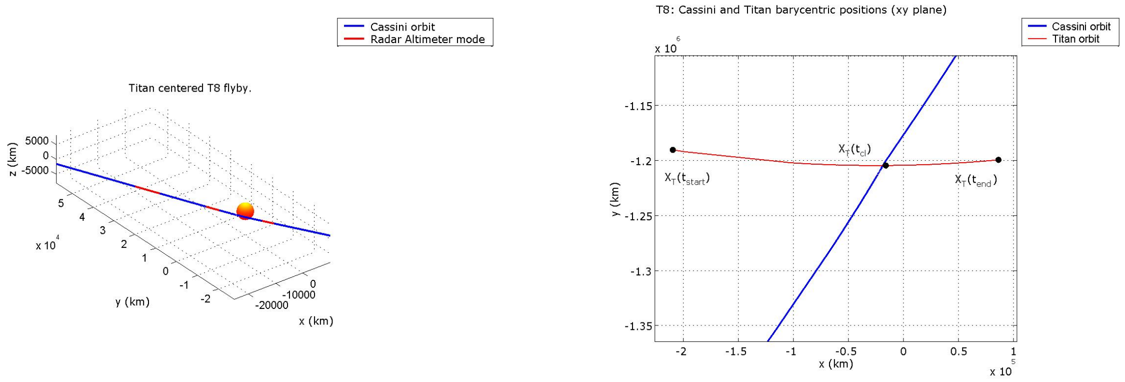

Figure 5.5: Titan flyby T8: plot of Cassini orbit with the red arcs when the altimeter mode is on, and plot of Cassini orbit and Titan's positions during the flyby on xy barycentric plane.

Titan flyby T13

Titan Flyby T13	**30 April 2006**

Flyby Description	
Fields	*Values*
Flyby t_{start}	$2006-04-30T20:47:28.000$ (199702052.6064)
Flyby t_{end}	$2006-05-01T02:13:52.000$ (199721624.3483)
Flyby length (hh mm ss)	$5^{\text{h}}26^{\text{m}}11.742^{\text{s}}$
Time of closest approach t_{cl}	$2006-04-30T20:59:12.000$ (199702758.8019)
Closest approach distance (km)	1855.749

Data Used Time Distribution	
Fields	*Values*
Altimetric data acquisition initial time t_{i}	$2006-04-30T21:19:28.000$ (199703966.3901)
Altimetric data acquisition final time t_{f}	$2006-04-30T21:37:20.000$ (199705034.1010)
Number of observations	268

Total number of altimetric observations used	**268**

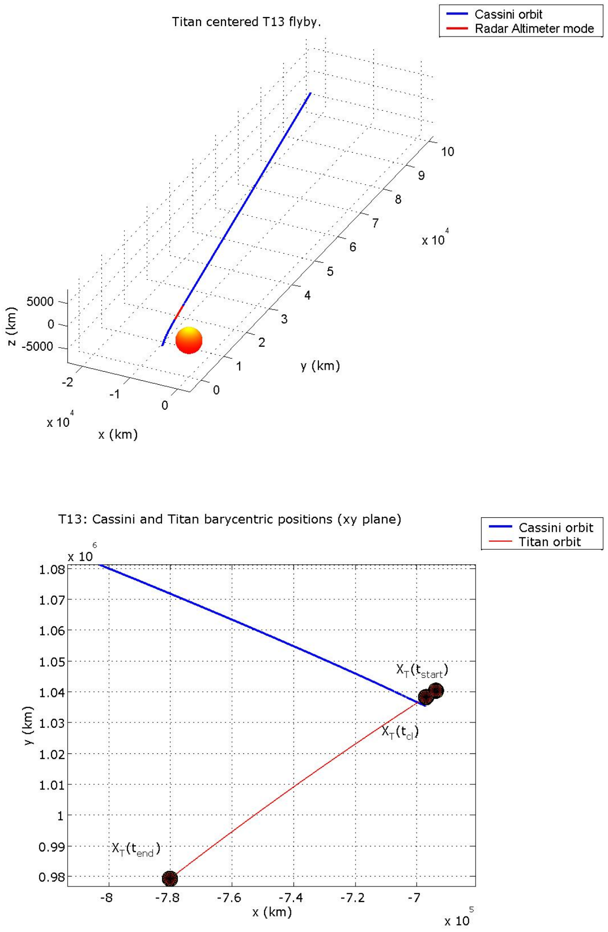

Figure 5.6: Titan flyby T13: plot of Cassini orbit with the red arcs when the altimeter mode is on, and plot of Cassini orbit and Titan's positions during the flyby on xy barycentric plane.

Titan flyby T16

Titan Flyby T16	**22 July 2006**

Flyby Description	
Fields	*Values*
Flyby t_{start}	$2006-07-21T16:31:28.000$ (206771491.2662)
Flyby t_{end}	$2006-07-22T00:55:44.000$ (206801751.8730)
Flyby length (hh mm ss)	$8^{\text{h}}24^{\text{m}}20.607^{\text{s}}$
Time of closest approach t_{cl}	$2006-07-22T00:26:24.000$ (206799991.0180)
Closest approach distance (km)	949.891

Data Used Time Distribution	
Fields	*Values*
Altimetric data acquisition initial time t_{i}	$2006-07-21T23:34:24.000$ (206796870.1568)
Altimetric data acquisition final time t_{f}	$2006-07-22T00:06:24.000$ (206798787.9129)
Number of observations	648
Time gap (hh mm ss)	$0^{\text{h}}39^{\text{m}}37.182^{\text{s}}$
Altimetric data acquisition initial time t_{i}	$2006-07-22T00:46:08.000$ (206801165.0952)
Altimetric data acquisition final time t_{f}	$2006-07-22T00:54:56.000$ (206801689.7064)
Number of observations	94

Total number of altimetric observations used	**886**

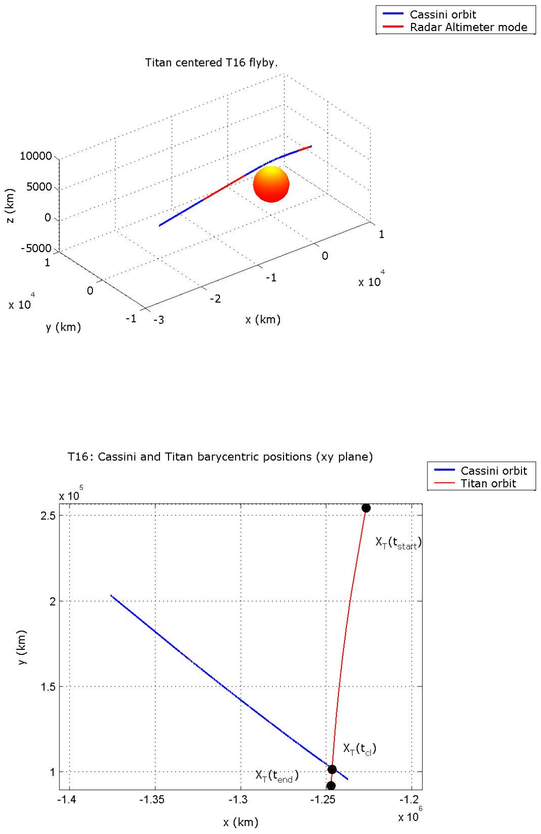

Figure 5.7: Titan flyby T16: plot of Cassini orbit with the red arcs when the altimeter mode is on, and plot of Cassini orbit and Titan's positions during the flyby on xy barycentric plane.

Titan flyby T19

Titan Flyby T19	**09 October 2006**

Flyby Description	
Fields	*Values*
Flyby t_{start}	$2006-10-09T09:16:16.000$ (213657373.3009)
Flyby t_{end}	$2006-10-09T22:45:36.000$ (213705936.0880)
Flyby length (hh mm ss)	$13^{\text{h}}29^{\text{m}}22.787^{\text{s}}$
Time of closest approach t_{cl}	$2006-10-09T17:31:12.000$ (213687072.0096)
Closest approach distance (km)	979.711

Data Used Time Distribution	
Fields	*Values*
Altimetric data acquisition initial time t_{i} Altimetric data acquisition final time t_{f} Number of observations	$2006-10-09T16:40:16.000$ (213684011.1816) $2006-10-09T17:09:04.000$ (213685747.0264) 432
Time gap (hh mm ss)	$0^{\text{h}}41^{\text{m}}52.096^{\text{s}}$
Altimetric data acquisition initial time t_{i} Altimetric data acquisition final time t_{f} Number of observations	$2006-10-09T17:50:56.000$ (213688259.1223) $2006-10-09T18:23:12.000$ (213690185.1448) 479

Total number of altimetric observations used	**911**

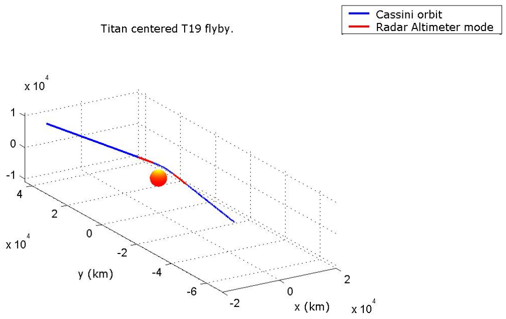

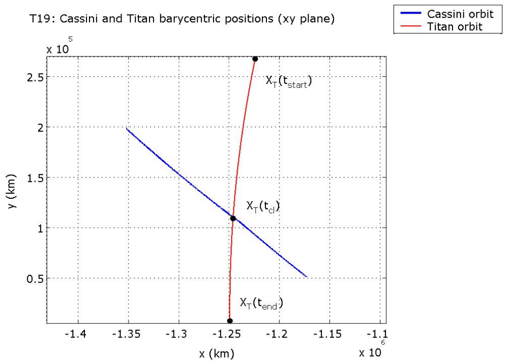

Figure 5.8: Titan flyby T19: plot of Cassini orbit with the red arcs when the altimeter mode is on, and plot of Cassini orbit and Titan's positions during the flyby on xy barycentric plane.

Titan flyby T21

Titan Flyby T21	**12 December 2006**

Flyby Description	
Fields	*Values*
Flyby t_{start}	$2006-12-12T09:02:40.000$ (219186158.1288)
Flyby t_{end}	$2006-12-12T15:37:04.000$ (219209820.0360)
Flyby length (hh mm ss)	$6^{\mathrm{h}}34^{\mathrm{m}}21.907^{\mathrm{s}}$
Time of closest approach t_{cl}	$2006-12-12T11:42:40.000$ (219195756.0443)
Closest approach distance (km)	999.984

Data Used Time Distribution	
Fields	*Values*
Altimetric data acquisition initial time t_{i}	$2006-12-12T12:04:48.000$ (219197082.0807)
Altimetric data acquisition final time t_{f}	$2006-12-12T12:34:24.000$ (219198869.9077)
Number of observations	445

Total number of altimetric observations used	**445**

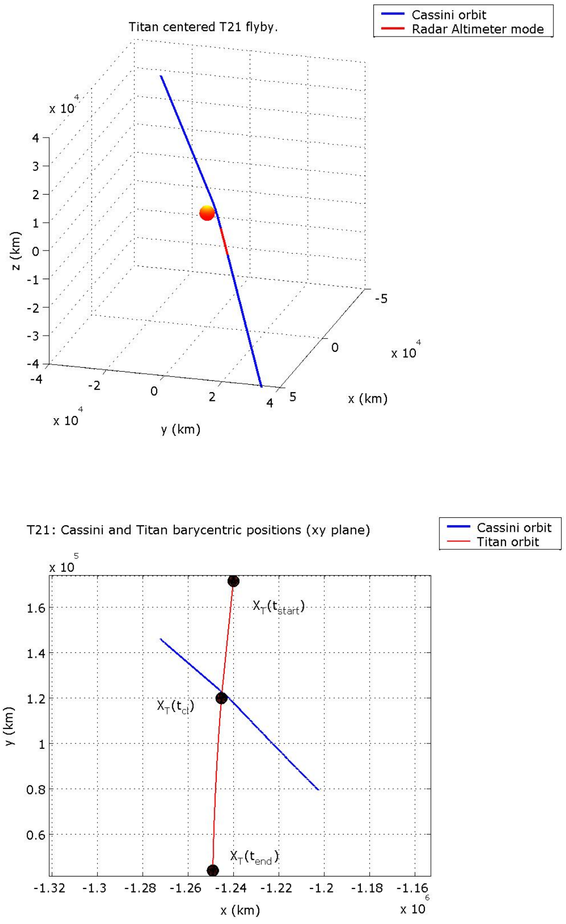

Figure 5.9: Titan flyby T21: plot of Cassini orbit with the red arcs when the altimeter mode is on, and plot of Cassini orbit and Titan's positions during the flyby on xy barycentric plane.

Titan flyby T23

Titan Flyby T23	**13 January 2007**

Flyby Description	
Fields	*Values*
Flyby t_{start}	$2007-01-13T00:44:48.000$ (221921087.7600)
Flyby t_{end}	$2007-01-13T13:34:08.000$ (221967250.5653)
Flyby length (hh mm ss)	$12^{\text{h}}49^{\text{m}}22.805^{\text{s}}$
Time of closest approach t_{cl}	$2007-01-13T08:39:28.000$ (221949575.9476)
Closest approach distance (km)	1000.266

Data Used Time Distribution	
Fields	*Values*
Altimetric data acquisition initial time t_{i} Altimetric data acquisition final time t_{f} Number of observations	$2007-01-13T07:47:28.000$ (221946454.6519) $2007-01-13T08:19:44.000$ (221948385.6012) 685
Time gap (hh mm ss)	$0^{\text{h}}40^{\text{m}}35.991^{\text{s}}$
Altimetric data acquisition initial time t_{i} Altimetric data acquisition final time t_{f} Number of observations	$2007-01-13T09:00:16.000$ (221950821.5921) $2007-01-12T09:09:36.000$ (221951383.5979) 202

Total number of altimetric observations used	**887**

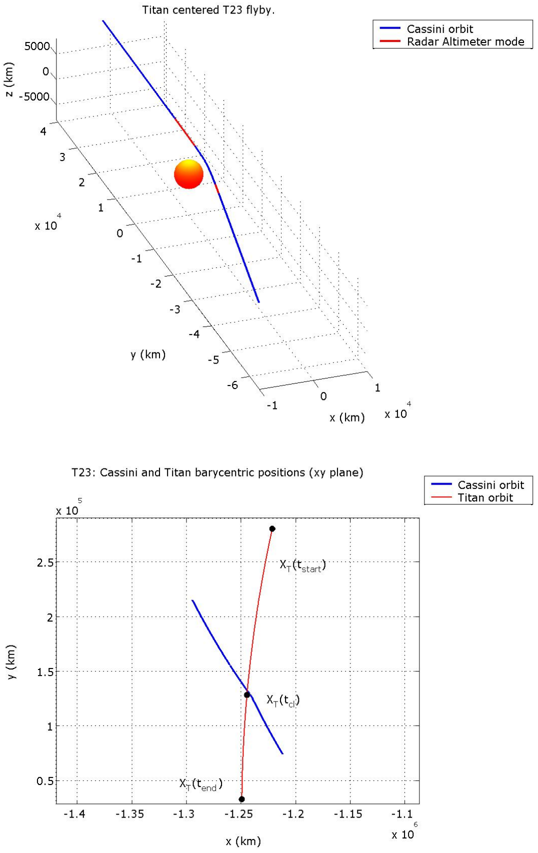

Figure 5.10: Titan flyby T23: plot of Cassini orbit with the red arcs when the altimeter mode is on, and plot of Cassini orbit and Titan's positions during the flyby on xy barycentric plane.

Titan flyby T25

Titan Flyby T25	**22 February 2007**

Flyby Description	
Fields	*Values*
Flyby t_{start}	$2007-02-22T02:50:24.000$ (225384627.9730)
Flyby t_{end}	$2007-02-22T07:58:56.000$ (225403132.8024)
Flyby length (hh mm ss)	$5^{\text{h}}08^{\text{m}}24.829^{\text{s}}$
Time of closest approach t_{cl}	$2007-02-22T03:13:36.000$ (225386009.0388)
Closest approach distance (km)	1000.371

Data Used Time Distribution	
Fields	*Values*
Altimetric data acquisition initial time t_{i}	$2007-02-22T02:50:24.000$ (225384627.9969)
Altimetric data acquisition final time t_{f}	$2007-02-22T02:54:24.000$ (225384863.8545)
Number of observations	57

Total number of altimetric observations used	**57**

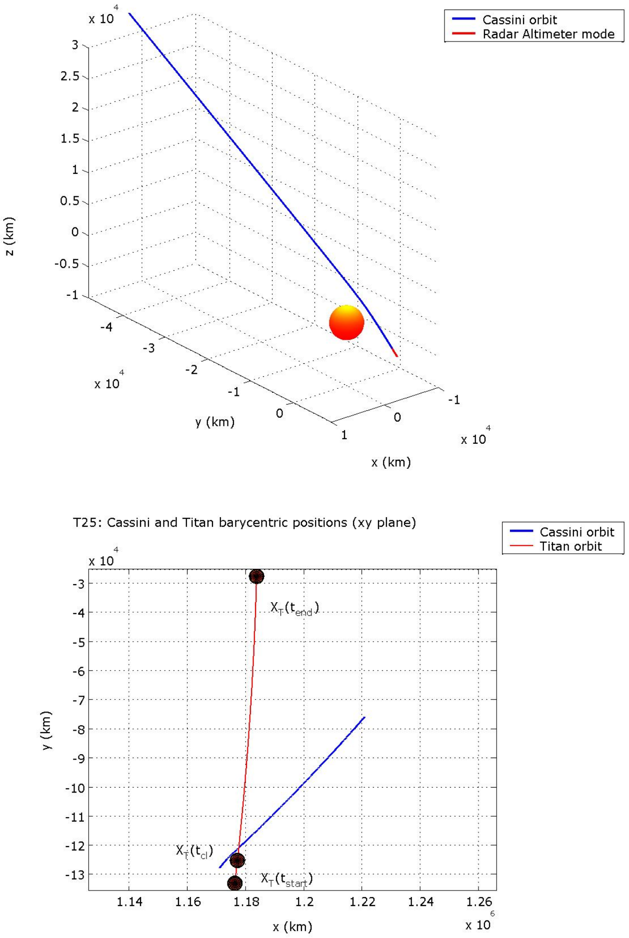

Figure 5.11: Titan flyby T25: plot of Cassini orbit with the red arcs when the altimeter mode is on, and plot of Cassini orbit and Titan's positions during the flyby on xy barycentric plane.

Titan flyby T28

Titan Flyby T28	**10 April 2007**

Flyby Description	
Fields	*Values*
Flyby t_{start}	$2007-04-10T15:04:32.000$ (229489476.8396)
Flyby t_{end}	$2007-04-10T23:28:00.000$ (229519678.6481)
Flyby length (hh mm ss)	$8^{\text{h}}23^{\text{m}}21.809^{\text{s}}$
Time of closest approach t_{cl}	$2007-04-10T22:59:12.000$ (229517944.8585)
Closest approach distance (km)	990.875

Data Used Time Distribution	
Fields	*Values*
Altimetric data acquisition initial time t_{i} Altimetric data acquisition final time t_{f} Number of observations	$2007-04-10T22:07:12.000$ (229514825.7348) $2007-04-10T22:39:12.000$ (229516756.1718) 853
Time gap (hh mm ss)	$0^{\text{h}}39^{\text{m}}35.501^{\text{s}}$
Altimetric data acquisition initial time t_{i} Altimetric data acquisition final time t_{f} Number of observations	$2007-04-10T23:18:56.000$ (229519131.6728) $2007-04-10T23:27:44.000$ (229519668.8183) 396

Total number of altimetric observations used	**1249**

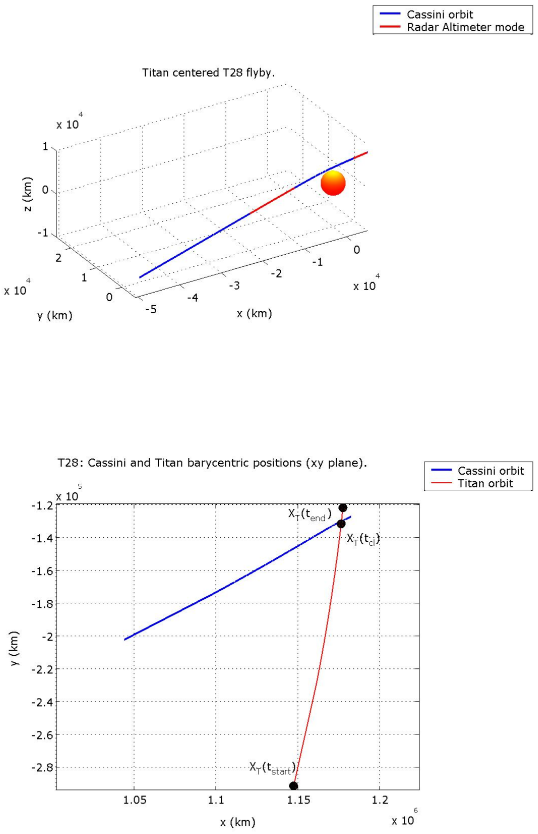

Figure 5.12: Titan flyby T28: plot of Cassini orbit with the red arcs when the altimeter mode is on, and plot of Cassini orbit and Titan's positions during the flyby on xy barycentric plane.

Titan flyby T29

Titan Flyby T29	**26 April 2007**

Flyby Description	
Fields	*Values*
Flyby t_{start}	$2007-04-26T16:49:04.000$ (230878145.0462)
Flyby t_{end}	$2007-04-27T02:23:12.000$ (230912597.9130)
Flyby length (hh mm ss)	$9^{\mathrm{h}}34^{\mathrm{m}}12.867^{\mathrm{s}}$
Time of closest approach t_{cl}	$2007-04-26T21:34:08.000$ (230895243.0506)
Closest approach distance (km)	980.814

Data Used Time Distribution	
Fields	*Values*
Altimetric data acquisition initial time t_{i}	$2007-04-26T20:21:04.000$ (230892064.0149)
Altimetric data acquisition final time t_{f}	$2007-04-26T21:13:36.000$ (230894008.4233)
Number of observations	490
Time gap (hh mm ss)	$0^{\mathrm{h}}40^{\mathrm{m}}11.527^{\mathrm{s}}$
Altimetric data acquisition initial time t_{i}	$2007-04-26T21:53:36.000$ (230896419.9503)
Altimetric data acquisition final time t_{f}	$2007-04-26T22:25:52.000$ (230898346.1105)
Number of observations	492
Total number of altimetric observations used	**982**

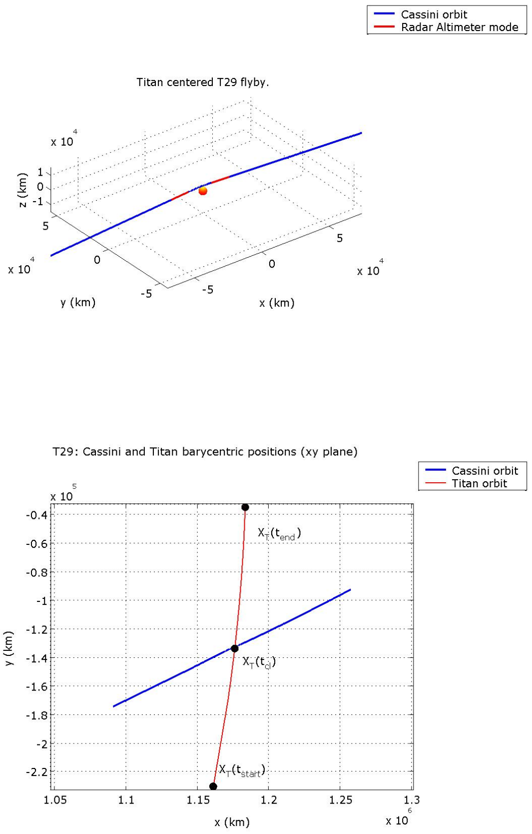

Figure 5.13: Titan flyby T29: plot of Cassini orbit with the red arcs when the altimeter mode is on, and plot of Cassini orbit and Titan's positions during the flyby on xy barycentric plane.

Titan flyby T30

In the altimetric data file of Titan's flyby T30 there are 9 very short time gaps of few seconds (between 11 s and 36 s) and they are not obviously reported in the table below. The SBDR table is not available in the PDS data system.

Titan Flyby T30	**12 May 2007**

Flyby Description	
Fields	*Values*
Flyby t_{start}	–
Flyby t_{end}	–
Flyby length (hh mm ss)	–
Time of closest approach t_{cl}	–
Closest approach distance (km)	–

Data Used Time Distribution	
Fields	*Values*
Altimetric data acquisition initial time t_{i}	$2007-05-12T19:19:28.000$ (232269560.2353)
Altimetric data acquisition final time t_{f}	$2007-05-12T20:11:28.000$ (232272689.5253)
Number of observations	2925
Time gap (hh mm ss)	$0^{\text{h}}19^{\text{m}}8.683^{\text{s}}$
Altimetric data acquisition initial time t_{i}	$2007-05-12T20:30:40.000$ (232273838.2083)
Altimetric data acquisition final time t_{f}	$2007-04-26T21:04:48.000$ (232275889.9043)
Number of observations	514
Total number of altimetric observations used	**3439**

Titan flyby T36

The SBDR table of Titan's flyby T36 is not available in the PDS data system.

Titan Flyby T36	**02 Oct 2007**

Flyby Description	
Fields	*Values*
Flyby t_{start}	–
Flyby t_{end}	–
Flyby length (hh mm ss)	–
Time of closest approach t_{cl}	–
Closest approach distance (km)	–

Data Used Time Distribution	
Fields	*Values*
Altimetric data acquisition initial time t_{i}	$2007-10-02T03:50:08.000$ (244569006.3394)
Altimetric data acquisition final time t_{f}	$2007-10-02T04:22:24.000$ (244570936.2274)
Number of observations	753
Time gap (hh mm ss)	$0^{\text{h}}41^{\text{m}}40.084^{\text{s}}$
Altimetric data acquisition initial time t_{i}	$2007-10-02T05:04:00.000$ (244573436.3114)
Altimetric data acquisition final time t_{f}	$2007-10-02T05:36:48.000$ (244575405.0494)
Number of observations	1080
Total number of altimetric observations used	**1833**

Titan flyby T39

The SBDR table of Titan's flyby T39 is not available in the PDS data system.

Titan Flyby T39	**20 Dec 2007**
Flyby Description	
Fields	*Values*
Flyby t_{start}	–
Flyby t_{end}	–
Flyby length (hh mm ss)	–
Time of closest approach t_{cl}	–
Closest approach distance (km)	–
Data Used Time Distribution	
Fields	*Values*
Altimetric data acquisition initial time t_{i} Altimetric data acquisition final time t_{f} Number of observations	$2007-12-20T22:28:32.000$ (251461715.0316) $2007-12-20T22:38:56.000$ (251462335.1286) 148
Time gap (hh mm ss)	$0^{\text{h}}41^{\text{m}}11.020^{\text{s}}$
Altimetric data acquisition initial time t_{i} Altimetric data acquisition final time t_{f} Number of observations	$2007-12-20T23:20:00.000$ (251464806.1486) $2007-12-20T23:53:20.000$ (251466805.0286) 485
Total number of altimetric observations used	**633**

				Planned RADAR Titan Flyby Activities										
Flyby	rev	Seq.	Alt (km)	iRAD	iSCT	iALT	iLSAR	iHSAR	oHSAR	oLSAR	oALT	oSCT	oRAD	Flyby date
TaRA	a	S5	1174				✓	✓						10/26/2004
Ta				X	✓	X			✓	✓	✓	✓	✓	
T3	3	S8	1579	X	X	✓	✓	✓	✓	✓	✓	✓	X	2/15/2005
T7	14	S14	1075	X	X	✓	✓	✓	✓	✓	✓	X	✓	9/7/2005
T8	17	S15	1353	✓	✓	✓	✓	✓	✓	✓	✓	✓	✓	10/28/2005
T12	22	S19	1947	X	X		X	X	X	X	X	X	✓	3/19/2006
T13	23	S20	1855	X	X	X	✓	✓	✓	✓	✓	✓	✓	4/30/2006
T16	26	S22	950	✓	✓	✓	✓	✓	✓	✓	✓	X	X	7/22/2006
T17RA	28	S23	950	X	X	X	X	✓	✓	X	X	X	X	9/7/2006
T18RA	29	S23	950	X	X	X	X	✓	✓	X	X	X	X	9/23/2006
T19	30	S24	950	✓	✓	✓	✓	✓	✓	✓	✓	✓	✓	10/9/2006
T20 RADAR Option	31	S25	950	✓	✓	✓	✓	✓	✓	✓	✓	✓	X	10/25/2006
T21RA	35	S26	950				✓	✓						12/12/2006
T21				X	X	X			✓	✓	✓	✓	✓	
T23	37	S27	950	✓	✓	✓	✓	✓	✓	✓	✓	✓	✓	1/13/2007
T25	39	S28	950	✓	✓	✓	✓	✓	✓	✓	✓	✓	✓	2/22/2007
T28	42	S29	951	✓	✓	✓	✓	✓	✓	✓	✓	X	X	4/10/2007
T29	43	S29	950	X	✓	✓	✓	✓	✓	✓	✓	✓	✓	4/26/2007
T30	44	S30	950	✓	✓	✓	✓	✓	✓	✓	✓	✓	✓	5/12/2007
T36RA	50	S34	950					✓	✓					10/2/2007
T36				✓	✓	✓	X			X	✓	✓	✓	
T39	54	S36	950	✓	✓	✓	✓	✓			✓	✓	✓	12/20/2007
T39RA									✓	✓				
T41	59	S38	950	✓	✓	✓	✓	✓	✓	✓	✓	✓	X	2/22/2008
T43	67	S40	950	✓	✓	✓	✓	✓	✓	✓	✓	✓	X	5/12/2008
T44 RADAR Option	69	S40B	1348	X	✓	✓	✓	✓	✓	✓	✓	✓	✓	5/28/2008

Figure 5.14: Planned RADAR Titan flyby activities.

Chapter 6

Determination of the Orbit of Titan

6.1 Setup of the Orbit Determination process

SOSYA_ART's capability is the estimation of Titan's state at the batch epoch by the use of the altimetric measurements collected. The estimation process is repeated for each set of data we received and in this way we have an estimated state vector of the moon for each flyby. All the processes have their own setup files list as input and give the output files for each iteration. This chapter describes at first the input files needed by each simulation process and then provides a discussion of the results obtained for Titan's estimated states.

The input and output files general flow of SOSYA_ART are illustrated in Figure 6.1, where the main computing steps are given. The input files list includes the initial setup for the run, the kernel files needed for the computation of the Cassini state vector at the observation times, the altimetric data file and the parameters setup used by the integration and interpolation part of the run. The output files give the observation residuals values and their statistical information, Titan's state estimated vector and the correlation coefficients between its elements. Moreover, SOSYA_ART outputs the list of the rejected altimetric observations. All these files are written at every iteration in the Orbit Determination run.

As we explained in Chapter 5, the altimetric data we used consist of range-to-target values measured from the antenna's center of phase to Titan's surface. The ranges values have been computed considering Titan as a sphere of 2575 km radius which is adopted as the surface model in the development of the observation equation. Each range value is characterized by an identification number (`burst ID`) and by the emission time at which the electromagnetic beam leaves the spacecraft antenna. During the process of orbit determination, the emission times are corrected for light time as we illustrated in Section 5.2. Since the altimetric observation errors were not available, we have used a constant value for the weight of 80 m for all the observations. This value is less than the minimum resolution the instrument achieves because RADAR works better than predicted (the real error probably is one-third of the expected error). However, the altimetric module code is implemented in order to process data with different errors.

By means of the *Orbit Simulation* capability of SOSYA ([2]), the equations of motion have been numerically integrated starting at an epoch corresponding to few minutes before the first altimetric observation of the RADAR for each flyby. In the same way, the final epoch has been set a few minutes after the altimetric observation arc is completed. Thus, a new set of initial conditions at epoch were determined that we have used as initial conditions in the Orbit Determination process. The files containing the new initial conditions at epoch for all the natural satellites of the Saturnian System have been computed for each Titan encounter. The estimation epoch at which the batch filter algorithm gives Titan's state vectors can be read off Table 6.2 together with the estimated positions and velocities and the standard deviation values. The results in the table are discussed later in the chapter. Since the values of the accuracies of

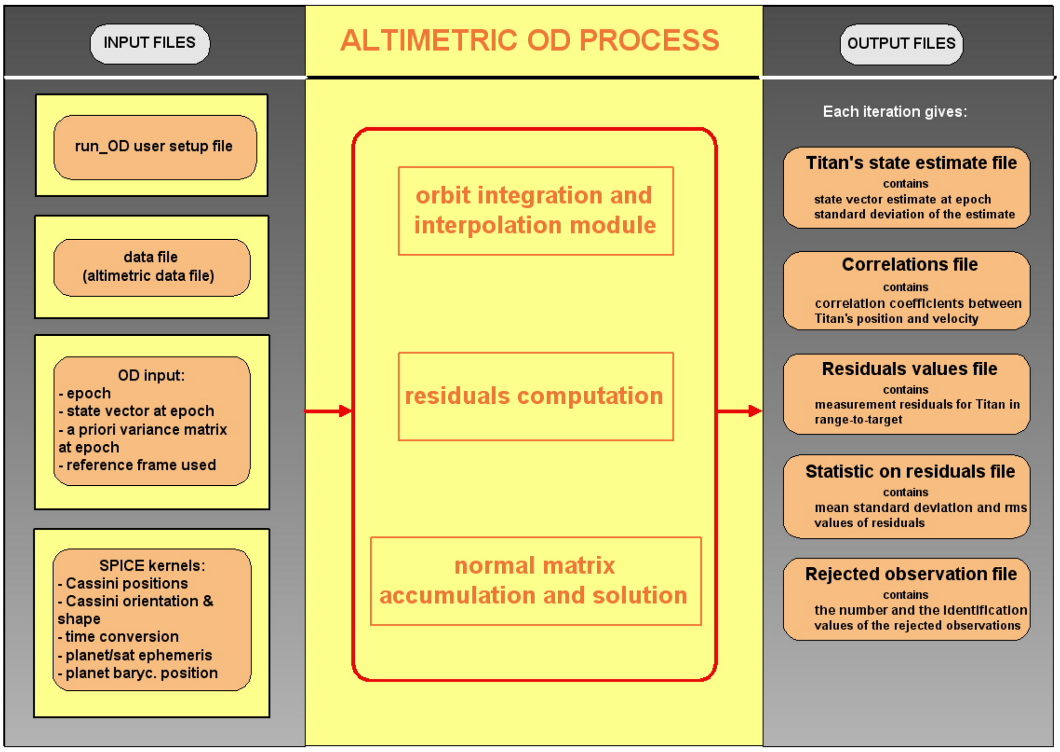

Figure 6.1: Input and output files list diagram of SOSYA_ART software.

the natural satellites ephemerides were not available, we do not have the possibility to use an a-priori variance matrix, $\bar{P}_0$, to better condition the estimation error covariance matrix, P, in the estimation process. So at first the Orbit Determination processes ran without the a priori variance matrix and then we used a variance of 9 km and 25 km for the positions and a variance of $9 \cdot 10^{-6}$ km/s and $25 \cdot 10^{-6}$ km/s for the velocities, respectively. With these choices for the solution procedure we wanted to prove that the standard deviation errors effectively decrease by the use of the a priori variance matrix.

The observation times at which Titan's state vector and its state transition matrix are interpolated are read directly from the files containing the altimetric data. The planetary ephemerides used in the simulation processes are the JPL Development Ephemeris DE405 and the satellites ephemerides have been obtained from the Cassini Radio Science Team of University "La Sapienza" in Rome. The file is specific for the Cassini spacecraft tour and we refer to it as SATXXX.

The computation of the altimetric distances makes use of Cassini's state vectors and attitude matrices, and use Titan's state vectors at the observation times. The first ones are read in from the SPICE-SPK/CK kernels containing spacecraft's orbit and attitude matrices, the second ones are given by the interpolation module implemented in SOSYA with the use of DIVA ([10]).

6.2 Orbit solution and discussion

In this section we present the results obtained by SOSYA_ART for the estimation of Titan's states at the batch epoch we fixed for each flyby by the means of the altimetric measurements collected. As it can be read from Figure 6.1, at each iteration, the software gives the computed residuals, the file containing the converged state vectors, the set of correlation coefficients and the rejected observations. Each of these files are ordered by the observation ID and the respective observation time.

Residuals

The residuals are the differences between the observed altimetric data at each observation time and the corresponding value computed using the observation model developed. If the model fit to the data is correct, the residuals approximate the random errors that make the relationship between the observed variables and the computed variable a statistical relationship.

first iteration	$\boldsymbol{h}$ (km)		
	mean	$\boldsymbol{\sigma}$	**rms**
Ta	15.977771	1.743615	16.072422
T3	-1.911673	0.129171	1.916017
T8	-2.328764	1.640540	2.847308
T13	-2.806186	0.129327	2.809154
T16	0.576560	1.333688	1.452287
T19	0.517462	2.792778	2.838807
T21	-4.447653	0.554961	4.482065
T23	3.290940	5.007163	5.989466
T25	3.503621	0.192917	3.508835
T28	-3.785247	0.432284	3.809831
T29	-3.590752	1.329476	3.828734
T30	-7.505698	2.914905	8.051689
T36	-0.380654	1.647358	1.690328
T39	-1.871269	3.259723	3.756415

last iteration	$\boldsymbol{h}$ (km)		
	mean	$\boldsymbol{\sigma}$	**rms**
Ta	-0.000031	0.065519	0.065435
T3	0.000007	0.047574	0.047489
T8	-0.000058	0.043685	0.043622
T13	-0.353466	0.306451	0.467440
T16	-0.000815	0.087654	0.087607
T19	-0.000326	0.101835	0.101777
T21	-0.000005	0.070569	0.070488
T23	-0.000460	0.091950	0.091899
T25	0.000000	0.027994	0.027738
T28	-0.000504	0.080050	0.080019
T29	-0.000598	0.114147	0.114089
T30	0.000138	0.068910	0.068898
T36	-0.001254	0.100706	0.100685
T39	-0.001249	0.108113	0.108031

Table 6.1: Altimetric observation residuals, means and standard deviations for the first iteration (on the left) and for the last iteration (on the right) for each flyby processed.

The plots of the residuals resulting from the pre-fit and post-fit iterations are shown at the and of the chapter in Figures 6.5, 6.6, 6.7, 6.8, 6.9, 6.10, 6.11, 6.12, 6.13, 6.14, 6.15, 6.16, 6.17, 6.18. The residuals appear to behave randomly in the most cases and this suggests that the model fits the data well. However, some post-fit plots show evidence of a non-random structure and this is a clear sign that either the model fits the data poorly, or the software needs some refinements in the simulation procedure implemented. The cases that need to be investigated in depth are flybys T13, T30 and T36.

In details, T13 has a parabolic post-fit residuals plot (Figure 6.8): this means that during the estimation process the filter doesn't change the state in the right way giving residuals values with a sort of noise signal and further investigations are needed. Anyway we observed that the parabolic behavior vanish as we use the a-priori variance matrix $\bar{P}_0$ in the simulation run. The sinusoidal behavior of the post-fit residuals plot is shown especially by flybys T30 and T36 (Figures 6.16 and 6.17). The reason for this may be related to inaccuracy in the spacecraft attitude data.

The statistical information on observation residuals for the altimetric observations are provided in Tables 6.1: for each flyby data set we provide the values of the residuals rms, the mean and the standard deviation of the pre-fit (left panel) and post-fit (right panel) iterations.

Titan's flybys T25 and T13 have the lowest number of observations and thus their residuals statistics are only listed here and excluded from the results summary. In fact, as it can be noticed from Table 6.1, the mean of the residuals in the last iteration for flyby T25 is practically null because the number of observations is only 57. On the other hand, the residuals mean of T13 is far from zero if compared with the other values. This could be another reason to explain the parabolic behavior shown by its post-fit residuals: there could be a bias in the altimetric measurements taken during flyby T13. Moreover, the standard deviation of T13 increases from the first to the last iteration instead of decreasing as all the other standard deviation values. This is a sign that the solution found is likely not acceptable, although during the last iteration the software has certainly discarded the outliers measurement residuals when trying to compute the best solution for the state. The source of the bias or the incorrect data processing for this case needs more investigation.

The mean of all the other flybys is approximately zero and it is clearly less than the measurement error (assumed as 80 m). For this reason we neglected the implementation of the bias estimation in the SOSYA_ART software module. The global mean of residuals at the first iteration is -340 m and it decreases to the global mean at the last iteration of $-4.296 \cdot 10^{-4}$ km. In the post-fit cases the values of the residuals mean range from a minimum mean value of -1.3 m (T36) to a maximum value of 0.14 m (T30). The mean of all the rms values at first iteration is 4.703 km and it decreases to the value of 81.67 m at last iteration. The difference between the values of the mean of the rms computed for the first and the last iterations underlines the goodness of the solutions for Titan state estimations obtained with respect the initial ones. In the post-fit cases the value of the rms ranges between 43.62 m (T8) and 114.08 m (T29) while in the pre-fit case it ranges between 1.452 km (T16) and 16.072 km (Ta).

Converged Titan's state vectors

The batch algorithm accumulates the entire set of data in the normal matrix prior to solving for the best Titan state estimate. To invert the normal equations and fit the data we have applied a Cholesky decomposition. We have verified that the covariance matrix was positive definite. The solution converges in few iterations to the best estimate of Titan's state at epoch. The number of iterations for each flyby is shown in Table 6.3 or in the residuals plots in Figures 6.5-6.18. Table 6.2 contains Titan's converged state vectors together with the standard deviation representing an assessment of the state uncertainty. The minimum value of standard deviation of the estimated position is 293.9 m which is the z-component of the vector computed for flyby T29. The maximum value is 5.2328 km which is the z-component of the vector computed for flyby Ta. The standard deviation of the velocity ranges from a minimum of $6.322 \cdot 10^{-2}$ m/s (v_z-component computed with T29) to a maximum value of 7.2 m/s (v_z-component computed with Ta). As explained in the previous section, Titan flybys T13 and T25 have been processed, but they are not discussed with the other results because they have very few observations (Table 5.1) and this can be noticed in the high standard deviation values of the respective estimated state vector.

The standard deviation values of the position and velocity vectors obtained without using the a priori variance matrix, $\bar{P}_0$, are displayed in Figure 6.2: all the values are below 6 km in the case of the position and below $8 \cdot 10^{-3}$ in the case of the velocity values (T13 and T25 are not included). The results are satisfactory if they are compared to the ones obtained by Jacobson [8]. Using astrometric observations, radiometric tracking and spacecraft imaging data, Jacobson developed new ephemerides for the major Saturnian satellites. The 1-σ uncertainties in the directions along the orbit radius (R), along the orbit track (T) and normal (N) to the orbit plane range between 10 km (Enceladus R-component) and 1600 km (Calypso T-component). The uncertainties in Titan's state are 40 km along R, 150 km along T and 50 km along N.

The estimation process used in this research yields good results because the altimetric data are very accurate observations. Obviously we should keep in mind that in this work we estimate only Titan's state on short orbital arcs and so we are treating a sort of particular and local solution for each flyby with respect the solution obtained by Jacobson. The orbital arc duration, over which the measurements are collected, is typically about 15 minutes (with some exceptions of about 30 minutes) making the present solutions extremely local. In order to obtain a global solution over the entire Cassini tour, a multi-arc approach would be required.

The accuracy of our solution is limited by the altimetric measurement errors and by the a priori covariance matrix values applied to the initial conditions of the natural bodies integrated. $\bar{P}_0$ is generally not a very realistic representation of the accuracy of the a priori estimates. However, it is used here as a constraint to better condition the estimation error covariance matrix P. Figures 6.3 and 6.4 show that using the a-priori variance matrix the state's estimation improves and the standard deviation values decrease. In the case of a variance of 25 km and $25 \cdot 10^{-6}$ km/s for the position and velocity respectively the standard deviation ranges between 0.10072 km and 3.618 km for the position, and between $3.0108 \cdot 10^{-3}$ km/s end $6.3149 \cdot 10^{-5}$ km/s for the velocity (Figure 6.3). When the variance is 9 km and $9 \cdot 10^{-6}$ km/s respectively for the position and the velocity, the standard deviation ranges from 0.147 km to 2.371 km for the position, and from $2.3071 \cdot 10^{-3}$ km/s to $6.3024 \cdot 10^{-5}$ km/s for the velocity (Figure 6.4).

As we stated in the description of the observation model adopted (Section 4.5), the values of the

		position (km)		**velocity** (km/s)	
		value	$\boldsymbol{\sigma}$	**value**	$\boldsymbol{\sigma}$
Ta	x	90790.525887122727	2.9440	5.5819055604179333	4.7752E-03
2004 oct 26 15:40:00.0000 TDB	y	-1199096.8702990653	2.2010	0.5287902415603646	2.8570E-03
	z	72683.696103072813	5.2328	-0.5211272691898859	7.2062E-03
T3	x	87274.251869283093	1.7017	5.6038494837426098	9.1069E-04
2005 feb 15 06:20:00.0000 TDB	y	-1199526.7118605727	1.3677	0.5216955983513399	4.8789E-04
	z	73048.913198629612	2.3527	-0.5236462589797357	1.5680E-03
T8	x	-28411.947114015828	1.1801	5.6098905160979378	4.4396E-04
2005 oct 28 03:40:00.0000 TDB	y	-1204874.3297385797	0.3972	-0.0170421344191247	2.1091E-04
	z	83697.084967720904	4.9703	-0.4973570222043116	1.2787E-03
T13	x	-697190.40329855599	2.0621	-4.5393541600028380	7.8958E-03
2006 apr 30 21:00:00.0000 TDB	y	1037998.2779941373	6.9895	-2.9371701979330251	1.4919E-03
	z	-8581.1580313269133	48.7006	0.6410486250934060	2.3702E-02
T16	x	-1244986.6941283541	0.4764	-0.4521965877121465	1.8484E-04
2006 jul 21 23:20:00.0000 TDB	y	122907.95779253976	1.3644	-5.3852336263923322	5.3568E-04
	z	101553.09322396258	0.8267	0.4034803557739413	2.1801E-04
T19	x	-1244831.8356550639	0.3109	-0.4618691366535072	8.8171E-05
2006 oct 09 16:40:00.0000 TDB	y	125123.60402943045	0.9021	-5.3833573101367449	2.2372E-04
	z	101398.18302370311	0.3797	0.4054949744917004	1.1006E-04
T21	x	-1245733.3951738123	2.0727	-0.4211978077103663	1.5185E-03
2006 dec 12 12:00:00.0000 TDB	y	113963.34775349268	1.0784	-5.3844918197851150	9.3881E-04
	z	102235.55166288861	1.2812	0.3972387688240128	8.1909E-04
T23	x	-1242739.6849992662	2.4655	-0.5644528869519235	5.3211E-04
2007 jan 13 07:40:00.0000 TDB	y	147202.40915197050	1.9947	-5.4109008357353741	4.4343E-04
	z	99781.250334802389	0.7342	0.3890415401640619	4.3928E-04
T25	x	1175875.9729624467	112.559	0.7098084782556775	1.3299E-01
2007 feb 22 02:40:00.0000 TDB	y	-136831.39986573055	120.804	5.7435019151753206	1.5676E-01
	z	-94559.060560886181	31.840	-0.4072782136239315	4.0374E-02
T28	x	1173990.1626205295	0.5716	0.7413754756430268	2.7392E-04
2007 apr 10 22:00:00.0000 TDB	y	-151952.98153080599	0.6755	5.6647203933513897	3.0138E-04
	z	-93337.905377521194	0.5860	-0.4489225463615419	1.3532E-04
T29	x	1173926.1655281514	0.5185	0.7430029997321714	1.1979E-04
2007 apr 26 20:40:00.0000 TDB	y	-152491.00758121791	0.7035	5.6658372592139417	1.5045E-04
	z	-93306.390496484630	0.2239	-0.4472932586492427	6.3220E-05
T30	x	1172953.8982665027	0.6993	0.7785458663755382	1.5180E-04
2007 may 12 19:00:00.0000 TDB	y	-159771.73128275471	0.9781	5.6561877983858251	2.0972E-04
	z	-92669.078982320018	0.3171	-0.4627073555797382	6.9744E-05
T36	x	970318.12994343333	0.5514	3.2363470236583027	1.0389E-04
2007 oct 02 03:40:00.0000 TDB	y	-683158.18994310603	0.3833	4.6939375904908234	7.0512E-05
	z	-39493.444615246422	0.4377	-0.6021358192517183	8.7647E-05
T39	x	984147.20423707645	1.8673	3.1401328309200665	4.2020E-04
2007 dec 20 22:20:00.0000 TDB	y	-662675.71488640446	0.9225	4.7591812181829836	2.0345E-04
	z	-42080.310902837278	0.4358	-0.5993228227933789	1.8223E-04

Table 6.2: Solved-for barycentric satellite state vectors at the TDB epoch time written in the first column. The altimetric data have been processed without adding the offset delay but corrected for light time. A priori covariance matrix is not used in these simulation processes.

standard deviation of the states show that the estimation process is not sufficiently sensitive for the assumption of a different shape from the sphere for Titan's surface.

Correlations

Table 6.3 gives the complete set of correlation coefficients between the various components of Titan's dynamical state components at the flyby epochs. In the table there are some terms that show a strong correlation between the position and velocity components in every flyby. This is probably due to the approximate conservation of the angular momentum for the satellite over the short orbital arcs considered. For example, all the components of the state vector in the case of Ta are strongly correlated and in

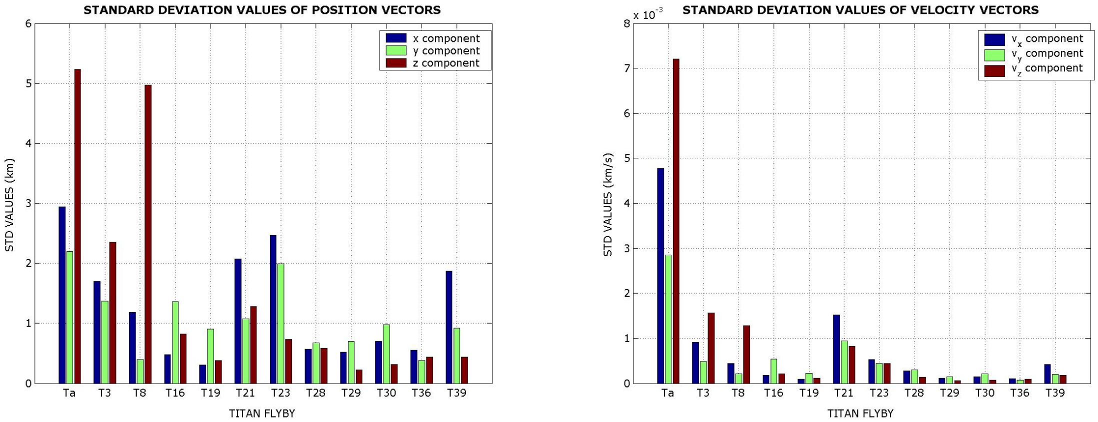

Figure 6.2: Standard deviations of the position vectors and velocity vectors without using the a priori variance. Resulting values of Titan's flybys T13 and T25 are not included in these graphics.

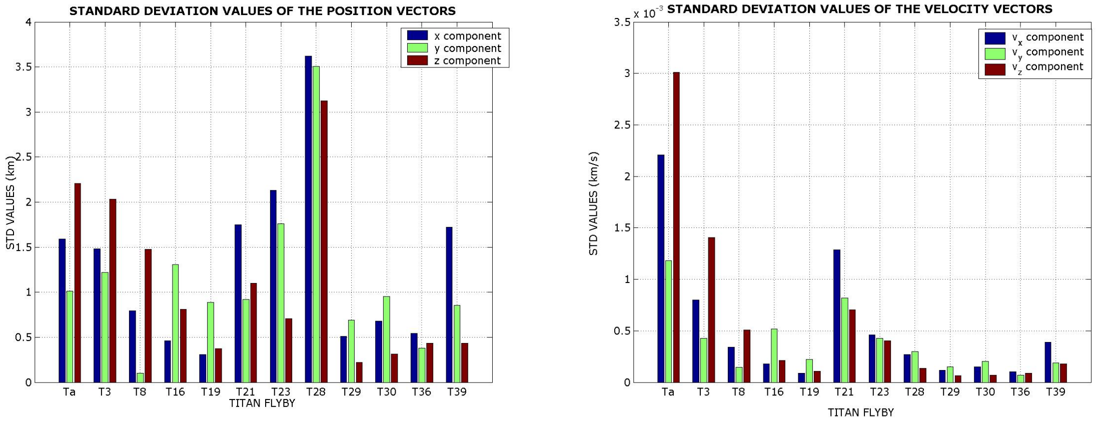

Figure 6.3: Standard deviations of the position vectors and velocity vectors using an a priori variance of 25 km in the position position and of $25 \cdot 10^{-6}$ km/s in the velocity vector. Resulting values of Titan's flybys T13 and T25 are not included in these graphics.

fact the altimetric data processed are collected over only 10 minutes. The strong correlation between the same position and velocity components (position-position and velocity-velocity) is due to the scalar nature of the altimetric measurement although the observation model is obviously vectorial. For this reason, different possible Titan state configurations yield the same altimetric measurement value, but the dynamics of the system is not compatible with the existence of all of them. On the other hand, the equations of motion can't reduce the number of configurations sufficiently to give an estimate as accurate as the altimetric data because of the short orbital arcs used in the inversion process. If the orbital arc of the flyby were longer and the number of observations greater, then the estimation of Titan's state would be more accurate as can be noticed from Tables 6.1 and 6.2. In this case too, the multi-arc technique would be the appropriate approach to adopt for the estimation problem solution.

Rejected observations

The rejection level is computed after the first iteration and it is set to be 3 times the weighted rms of the previous iteration (99.73% of the residuals values are within 3 standard deviations). Using the

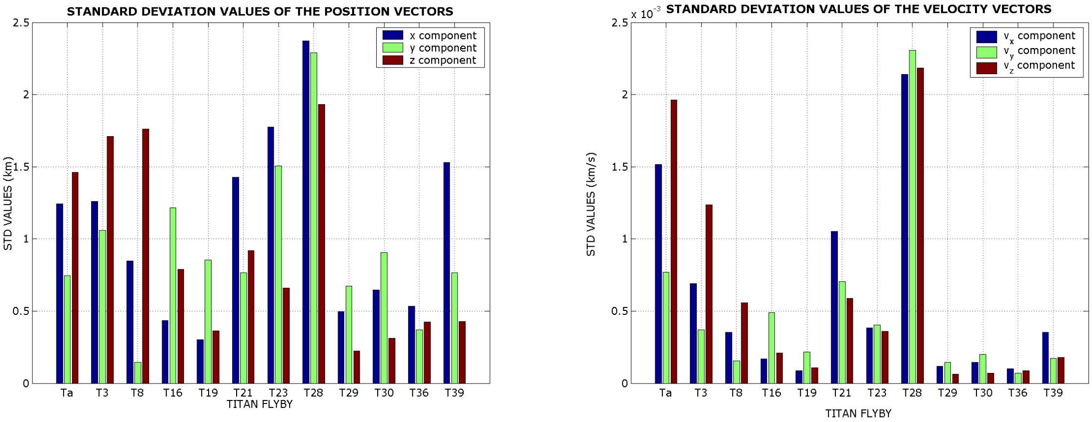

Figure 6.4: Standard deviations of the position vectors and velocity vectors using an a priori variance of 9 km in the position position and of $9 \cdot 10^{-6}$ km/s in the velocity vector. Resulting values of Titan's flybys T13 and T25 are not included in these graphics.

rejection subroutine, SOSYA_ART neglects residuals that stand out from the basic random pattern of residuals (no outliers) so it rejects bad observations from the set of data during the reduction run. At each iteration the software can re-process the observations that were previously discarded, if their current rms value become less than the current rejection level. The rejection level changes at each iteration because the weighted rms also changes. Table 6.4 gives for each flyby the number of the observations rejected for each iteration and the total number of observations used in the last iteration.

		x	y	z	v_x	v_y	v_z
Ta iter 21	x	**1.00**	0.853	-0.934	-0.901	-0.894	0.933
	y		**1.00**	-0.981	-0.978	-0.976	0.946
	z			**1.00**	0.979	0.984	-0.980
	v_x				**1.00**	0.989	-0.975
	v_y					**1.00**	-0.991
	v_z						**1.00**
T3 iter 8	x	**1.00**	0.982	-0.614	-0.892	-0.895	0.428
	y		**1.00**	-0.452	-0.870	-0.874	0.304
	z			**1.00**	0.560	0.562	-0.733
	v_x				**1.00**	0.999	-0.698
	v_y					**1.00**	-0.695
	v_z						**1.00**
T8 iter 12	x	**1.00**	0.811	0.536	-0.983	-0.986	-0.545
	y		**1.00**	0.928	-0.708	-0.791	-0.903
	z			**1.00**	-0.396	-0.512	-0.957
	v_x				**1.00**	0.988	0.438
	v_y					**1.00**	0.563
	v_z						**1.00**
T13 iter 12	x	**1.00**	-0.084	0.969	-0.416	-0.738	-0.986
	y		**1.00**	0.104	0.941	0.734	0.159
	z			**1.00**	-0.233	-0.588	-0.965
	v_x				**1.00**	0.920	0.480
	v_y					**1.00**	0.778
	v_z						**1.00**
T16 iter 6	x	**1.00**	-0.846	0.326	-0.835	0.761	-0.348
	y		**1.00**	0.228	0.853	-0.885	-0.203
	z			**1.00**	-0.014	-0.178	-0.997
	v_x				**1.00**	-0.981	0.072
	v_y					**1.00**	0.121
	v_z						**1.00**
T19 iter 8	x	**1.00**	-0.777	-0.345	-0.787	0.679	0.197
	y		**1.00**	0.859	0.492	-0.814	-0.745
	z			**1.00**	0.091	-0.660	-0.951
	v_x				**1.00**	-0.785	-0.131
	v_y					**1.00**	0.716
	v_z						**1.00**
T21 iter 6	x	**1.00**	-0.986	0.919	-0.960	0.842	-0.949
	y		**1.00**	-0.840	0.931	-0.762	0.954
	z			**1.00**	-0.923	0.952	-0.817
	v_x				**1.00**	-0.920	0.956
	v_y					**1.00**	-0.767
	v_z						**1.00**

		x	y	z	v_x	v_y	v_z
T23 iter 7	x	**1.00**	-0.723	0.245	-0.996	-0.241	-0.843
	y		**1.00**	0.492	0.726	-0.442	0.255
	z			**1.00**	-0.237	-0.924	-0.704
	v_x				**1.00**	0.200	0.822
	v_y					**1.00**	0.722
	v_z						**1.00**
T25 iter 9	x	**1.00**	0.965	0.296	-0.999	-0.980	-0.739
	y		**1.00**	0.537	-0.965	-0.996	-0.889
	z			**1.00**	-0.298	-0.475	-0.858
	v_x				**1.00**	0.982	0.740
	v_y					**1.00**	0.855
	v_z						**1.00**
T28 iter 9	x	**1.00**	0.783	-0.393	-0.906	-0.829	0.226
	y		**1.00**	0.265	-0.572	-0.771	-0.398
	z			**1.00**	0.558	0.145	-0.937
	v_x				**1.00**	0.897	-0.296
	v_y					**1.00**	0.157
	v_z						**1.00**
T29 iter 7	x	**1.00**	0.987	0.048	-0.893	-0.863	0.124
	y		**1.00**	0.205	-0.856	-0.875	-0.031
	z			**1.00**	0.116	-0.185	-0.963
	v_x				**1.00**	0.951	-0.185
	v_y					**1.00**	0.128
	v_z						**1.00**
T30 iter 15	x	**1.00**	0.995	0.374	-0.835	-0.848	-0.329
	y		**1.00**	0.463	-0.816	-0.846	-0.419
	z			**1.00**	-0.173	-0.338	-0.988
	v_x				**1.00**	0.985	0.213
	v_y					**1.00**	0.378
	v_z						**1.00**
T36 iter 11	x	**1.00**	0.997	0.864	-0.880	-0.877	-0.785
	y		**1.00**	0.897	-0.870	-0.867	-0.821
	z			**1.00**	-0.696	-0.691	-0.954
	v_x				**1.00**	1.000	0.751
	v_y					**1.00**	0.746
	v_z						**1.00**
T39 iter 9	x	**1.00**	0.948	0.023	-0.953	-0.901	0.149
	y		**1.00**	0.339	-0.881	-0.948	-0.172
	z			**1.00**	0.050	-0.314	-0.983
	v_x				**1.00**	0.932	-0.199
	v_y					**1.00**	0.171
	v_z						**1.00**

Table 6.3: Correlation coefficients of the last iteration for each flyby.

iter number →	1	2	3	4	5	6	7	8	9	10	11	12	13	14	15	16	17	18	19	20	21	total obs.	obs. last iter
Ta	0	0	0	4	9	14	18	22	27	31	37	41	47	52	57	60	64	69	70	71	71	459	388
T3	0	0	2	6	9	10	11	11	-	-	-	-	-	-	-	-	-	-	-	-	-	291	280
T8	0	1	165	165	3	1	1	9	15	16	17	17	-	-	-	-	-	-	-	-	-	349	366
T13	0	0	10	29	1	0	0	0	0	0	0	0	-	-	-	-	-	-	-	-	-	268	268
T16	0	0	8	11	12	12	-	-	-	-	-	-	-	-	-	-	-	-	-	-	-	886	874
T19	0	0	16	28	36	41	43	43	-	-	-	-	-	-	-	-	-	-	-	-	-	911	869
T21	0	0	4	5	6	6	-	-	-	-	-	-	-	-	-	-	-	-	-	-	-	444	438
T23	0	0	0	0	6	7	7	-	-	-	-	-	-	-	-	-	-	-	-	-	-	887	880
T25	0	0	1	1	1	2	2	2	2	-	-	-	-	-	-	-	-	-	-	-	-	57	55
T28	0	0	17	31	37	40	43	45	-	-	-	-	-	-	-	-	-	-	-	-	-	1248	1203
T29	0	0	4	15	20	21	21	-	-	-	-	-	-	-	-	-	-	-	-	-	-	982	961
T30	0	0	60	113	178	244	299	375	429	458	471	480	482	483	483	-	-	-	-	-	-	3439	2956
T36	0	7	17	25	39	51	59	62	67	68	68	-	-	-	-	-	-	-	-	-	-	1833	1765
T39	0	0	11	19	22	25	27	28	28	-	-	-	-	-	-	-	-	-	-	-	-	633	605

Table 6.4: Rejected altimetric observations for each flyby and for each iteration.

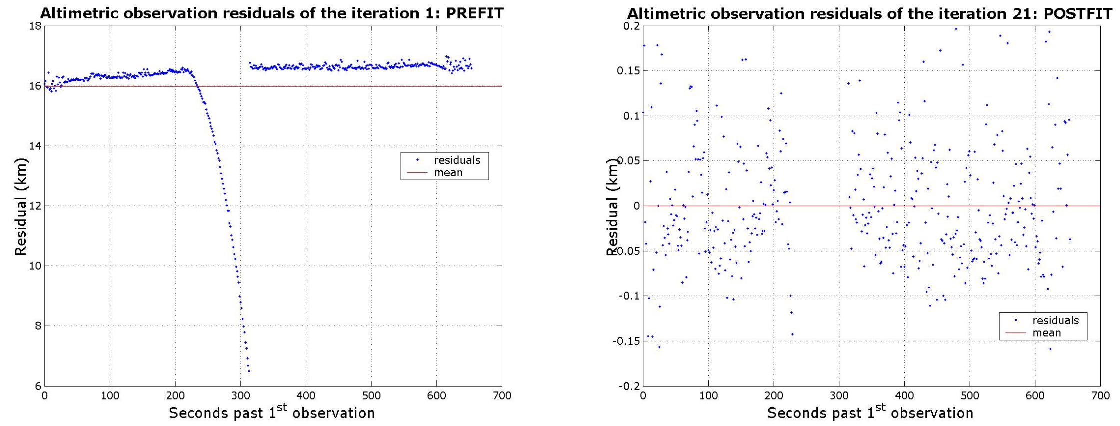

Figure 6.5: Flyby Ta: prefit and postfit altimetric measurements residuals.

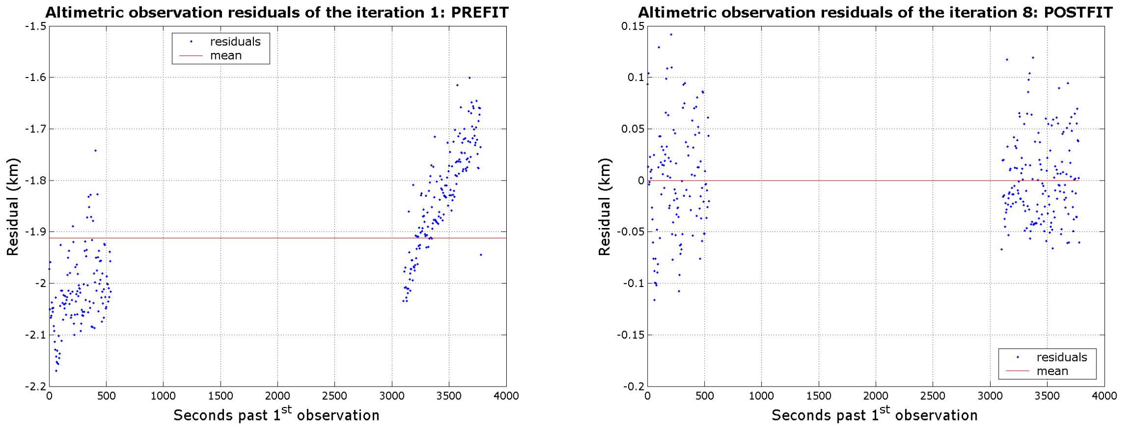

Figure 6.6: Flyby T3: prefit and postfit altimetric measurements residuals.

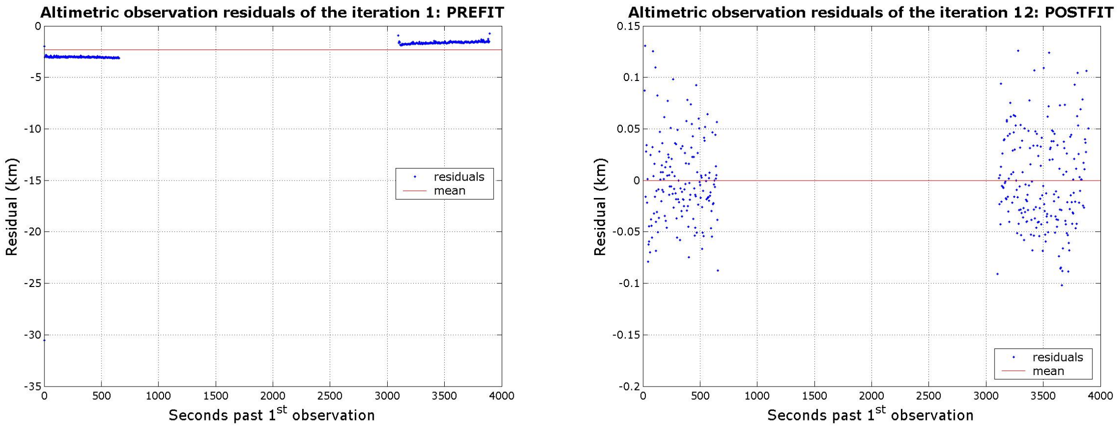

Figure 6.7: Flyby T8: prefit and postfit altimetric measurements residuals.

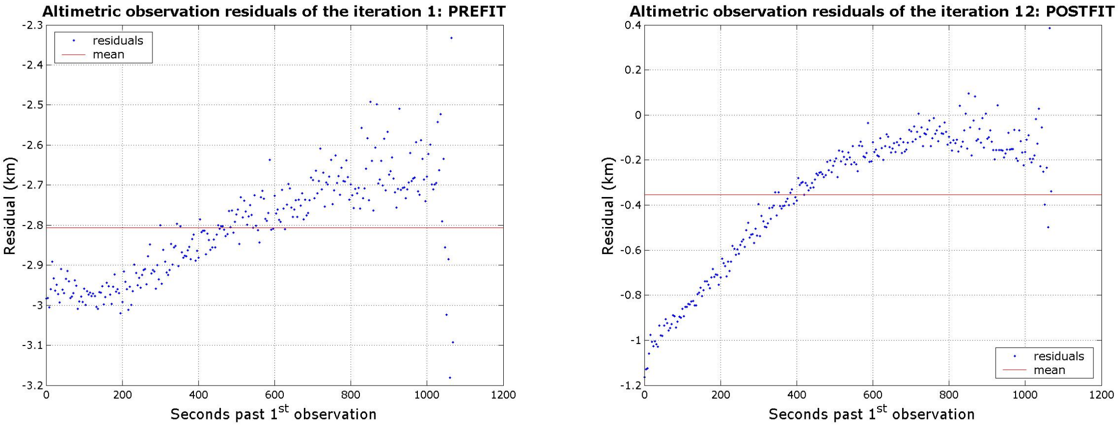

Figure 6.8: Flyby T13: prefit and postfit altimetric measurements residuals.

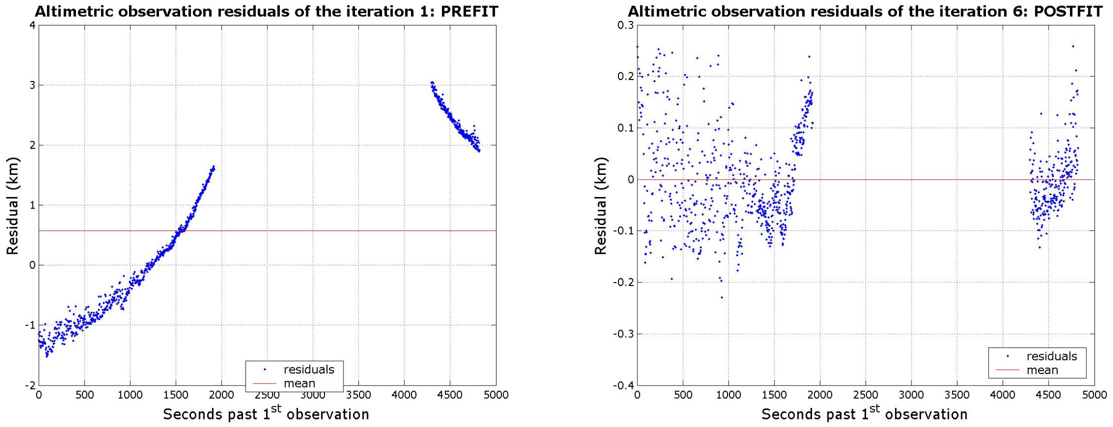

Figure 6.9: Flyby T16: prefit and postfit altimetric measurements residuals.

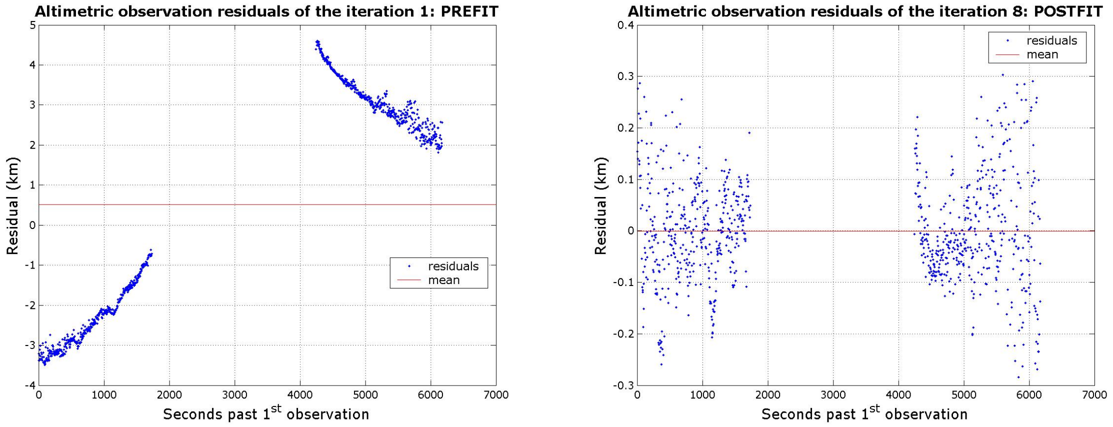

Figure 6.10: Flyby T19: prefit and postfit altimetric measurements residuals.

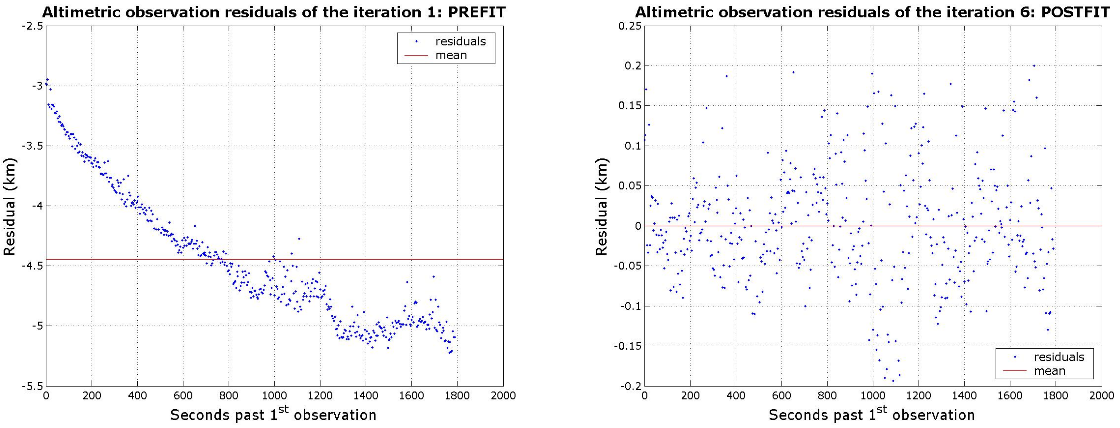

Figure 6.11: Flyby T21: prefit and postfit altimetric measurements residuals.

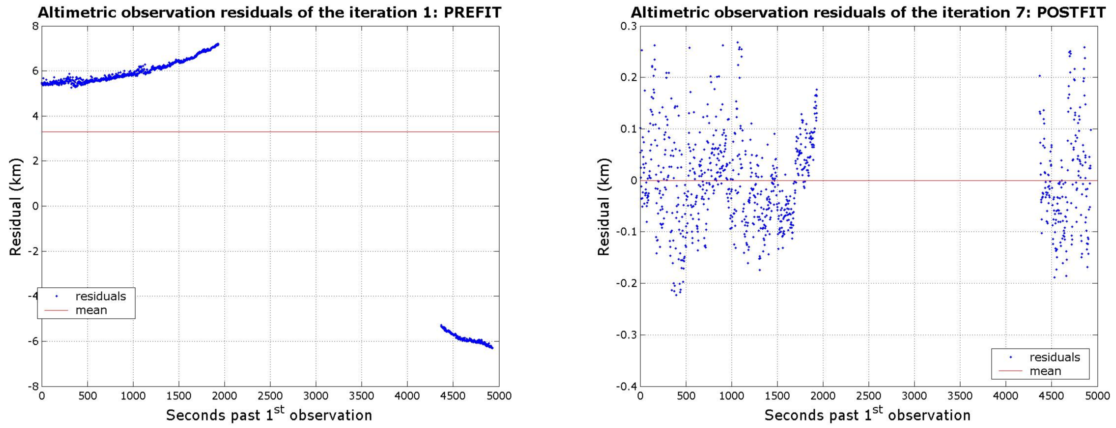

Figure 6.12: Flyby T23: prefit and postfit altimetric measurements residuals.

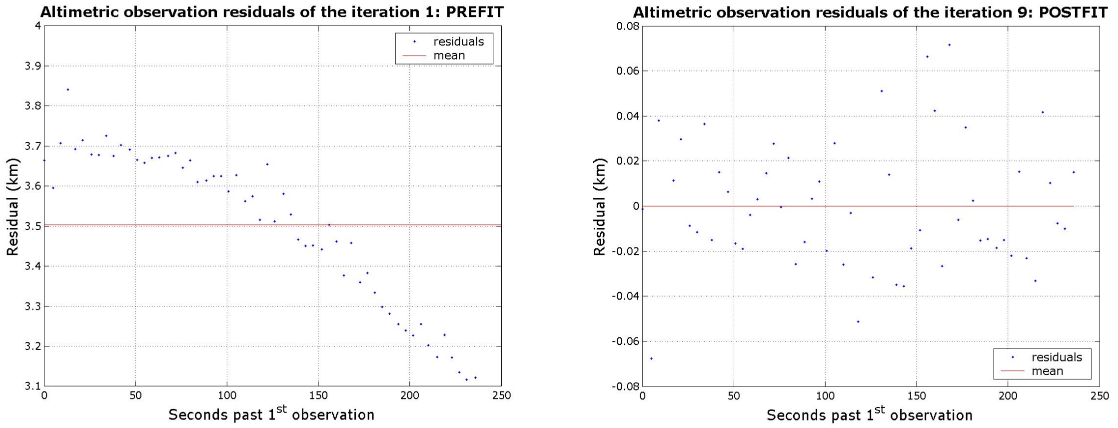

Figure 6.13: Flyby T25: prefit and postfit altimetric measurements residuals.

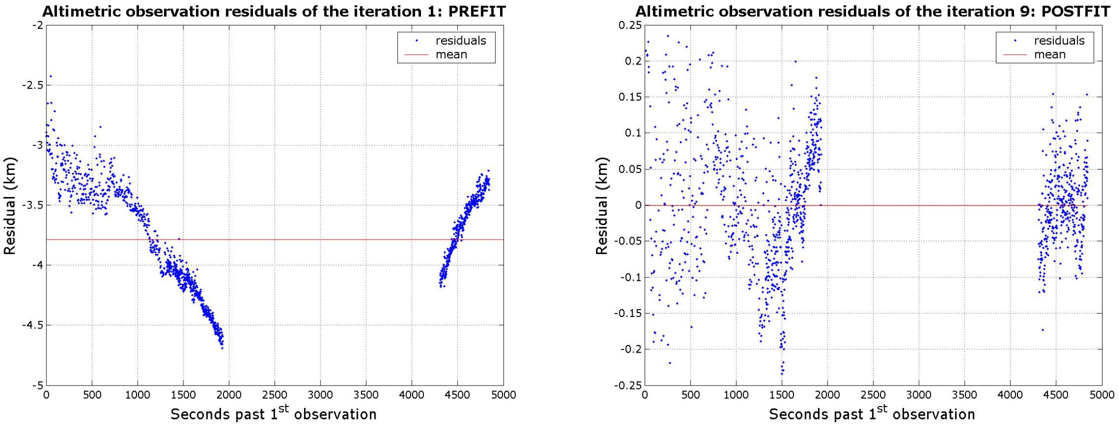

Figure 6.14: Flyby T28: prefit and postfit altimetric measurements residuals.

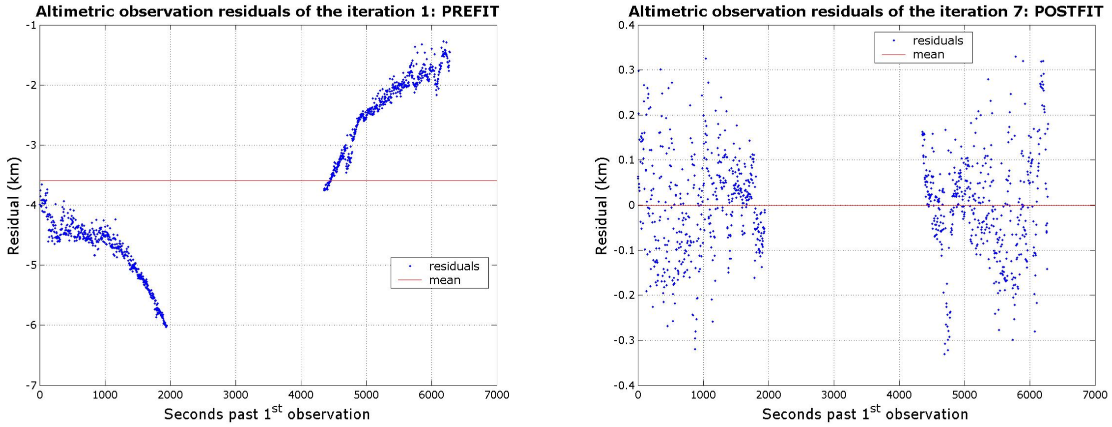

Figure 6.15: Flyby T29: prefit and postfit altimetric measurements residuals.

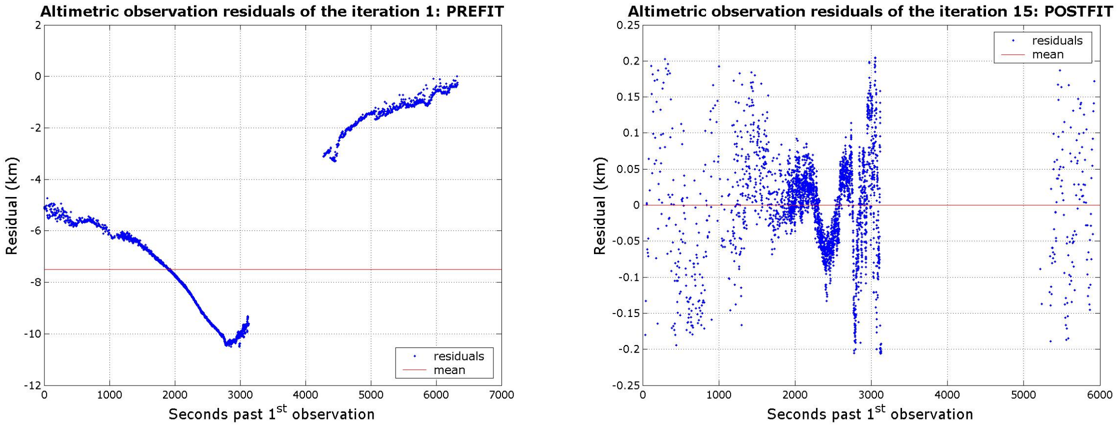

Figure 6.16: Flyby T30: prefit and postfit altimetric measurements residuals.

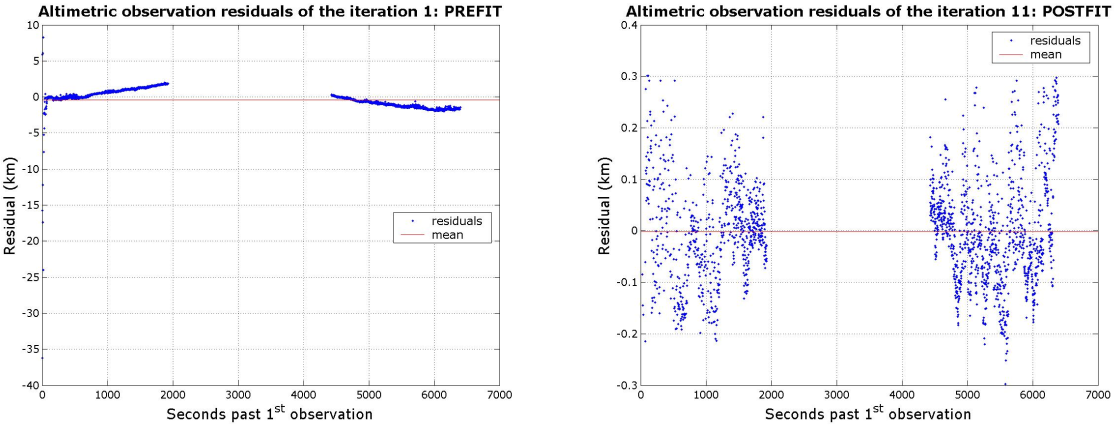

Figure 6.17: Flyby T36: prefit and postfit altimetric measurements residuals.

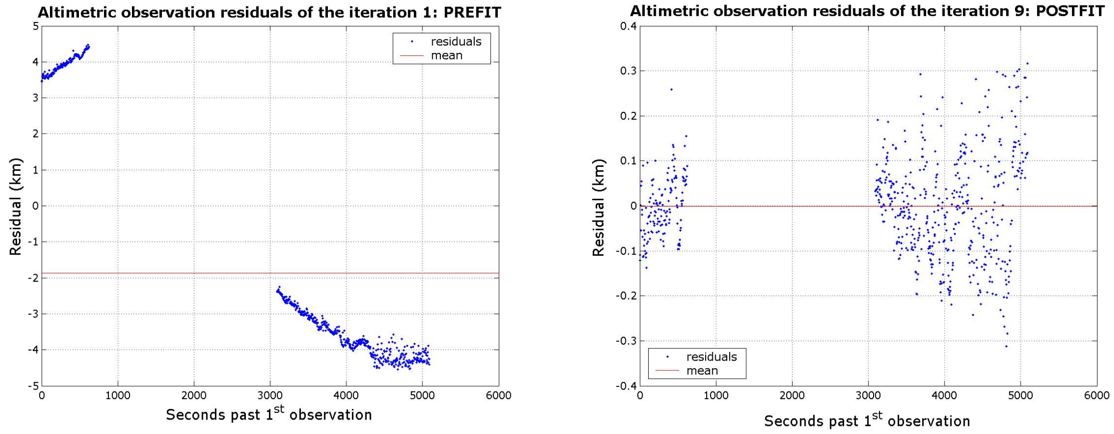

Figure 6.18: Flyby T39: prefit and postfit altimetric measurements residuals.

Chapter 7

Conclusion and Future Work

The research presented in this thesis has dealt with Titan's orbit determination through the use of the altimetric observations performed by Cassini's RADAR instrument during the flybys with the Saturnian moon. The main purpose of this work has been realized in the development and implementation of an additional module of the SOSYA (SOlar SYstem Astrometry) software tool. This new module has been named SOSYA_ART (SOSYA_Altimetric Run Tool and performs orbit determination based on an altimeter data type. Like the main software tool, SOSYA_ART is coded in Fortran95 following an object-oriented programming methodology allowing for safer programming and simpler code extension. Moreover, the Measurement Simulation capability of SOSYA (Appendix B) has been enriched by the introduction of a software module in the code that generates synthetic altimeter data, given the observer and the target trajectories and the instrument specification (Appendix A). The altimetric data simulation module uses SPICE-based subroutines and it is coded in Fortran95 as well. The module can be improved by the introduction of the possibility of adding noise to the signal.

The dynamical model of the Saturnian system adopted in the in the SOSYA software is fully described in [2]. SOSYA numerically integrates the equations of motion and the associated variational equations for the main natural satellites of Saturn in a reference frame centered in the barycenter of the Saturnian system. The geometrical model of the altimetric observations is developed and implemented in the same reference frame.

In total, 14 altimeter data arcs have been processed, but Titan's flybys T13 and T25 were discarded because the number of observations collected were insufficient to glean statistical information. The data coming from the last flybys scheduled during the nominal mission will be processed as soon as they will be made available, as well as those planned for the extended mission. The altimetric observations have been processed with a constant weight of 80 m, approximatively corresponding to the better resolution achieved by the instrument.

The precision associated with the estimated Titan dynamical state compares well, for example, with the the solution obtained by Jacobson [8], with uncertainties of 40 km along R, 150 km along T and 50 km along N. Without using the a priori variance matrix in the simulation processes, we obtained standard deviation values that range between 294 m and 5.233 km for the position vectors, and between $6.3 \cdot 10^{-2}$ m/s and 7.2 m/s for the velocity vectors. The altimetric data are very accurate measurements. Since we estimated only Titan's state on short orbital arcs, the estimated states represent very local solutions with respect the long arc solution obtained by Jacobson. In order to compute a global solution spanning the entire tour or any sizable portion of it, a multi-arc approach would be indicated. This technique would yield a more accurate estimation of Titan's ephemeris.

The altimetric measurement residuals rms improves from a minimum value of 1.365 km (T16) to a maximum value of 16.007 km (Ta) from the first to the last iteration underlining the goodness of the solutions for Titan's state obtained with respect the initial ones. Considering all the flybys, except T13 and T25, the rms obtained from their last iteration ranges from 43.6 m to 114 m. The residuals mean is between -0.005 m (T21) and -1.254 m (T36) which is clearly less than the assumed measurement weight (80 m). This justifies neglecting bias estimation in the data reduction process.

The parabolic shape of the post-fit residuals of flyby T13 and some sinusoidal behavior in other residuals plots point to the need for further investigation.

Introduction of an a-priori variance, $\bar{P}_0$, causes the values of the standard deviations to improve: the minimum value for the position vectors decreases to 147 m and the minimum value for the velocity vectors decreases to $6.3024 \cdot 10^{-2}$ m/s. This results are obtained using variance values of 3 km and $3 \cdot 10^{-3}$ km/s in Titan's position and velocity respectively. With the a-priori variance the parabolic behavior of the T13 post-fit plot disappears.

The altimetric module developed here can be tested on other mission scenarios with altimetric observations made by radar or laser instruments on board the spacecraft observing the surface of the target body during a flyby. The result is the improvement of the orbit of the celestial body observed, if the orbit of the observing spacecraft is already known with high accuracy.

SOSYA_ART will be enriched by a consider covariance analysis module that will allow the assessment of the effects of uncertainties in system model parameters on the estimated state vector.

The altimetric Orbit Determination capability of SOSYA_ART has enabled the determination of Titan dynamical states during several short arcs of the Cassini nominal mission. They provide virtual observations with an accuracy below 100 m that may be used together with other, more conventional observations of this body, in an attempt to determine an improved ephemeris for this largest moon of Saturn.

Appendix A

Altimetric Data Simulation

One of the purpose of SOSYA [2] is the Measurements Simulation and in this appendix we give the functional description of the module that implements the altimetric data simulation process. The software procedure uses SPICE-based subroutines and it is coded in Fortran95 as the entire software. The module computes the intersection points of the boresight ray of the Cassini RADAR science instrument with the surface of Titan at given observation times. Moreover, it computes the planetocentric latitudes and longitudes values of the intercept points.

A.1 The geometry of the problem

The geometry implemented to obtain the boresight intercept on the surface of Titan is illustrated in Fig. A.1. At a given observation time, the orientation of the spacecraft is computed with respect to the inertial frame and consequently the field of view of the observing instrument is known by the use of the SPICE kernels containing the instrument displacement and their observing direction. Then, the ephemeris kernels loaded give Titan's position at the observation time allowing in this way the intersection point coordinates computation. The altimetric values is the range-to-target value, or rather the distance between the spacecraft (corrected for the center of mass) and the point intersected on the surface. The transformation of the coordinates of this point from the inertial frame to the body-fixe frame gives the planetocentric coordinates expressed as longitude and latitude on the surface.

The user inputs required to specify the problem and solve it are:

- when: `times` (expressed as `TDB`), the module needs a file containing the observation times at which it computes the intersection points with the body's surface and the related ranges-to-target;
- on what object: `satnm (Titan)`, it is the name of the celestial body on which the altimetric observations are made;
- for what spacecraft: `scnm (Cassini)`, it is the name of the observing spacecraft;
- for which instrument: `instnm (cassini_radar_♯)`, it is the name of the instrument on board the spacecraft that observes the body's surface. The symbol ♯ means the radar beam number used in the data simulation process;
- model used: `spice_kernels.furnsh`, it consists of a file containing the kernels to be loaded by the process. The kernels needed in the case of Cassini mission are listed in the next section.

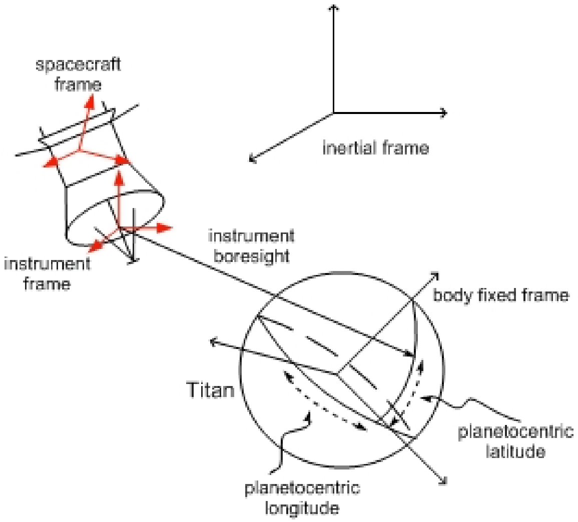

Figure A.1: Geometry and reference frames involved in the altimetric measurements simulation process.

A.2 SPICE Kernels needed

The values required to compute vectors, rotations and other parameters required to compute the altimetric range values are stored in the SPICE kernels listed, as an example, in table A.1. If kernels containing Cassini's ephemeris and attitude values at observation times are not available, they can be created using SPICE toolkit executable routines applied to the data fields contained in the SBDR tables. The data fields available to create the kernels needed to perform the computation are listed in the next section. The fields containing the spacecraft position and velocity in the J2000 coordinate system are used to produce the SPK kernel file for the orbit arc of interest. The fields containing the direction vectors of the axes of the space coordinate system and the angular velocity vector of the spacecraft are used to make the CK kernel file.

The easiest and most flexible way to make required kernels available to the program is via `FURNSH`. For the data simulation program we make a setup file (also called a "metakernel" or "furnsh kernel") containing the list of kernels to be loaded: `spice_kernels.furnsh`.

Parameter	Kernel Type	File name
time conversion	generic LSK Cassini SCLK	`naif0008.tls` `cassini.tsc`
satellite orientation	generic PCK	`pck00008.tpc`
satellite shape	generic PCK	`pck00008.tpc`
satellite position	planet/sat ephemeris SPK	`sat136.bsp`
planet barycenter position	planet SPK	`de405.bsp`
spacecraft position	spacecraft SPK	`Cassini_Feb_2005.bsp`*
spacecraft orientation	spacecraft CK	`Cassini.bc`*
instrument alignment	CASSINI FK	`cas_v39.tf`
instrument boresight	Instrument IK	`cas_radar_v11.ti`

Table A.1: Example of a list of SPICE kernels used by the program. * means that the kernel can be generated using the SBDR data fields.

A.3 Data fields used from SBDR

The altimetric measurements simulation module needs some data fields values contained in the SBDR tables and they are listed in table A.2. The active geometry time offset values are added to the ephemeris time values and this is a sort of correction for light time for the observation. The beam number and radar mode values are requested in order to know if the RADAR altimetric mode is operative at the observation time read in. The components of Cassini state vectors, attitude and angular velocity are needed when ephemeris and attitude SPICE-kernels are not available as explained in the previous section. In these cases, a simple SPICE procedure [11] can be followed to create those kernels. Two subroutines have been implemented in order to read the SBDR binary data files and create the input files needed to start the run; the first one creates the file containing all the observation times values, the radar mode and beam values. The other one extracts the state vectors and attitude values from SBDR in the case the user needs to create the requested kernels before running the altimetric data simulation module.

Data Field Name	**Segment**	**Description**
`radar_mode`	engineering data	The operational mode of the radar. 0 = scatterometry, 1 = altimetry, 2 = low resolution SAR, 3 = high resolution SAR, 4 = radiometer. Adding 8 to any of these values indicates auto-gain is enabled.
`t_ephem_time`	intermediate level data	time at start of burst expressed in seconds since 12:00 AM Jan. 1, 2000.
`act_geom_time_offset`	science data	time offset in seconds from the burst reference time (`t_ephem_time`) for which the active geometry fields are computed.
`beam_number`	intermediate level data	the number (1-5) of the beam for which the measurements are obtained during the burst.

`sc_pos_j2000_x`
`sc_pos_j2000_y`
`sc_pos_j2000_z`
	intermediate level data	components of spacecraft position in target-centered J2000 inertial coordinate system.

`sc_vel_j2000_x`
`sc_vel_j2000_y`
`sc_vel_j2000_z`
	intermediate level data	components of spacecraft velocity in target-centered J2000 inertial coordinate system.

`sc_x_axis_x`
`sc_x_axis_y`
`sc_x_axis_z`
	intermediate level data	components of direction vector representing the spacecraft coordinate system's x axis in J2000 coordinate system. This is a unitless quantity. The vector magnitude is one.

`sc_y_axis_x`
`sc_y_axis_y`
`sc_y_axis_z`
	intermediate level data	components of direction vector representing the spacecraft coordinate system's y axis in J2000 coordinate system. This is a unitless quantity. The vector magnitude is one.

`sc_z_axis_x`
`sc_z_axis_y`
`sc_z_axis_z`
	intermediate level data	components of direction vector representing the spacecraft coordinate system's z axis in J2000 coordinate system. This is a unitless quantity. The vector magnitude is one.

`rot_vel_J2000_x`
`rot_vel_J2000_y`
`rot_vel_J2000_z`
	intermediate level data	components of the spacecraft angular velocity vector in J2000 coordinate system. Units are degrees/s.

Table A.2: List of data fields from SBDR used by the module.

A.4 SPICELIB subroutines calls

In this section we give the list of the SPICE's subroutines called by the simulation module to find the intersection points of the beam on the surface and compute the range values (the output values of interest are in blue).

First of all, to get the Titan's ellipsoid radii the following function is used:

```
call BODVRD ( satnm , item , maxn , dim , values ),
```

where `satnm` is the name of the body for which `item` is requested (`Titan`). `item` is the item to be returned, in this case the requested item is Titan's radius (`'radii'`). `maxn` is the maximum number of values that may be returned. For an ellipsoid the number is 3 and in the case of Titan the three values returned are the same because it is considered as a sphere. `dim` is the number of values returned and `values` is the array of values associated with the requested kernel variable.

Before acquiring the field of view of the instrument used, we need the translation of the name of this instrument to the corresponding SPICE integer ID code:

```
call BODN2C ( instnm , instid, found ),
```

where `instnm` is the name of a body or object or instrument, that is "known" to the SPICE system (`cassini_radar_3`). `instid` is the SPICE integer ID code for the named body and `found` is true if `instnm` has a translation.

Then we get the instrument boresight direction and the name of the instrument frame in which it is defined (the field of view configuration for the specified instrument) and we use

```
call GETFOV ( instid , room , shape , iframe , insite , N , bundry ),
```

where `room` is the maximum number of vectors that can be returned, `shape` is a character string that describes the "shape" of the field of view (`circle` for beam number 3, `ellipse` for the other radar beams). If the value of `shape` is '`circle`' the field of view of the instrument is a circular cone about the boresight vector. The vertex of the cone is at the instrument focal point. A single vector will be returned in `bounds`. If the value of `shape` is '`ellipse`' the field of view of the instrument is a elliptical cone with the boresight vector as the axis of the cone. In this case two vectors are returned in `bounds`. One of the vectors returned in `bounds` points to the end of the semi-major axis of a perpendicular cross section of the elliptic cone. The other vector points to the end of the semi-minor axis of a perpendicular cross section of the cone. `iframe` is the name of the reference frame in which the field of view boundary vectors are defined. At last `insite` is the vector that points in the direction of the center of the field of view, `N` is the number of boundary vectors returned and `bundry` is the array of vectors that point to the "corners" of the instrument field of view.

The computation of the boresight ray intersection with the surface of Titan is made by the use of

```
call SRFXPT ( method , satnm , et , abcorr , scnm , iframe , insite , point , dist ,
                              trgepc , obspos , found ).
```

`method` is a string providing parameters defining the computation method to be used. Parameters include, but are not limited to, the shape model used to represent the surface of the target body. The only choice currently supported is `'ellipsoid'`. `et` is the epoch of the observer, expressed as ephemeris seconds past J2000 TDB: it is the epoch at which the observer's state is computed. `abcorr` indicates the aberration correction to be applied when computing the observer-target state and the orientation of the target body (we use `'LT+S'` which indicates the correction for one-way light time and stellar aberration using a Newtonian formulation). `scnm` is the name of the observing body (`'Cassini'`). `point` is the Titan's surface intercept point of the ray defined by the observer and the direction vector. It is expressed in Cartesian coordinates, relative to the body-fixed frame associated with the target body. The body-fixed target frame is evaluated at the intercept epoch `trgepc` (see below). The output argument `found` indicates whether an intercept was found. `dist` is the distance between the observer and the surface intercept on Titan, `trgepc` is the "intercept epoch" and `obspos` is the vector from the center of the target body at epoch `trgepc` to the observer at epoch `et`. It is expressed in the target body-fixed reference frame.

Then, if an intercept is found, we compute planetocentric and (or planetodetic) latitude and longitude of the point:

```
call RECLAT ( point , R , pclon , pclat ),
```

where `R` is the distance of the point from the origin, `pclon` and `pclat` are the longitude $[-\pi, +\pi]$ and the latitude $[-\pi/2, +\pi/2]$ of the point.

In the planetodetic case, we need the natural satellite's longer equatorial radius `RE`, polar radius `RP` and flattening factor `F` ($F = (RE - RP)/RE$):

```
call RECGEO ( point , RE , F , pdlon , pdlat , alt ).
```

`pdlon` and `pdlat` are the planetodetic longitude $[-\pi, +\pi]$ and latitude $[-\pi/2, +\pi/2]$ of the point, `alt` is the altitude of point above the reference spheroid.

Appendix B

SOSYA_ART: SOlar SYstem Astrometry_Altimetric Run Tool

One of the aims of SOSYA [2] is the orbit determination of Cassini spacecraft by means of the altimetric data provided by the radar instrument on board the probe. This is implemented in the module called SOSYA_ART, SOlar SYstem Astrometry_Altimetric Run Tool. In addition the software performs altimetric data simulation as explained in Appendix A and it is built to work on different mission scenarios such as flybys with the other bodies of the Solar System.

B.1 Function and purpose of the altimetric part of the software

The technical objectives of the altimetric run of SOSYA_ART are summarized here:

- **Orbit Simulation**: Saturnian system's natural satellites orbit propagation by numerical integration of the equations of motion using a full set of acceleration models in order to find Titan's ephemeris at altimetric observation times needed by the model developed;
- **Measurement Simulation**: altimetric data simulation in body-fixed reference frame in the case real altimetric measurements are not available;
- **Orbit Determination**: Titan's orbit determination by the use of the altimetric data;
- **Covariance Analysis** (not implemented): sensitivity study of orbits of natural satellites; a priori observation errors covariance matrix and a priori covariance matrix of consider parameters.

The complete list and explanation of SOSYA integration and interpolation capability can be founded in details in [2]. Following the codification methods required by SOSYA, the altimetric part is implemented using as programming language the Fortran95 standard and adopting object-orienting programming methodology.

B.2 Relation to other systems

The software interacts with two external systems precompiled into separated library and linked to the software:

- SPICE [11], a NAIF (Navigation and Ancillary Information Facility at JPL) developed software system that provides the capability to easily combine accurate space geometry and event data with mission analysis, observation planning, or science data processing software. SOSYA_ART code uses SPICE toolkit to compute radar beam intersection point with Titan's surface in order to get the computed range value of the observation model developed. In particular SPICE toolkit is used to get Cassini's attitude matrix together with its RADAR instrument displacement and the direction of the fields of view at given observation time. The same SPICE functions are called in the altimetric data simulation process.

- DIVA [10], a variable order integrator for ordinary differential equations: this integrator is based on the predictor-corrector scheme of Adams-Bashforth and Adams-Moulton.

B.3 Modular description

In Figure B.1 we give the modular view of SOSYA program and in Figure B.2 we give the flowchart diagram of SOSYA_ART, the orbit determination module that uses the altimetric data.

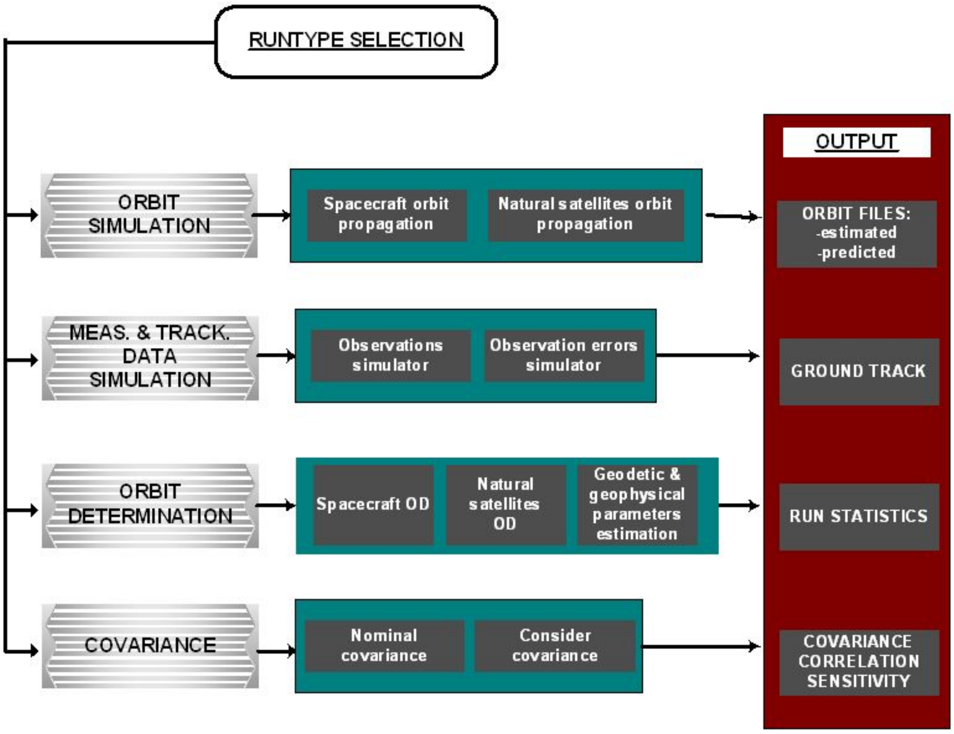

Figure B.1: Modular view of SOSYA.

B.4 Component description

In this section we describe the components of SOSYA_ART software module.

B.4.1 Classes

The following tables give a brief description of all the classes contained in the altimetric code implemented. The description of the components concerning with natural satellites orbit propagation and ephemeris interpolation is given in [2].

Class	Description
altimetric_class	manages the available altimetric data type
estimation_class	manages the estimation input parameters

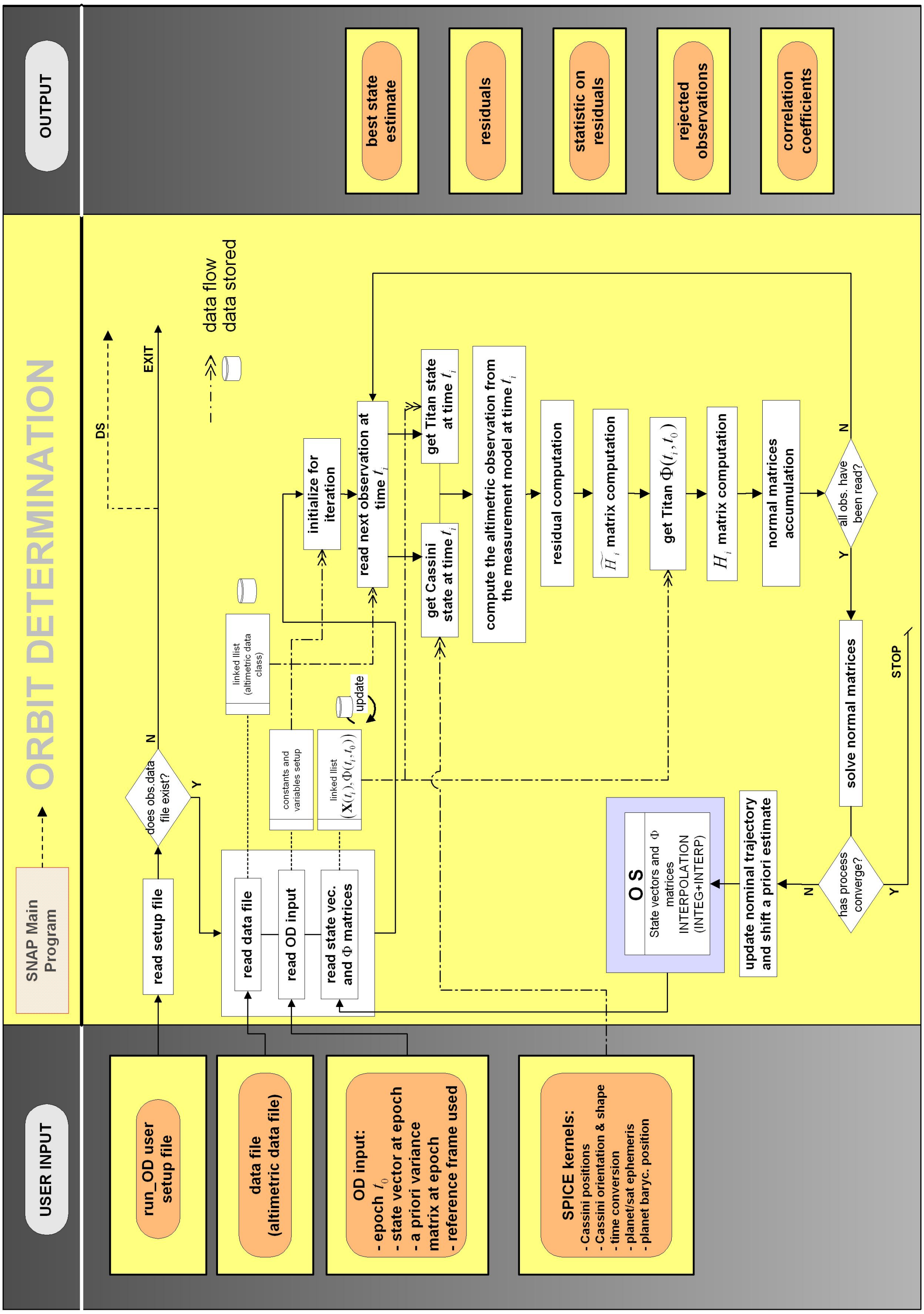

Figure B.2: Flow chart diagram of SOSYA_ART.

altimetric_class

Variables		
Name	**Type**	**Description**
burst_ID	integer	radar burst's identification number
time_et	real	ephemeris time of the radar burst
height	real	range to body target
hsigma	real	range measurement error
angle_off_nadir	real	off nadir angle of the radar FOV
hres	real	residual
rejected	logical	rejection flag of the observation

Methods	
Name	**Description**
init_altimetric_data	initializes variables of altimetric_class
set_altimetric_data_burst_ID	sets the identification number of the input data
get_altimetric_data_burst_ID	gets the identification number of the input data
set_altimetric_data_time_et	sets the ephemeris time of the input data
get_altimetric_data_time_et	gets the ephemeris time of the input data
set_altimetric_data_height	sets the altimetric range at the ephemeris time
get_altimetric_data_height	gets the altimetric range at the ephemeris time
set_altimetric_data_hsigma	sets the measurement error of the given range
get_altimetric_data_hsigma	gets the measurement error of the given range
set_altimetric_data_angle_off_nadir	sets the off nadir angle of altimetric observation
get_altimetric_data_angle_off_nadir	gets the off nadir angle of altimetric observation
set_altimetric_data_residual	sets the computed residual at the ephemeris time
get_altimetric_data_residual	gets the computed residual at the ephemeris time
set_altimetric_data_rejectflag	sets the rejection flag for the observation
get_altimetric_data_rejectflag	gets the rejection flag for the observation
count_rejected_observations	counts the number of the rejected observations
Read_next_alt_observation	reads the altimetric data for a given observation ID
hresidual_statistics	computes the mean, standard deviation and rms of residuals

estimation_class

Variables		
Name	**Type**	**Description**
time_t0	real	epoch of the state to be estimated
state_t0	real(6)	body's initial conditions at epoch
ref_frame	character(2)(2)	reference frame description of the initial conditions
P0_variance	real(:,:)	a priori variance-covariance matrix at epoch

Methods	
Name	**Description**
init_estimation_class	initializes variables of estimation_class
set_estimation_time0	sets the epoch at which the state is estimated
get_estimation_time0	gets the epoch at which the state is estimated
set_estimation_state_t0	sets the initial state at epoch
get_estimation_state_t0	gets the initial state at epoch
set_estimation_frame	sets the reference frame
get_estimation_frame	gets the reference frame
set_estimation_variance	sets the a priori variance matrix
get_estimation_variance	gets the a priori variance matrix

B.4.2 Modules

In the following tables a brief description of all the modules contained in the software's code is given.

normal_matrices

Subroutine	Description
set_normal_matrices	allocates normal matrices
set_initial_matrices	sets normal matrices's initial values
accumulate_normal_matrices	accumulates normal matrices at each observation
solve_normal_matrices	solves normal matrices
write_output_correlation_file	writes correlation matrix on files
compute_correlation_matrix	computes the correlation matrix
minvch	inverts a symmetric matrix using choleski algorithm

altimetric_observation_model

Subroutine	Description
compute_altimetric_vector	computes the altimetric measurement from the model
dh_over_dX_J2000	computes partials derivatives of the observation equation
line_sphere_intersection	computes the intersection point of the radar beam with the surface

read_input_data_files

It reads the input altimetric data files.

Subroutine	Description
Read_Data_Files	driver for input data files reading
Read_Altimetric_Data	reads files containing the altimetric data type

read_user_input_files

It reads the input files supplied by the user.

Subroutine	Description
Read_Input_Files_nl	driver for input files reading
Read_RunType_File	reads the type of run the user decides to do
Read_RunOD_File	reads the general setting for orbit determination run type
Read_Estimation_input	reads input parameters related to the estimation process
inquire_if_file_exixts	inquires the existence of an input file

SOSYA_ART_run

It controls the orbit determination process.

Subroutine	Description
orbit_determination_run	driver for orbit determination
open_output_files	opens files to write residuals and output values
close_output_files	closes files to write residuals and output values
compute_statistics_on_residuals	computes statistics on residuals
write_state_estim_output	writes the estimated state vector on output file
write_residuals	writes statistics residuals
write_rejected_observations	writes the rejected observations on files

precision

It specifies the arithmetic precision used by the program.

input_setting_module

It sets the common variables coming from user's choices.

alt_constants

It defines altimetric constants used by the program.

In Figures B.3, B.4, B.5, B.6, B.7, B.8, B.9, B.10 and B.11, we give the call trees of SOSYA_ART. The dashed routine are subroutine contained in the precompiled library and linked to the program (SPICE, DIVA).

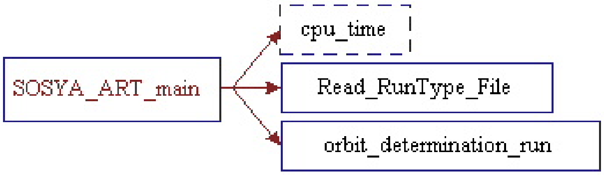

Figure B.3: SOSYA_ART: altimetric OD run call tree, main program.

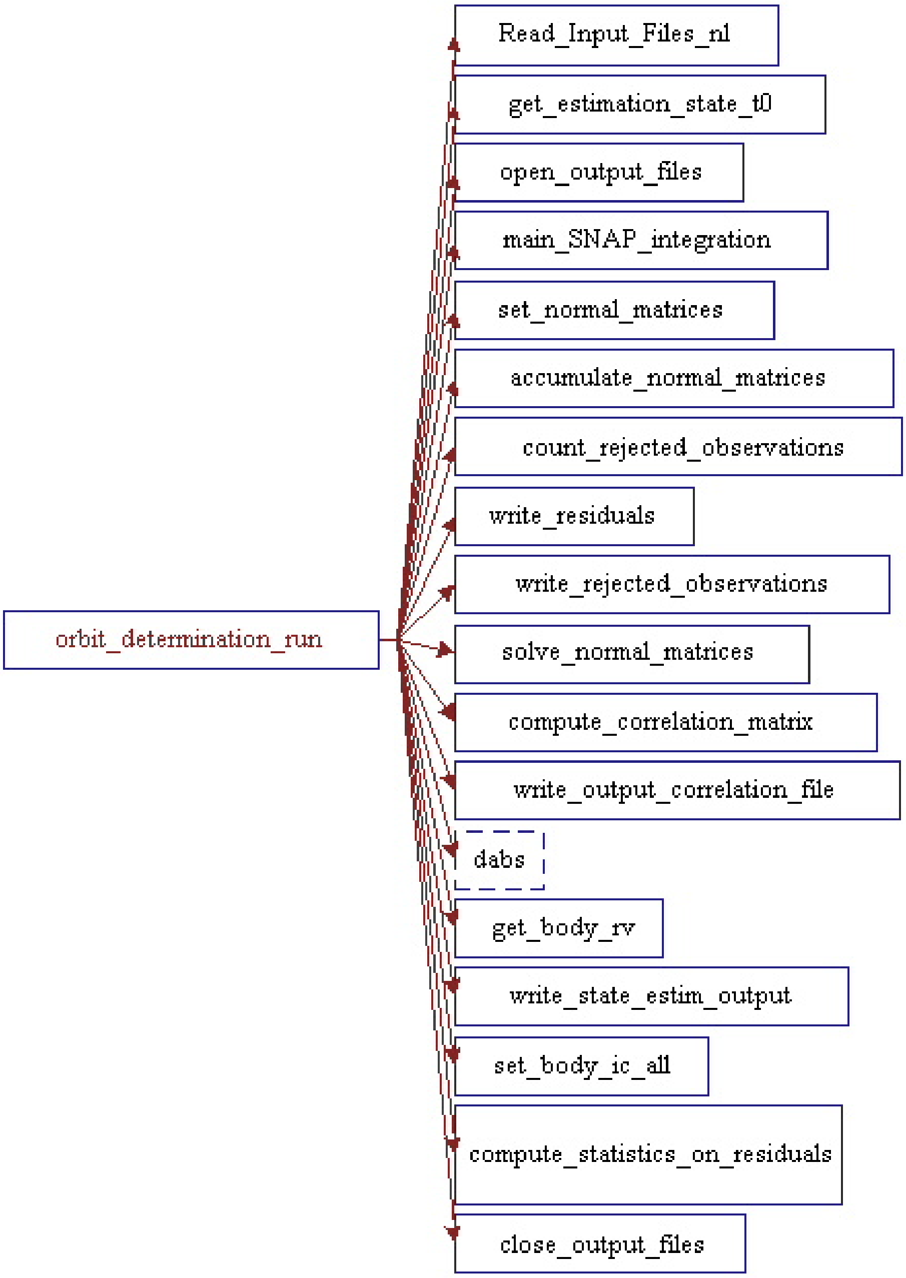

Figure B.4: SOSYA_ART: altimetric OD run call tree, orbit determination process.

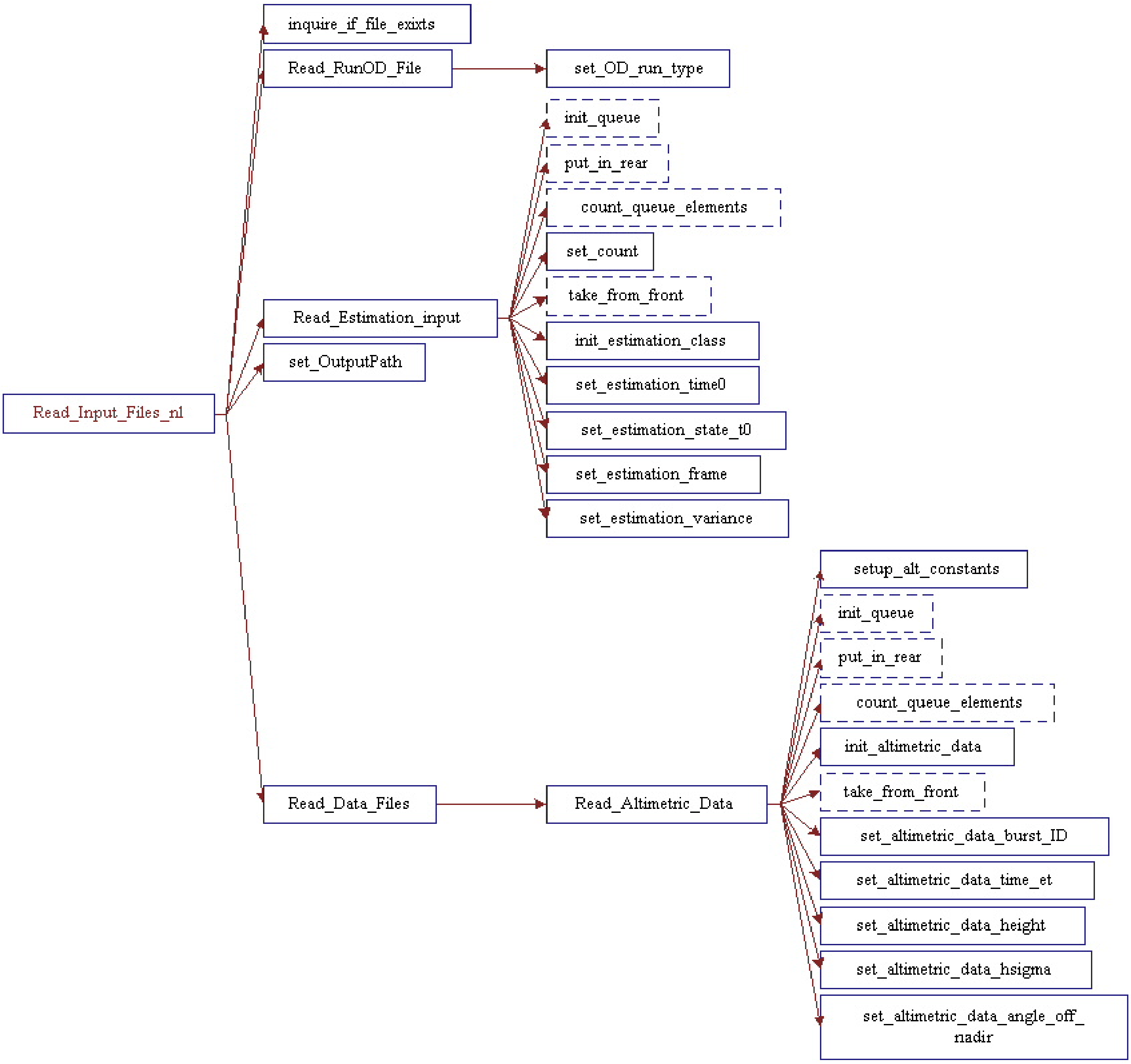

Figure B.5: SOSYA_ART: altimetric OD run call tree, read input files.

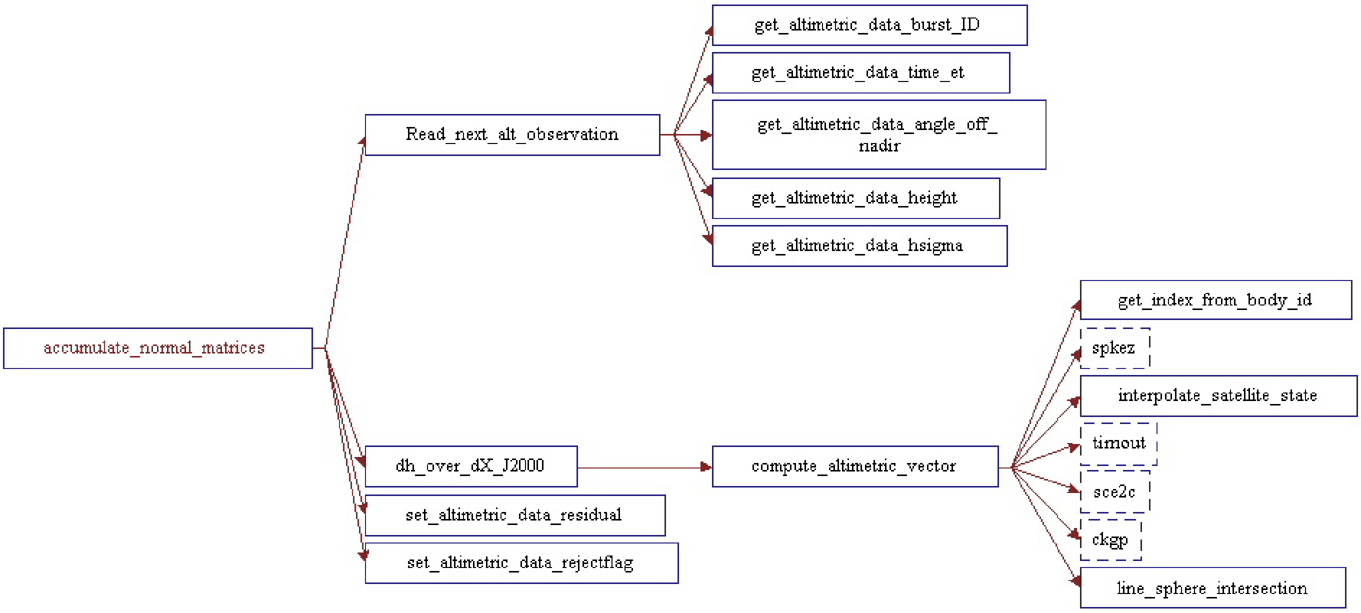

Figure B.6: SOSYA_ART: altimetric OD run call tree, normal matrix accumulation.

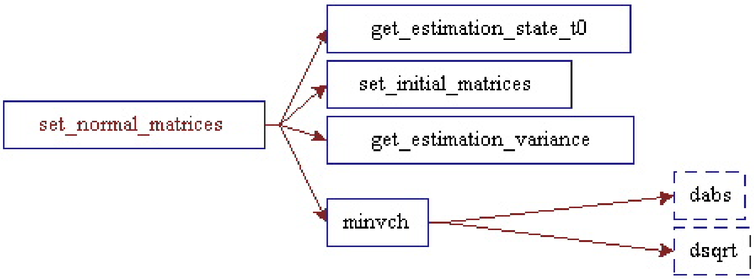

Figure B.7: SOSYA_ART: altimetric OD run call tree, normal matrix setting.

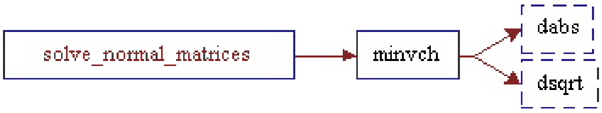

Figure B.8: SOSYA_ART: altimetric OD run call tree, normal matrix solution.

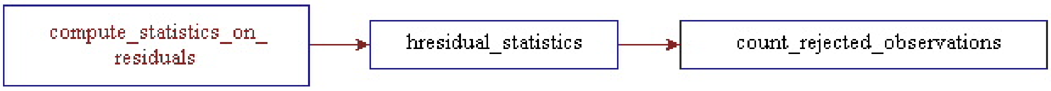

Figure B.9: SOSYA_ART: altimetric OD run call tree, statistic on residuals.

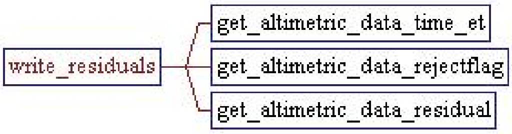

Figure B.10: SOSYA_ART: altimetric OD run call tree, residuals files writing.

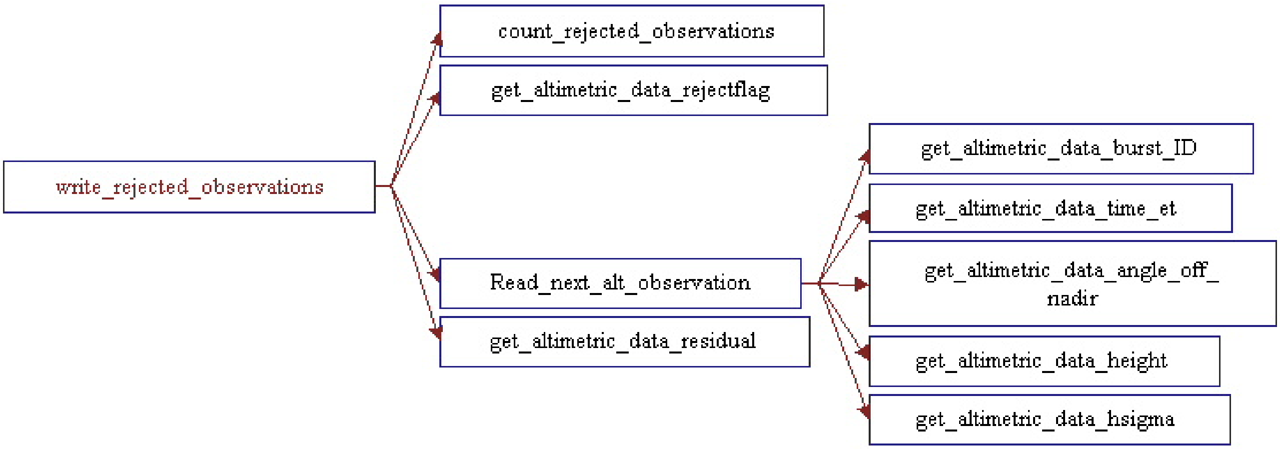

Figure B.11: SOSYA_ART: altimetric OD run call tree, rejected observation files writing.

Appendix C

SPICE subroutine CKGP

The function `CKGP` gets instruments pointing or spacecraft's attitude for a specified clock time (for more details see [11]). The procedure together with the input/output elements is the following:

$$\texttt{SUBROUTINE CKGP (INST, SCLKDP, TOL, REF, CMAT, CLKOUT, FOUND)} \tag{C.1}$$

where

- `INST` (input) is the NAIF ID of instrument, spacecraft, or structure.
- `SCLKDP` (input) is the encoded spacecraft clock time.
- `TOL` (input) is time tolerance.
- `REF` (input) is the reference frame.
- `CMAT` (output) is the C-matrix pointing data ($\mathcal{R}_{sc}$).
- `CLKOUT` (output) is the output encoded spacecraft clock time.
- `FOUND` (output) is true when requested pointing is available.

Since we have time in ET seconds past J2000 format, the subroutine `sce2c` is used to convert ephemeris seconds to continuous encoded spacecraft clock ('ticks') before calling `CKGP`. The value returned, `SCLKDP`, is the encoded spacecraft clock value which is a representation of the total number of spacecraft clock ticks measured from the time the spacecraft clock started to the epoch ET.

`TOL` is a time tolerance in ticks, the units of encoded spacecraft clock time. The C-matrix ($\mathcal{R}_{sc}$) returned by `CKGP` is the one whose time tag is closest to `SCLKDP` and within `TOL` units of `SCLKDP`.

The returned C-matrix gives the orientation of the instrument designated by `INST` relative to the frame designated by `REF`. When a vector specified relative to frame `REF` is left- multiplied by `CMAT`, the vector is rotated to the frame associated with `INST`.

`CMAT` is a rotation matrix that transforms the components of a vector expressed in the reference frame specified by `REF` to components expressed in the frame tied to the instrument, spacecraft, or other structure at time `CLKOUT`. Thus, if a vector v has components (x, y, z) in the `REF` reference frame, then v has components (x', y', z') in the instrument fixed frame at time `CLKOUT`:

$$\begin{pmatrix} x' \\ y' \\ z' \end{pmatrix} = \mathcal{R}_{sc} \begin{pmatrix} x \\ y \\ z \end{pmatrix} , \tag{C.2}$$

If (x', y', z') are known, the transpose of the C-matrix is used to determine (x, y, z) as follows:

$$\begin{pmatrix} x \\ y \\ z \end{pmatrix} = \mathcal{R}_{sc}^{\mathrm{T}} \begin{pmatrix} x' \\ y' \\ z' \end{pmatrix} . \tag{C.3}$$

`CLKOUT` is the encoded spacecraft clock time associated with the returned C-matrix. This value may differ from the requested time, but never by more than the input tolerance `TOL`.

`FOUND` is true if a record was found to satisfy the pointing request and it is false otherwise.

Bibliography

[1] Akin, E., *Object Oriented Programming via Fortran 90/95*, Cambridge University Press, New York, 2003.

[2] Bardella M., *Determination of the orbits of the natural satellites of Saturn from optical observations*, PhD Thesis, School of PhD of Research in Sciences Technologies and Measurements for Space (Astronautic and Satellite Science).

[3] CO.RI.S.T.A., *Cassini Radar Altimeter - ASCII File Description (Version 2 Data)*, 2007/10/25.

[4] Eddy, W.F., McCarthy, J.J., Pavlis, D.E., Marshall, J.A., Luthcke, S.B., Tsaoussi, L.S., Leung, G., Williams, D.A., “GEODYN II - Vol. 1, Systems Description”, STX System Corporation, Philadelphia, 1990.

[5] Elachi C., *Introduction to the Physics and Techniques of Remote Sensing*, Wiley series in remote sensing, Wiley-Interscience Publication, 1987.

[6] Elachi C., *RADAR Engineering Technical Write-up*

[7] Franceschetti G. and Lanari R., *Synthetic Aperture RADAR PROCESSING*, Electronic engineering system series, 1999.

[8] Jacobson, R.A., “The Orbits of the Major Saturnian Satellites and the Gravity Field of Saturn from Spacecraft and Earth-Based Observations”, *The Astronomical Journal*, **128**, 492, 2004.

[9] JPL, Navigation Software Group, “DPTRAJ-ODP User’s Reference Manual”, Volume 1, Volume 2, Volume 3, Volume 4, 1996.

[10] JPL, *Variable Order Adams Method for Ordinary Differential Equations*, California Institute Of Technology, Math à la Carte, 2006.

[11] JPL, NAIF (The Navigation and Ancillary Information Facility at JPL), “Most Useful SPICELIB subroutines”, NAIF, 2001.

[12] Lorenz R.D. *et al*, *Cassini RADAR: prospects for Titan surface investigations using the microwave radiometer*, Planetary and Space Science **51** (2003) 353-364

[13] Melacci P.T., Orosei R., Picardi G. and Seu R., *Cassini radar: system concept and simulation results*, Planetary Space Science, Vol 46, No 9/10, pp 1363-1374, 1998.

[14] NASA, JPL, *Cassini-Huygens, Mission To Saturn and Titan*, online documentation.

[15] Nerem R.S., *Determination of the general ocean circulation using satellite altimetry froma simultaneous solution for the Earth’s gravitational field*, Center for Space Research, The University of Texas at Austin, CSR-89-2.

[16] Pelletier F., *Altimeter Range Crossover Analysis for the Near Asteroid Rendezvous Mission*, University of Texas at Austin, December 2000.

[17] Peters, C.F., “Numerical Integration of the Satellites of the Outer Planets”, *Astronomy and Astrophysics*, **104**, 37-41, 1981.

[18] Picardi G., *Elaborazione del segnale radar Metodologie ed applicazioni*, Collana Scientifica 1340.51, Franco Angeli Editore

[19] Stiles B., *Cassini Radar Burst Ordered Data Product SIS, Version 1.5*, Cassini Radar Instrument Team, Jet Propulsion Laboratory, Californian Institute of Technology, NASA, D-27891, September 27, 2005.

[20] Stofan E., Lunine J. et al., *Mapping of Titan: Results from the first Titan radar passes*, Icarus 185, 443-456, 2006.

[21] Tapley, B., Schutz, B., Born, G.H., *Statistical Orbit Determination*, Elsevier Academic Press, 2004.

[22] Zebker, H. A., Stiles, B., Hensley, S., Callahan, P., Gim, Y., Lorenz, R. D., Kirk, R. L.,*Titan’s Shape from Cassini Radar Altimeter and SAR Monopulse Observations*, American Geophysical Union, Fall Meeting 2008, abstract P11D-02.